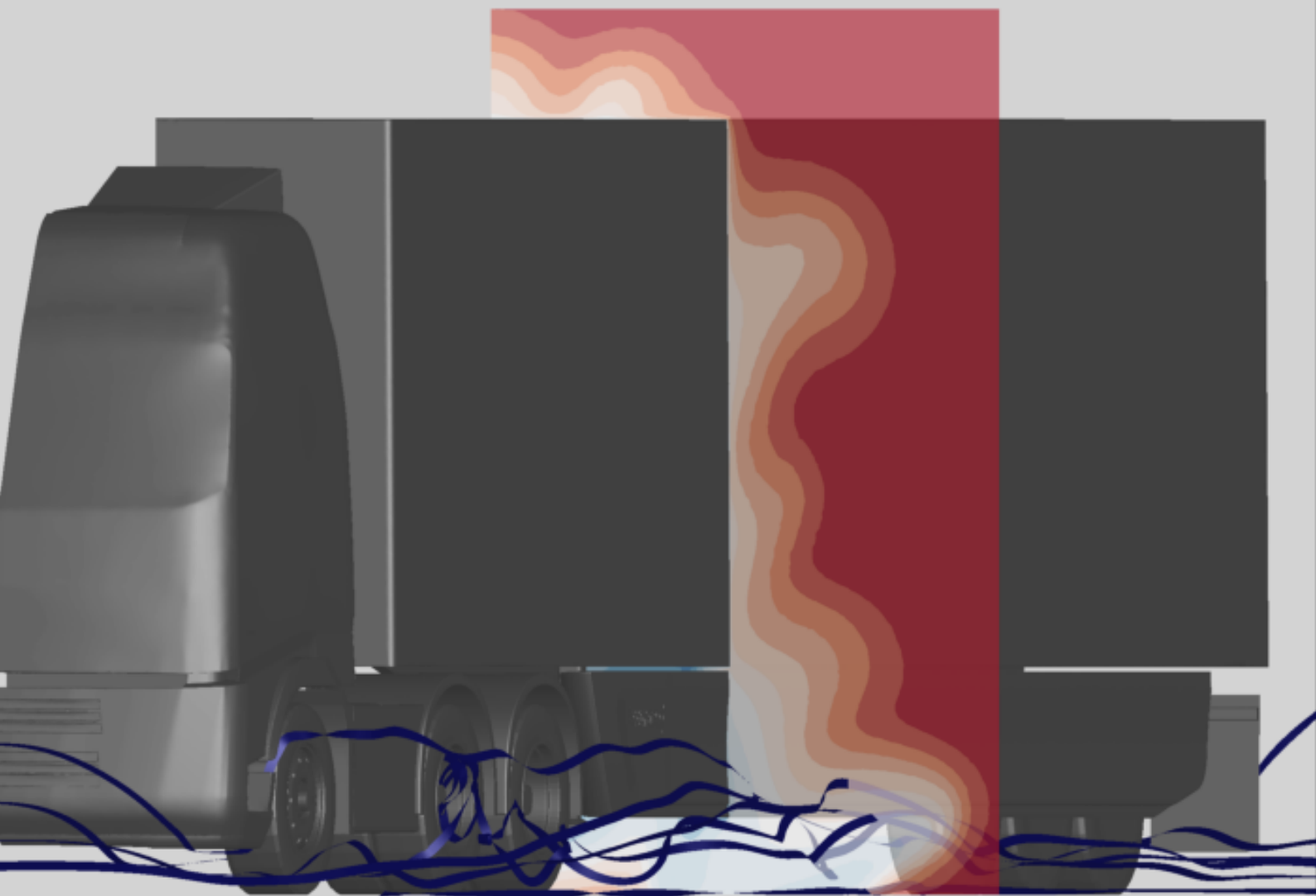


Numerical analysis of side-skirt in dual rear axle condition

Sumedh Jain Y R



Numerical analysis of side-skirt in dual rear axle condition

Sumedh Jain Y R

to obtain the degree of Master of Science
at the Delft University of Technology,
to be defended publicly on May 29, 2018 at 2:00 PM.

Student number: 4501586
Project duration: March 1, 2017 – May 29, 2018
Thesis committee: dr. ir. B. W. van Oudheusden, TU Delft, Chair
ir. W. A. Timmer, TU Delft, External Examiner
dr. ir. A. H. van Zuijlen, TU Delft, Supervisor
dr. ir. G. van Raemdonck, TU Delft & WABCO, Supervisor

This thesis is confidential and cannot be made public until May 29, 2023.

An electronic version of this thesis is available at <http://repository.tudelft.nl/>.

Acknowledgement

My journey here at T U Delft is almost coming to an end. I would like to thank a few people who were part of this journey especially the ones who helped with this thesis.

Firstly, I would like to thank Gandert van Raemdonck for trusting me with this project and allowing me to widen my horizons in the field of Aerodynamics. He always encouraged me and pushed me to do things that I thought were beyond me. I thank him for showing me that a person can do more than he can think of. Secondly, I extend my gratitude to Sander van Zuijlen, my internal supervisor. He showed good interest and excitement when I and Gandert pitched him this project. His office doors were always open for any doubts be it conceptual or something very simple. When I was having tough time running my several week long simulations and sometimes lose results because of some issue with cluster, he was there to listen to me ramble on and on about it. He understood the problems I was handling with cluster and was very considerate about them. I really thank both my supervisors from the bottom of my heart for being instrumental in my journey of becoming a well-rounded engineer (hope so!).

Last but not the least, I cannot thank my parents for letting me pursue my dream of being an aerospace engineer. Especially my mother, a brave heart, has sacrificed a lot to see me in this position.

Any journey would not be complete without good friends, I made some good friends during my thesis. I would like to thank Jordi, Lluís, Ka Hin, Alex, Yash, Arun, Gigi and Fancy for their companionship. Would like to extend a special thanks to Mart for going through my thesis at crucial period and giving me some valuable comments.

Sumedh Jain Y R
Delft, May 2018

Contents

List of Figures	vii
List of Tables	ix
1 Introduction	1
1.1 Research Goals	3
2 Aerodynamic Background	5
2.1 Flow Physics	5
2.1.1 Wheelhouse Flow	5
2.1.2 Underbody Flow	7
2.1.3 Performance Study of WABCO-OptiFlow's SideWing™	10
2.1.4 Full Scale tests with Side-skirts	10
2.2 Research question, aims and objectives	10
3 Theoretical Methodology	11
3.1 Numerical Set-up	11
3.1.1 CFD Approach	11
3.1.2 Reynolds Averaged Navier Stokes (RANS)	13
3.1.3 Turbulence Modelling	13
3.1.4 Wall Modeling	14
3.1.5 General Scalar Transport Equation	15
3.2 Discretisation Schemes	15
3.2.1 Spatial Discretisation	15
3.2.2 Gradient and Derivative Evaluation	16
3.2.3 Temporal Discretisation	16
3.2.4 Final Discretised System (Linearized)	16
3.3 Solver Algorithm	17
3.4 Truck Model Profile	17
3.5 Rotating Flow Modeling	19
3.6 Domain Sizing and Boundary Conditions	20
3.7 Type of Cells	21
3.7.1 Polyhedron Cells	21
3.8 Physical Run Time	23
3.9 Summary of Numerical Set-up	24
4 Mesh Sensitivity	25
4.1 Meshing Strategy	25
4.1.1 Mesh constraints	25
4.2 Mesh Sensitivity Analysis	27
4.2.1 GCI study	28
5 Results	31
5.1 Validation	31
5.1.1 Spectral Validation	33
5.1.2 Downstream Behaviour	34

5.2	Side-skirt Behaviour	35
5.3	Averaging Window Analysis	37
5.4	Underperformance Quantification	38
5.4.1	Fuel Savings	38
5.5	Cause of underperformance	39
5.5.1	No side-skirt cases	42
5.5.2	Side-skirt cases	42
5.6	Instantaneous and Time averaged solution	46
5.7	Summary of all dynamics	47
5.8	Modifications	48
5.8.1	Evaluation of modifications	48
5.8.2	More insights into MODs.	48
5.9	Geometry Simplification	50
6	Conclusions and Recommendations	51
6.1	Recommendations.	52
A	Appendix A	55
B	Appendix B	57
B.1	Linearized Equation Coefficients	57
B.2	Coupled Solver Algorithm	57
C	Appendix C	59
D	Appendix D	61
D.1	Drag-Fuel formula derivation.	61
E	Appendix E	65
	Bibliography	67

List of Figures

1.1	CO_2 emissions of Tractor-Trailer by Miller and Façanha [10]	2
1.2	Fuel consumption reduction potential in 2030 [12]	2
1.3	Add-on devices classification	2
1.4	Add-on devices adoption comparison	3
1.5	Tractor configurations	3
2.1	Region of Flow Investigation highlighted	6
2.4	Simplified truck model used by [15]	7
2.5	Underbody flow simulated by [22]	8
2.6	Underbody flow by Scheeve [17] (steady state) at two different iterations. Plots of C_{p_t} at $Z/D = 0.5$	8
2.7	Underbody normalized Velocity contour for no side-skirt case by Stephens and Babinsky [20], $Z/b = 0.16$, horizontal plane	9
2.8	Underbody normalized Velocity contour for side-skirt case by Stephens and Babinsky [20], $Z/b = 0.16$ (b =width of truck), horizontal plane	9
2.9	Velocity Contour in $x/b=2.51$	9
3.1	DES/RANS base wake prediction (Baseline refers to RANS)	12
3.2	DES/RANS wake prediction behind a cube	12
3.3	Behaviour of the boundary layer in the vicinity of the wall[24]	14
3.4	Truck Model	18
3.5	Configuration Studied	18
3.6	Coefficient of total pressure in a plane located 100 mm behind the wheel axle. From top left: Location of measurement plane, experimental results, Rotating Wall, MRF I, MRF II and Sliding Mesh.	19
3.7	Rotating Wheel Implementation. Wheel cut off $2mm$ at the bottom to emulate wheel patch. The cut-off edges are joined with ground plane	20
3.8	Domain size, $L = 16.5m$	21
3.9	3D model as used by simscape	21
3.10	Cell Type Comparison-I	22
3.11	Cell Type Comparison-II	23
4.1	y^+ contour over truck	26
4.2	Boundary layer at the end of trailer, ($X/D = 10$, measured from trailer leading edge)	26
4.3	Refinement Regions	27
4.4	Overview of Mesh	28
5.1	L,E,R Vortices Validation	32
5.2	Vortex Profile, $X/D = 0.2$	32
5.3	Downstream validation with Stephens and Babinsky [20] on no-side-skirt case . $Z/D=0.01$ (top), $Z/D=0.2$ (middle), $Z/D=0.5$ (bottom)	33
5.4	Standard Deviation Spectrum	34

5.5	L,E,R vortices (Only E & R merging is shown in this image, L merges further downstream)	34
5.6	All vortices coalesced as large blobs of separated region. The original positions of vortices observed in figure 5.2a is also highlighted, Isosurfaces of $C_{P_t} = -1.2$ coloured by X-vorticity	35
5.7	Side-skirt restricting flow, $Z/D=0.52$	36
5.8	Side-skirt performance in 4X2 (single axle condition)	36
5.9	Windtunnel setup of van Raemdonck	36
5.10	Y-momentum analysis, outflow (<i>blue</i>), inflow (<i>red</i>), slice $Y/D = -0.01$	37
5.11	Averaging window analysis	37
5.12	Brake thermal efficiency distribution of engines based on certified model year [5]	39
5.13	Underbody bleed	39
5.14	Massflow rate plane positions	40
5.15	Inflow and low pressure regions	41
5.16	Low momentum fluid ejection from rear wheel-well. Streamlines emanating from Wheel-well and joining the freestream	41
5.17	Influx at $X/D = 4.5$	42
5.18	Suction region, isosurfaces of $C_p = -0.16$ colored by C_{P_t}	42
5.19	Influx difference in side-skirt cases, slice $Z/D = 0.3$	43
5.20	Ripples emerging from rear wheels, along with inflow entry marked, $Z/D = 0.3$	44
5.21	Bleed flow, wheel-well flow, inflow interaction	44
5.22	Y-momentum analysis, outflow (<i>blue</i>), inflow (<i>red</i>), slice $Y/D = -0.01$	45
5.23	Pressure difference between inside of trailer and outside along the length of the side-skirt	46
5.24	Instantaneous and Time averaged	47
5.25	Modifications	49
5.26	C_D comparison of MODS	50
D.1	flow entering trailer underbody	61
D.2	6X4-SS Instantaneous Y-momentum, outflow (<i>blue</i>), inflow (<i>red</i>), slice $Y/D = -0.01$	62
D.3	Inflow and high pressure ripple correspondence	63
D.4	Instantaneous and Time average plots	64
E.1	Underbody	65
E.2	Underbody with engine block, shaft components, axle, wheels cut-off to emulated wheel patch	66

List of Tables

3.1	Truck Dimensions	17
3.2	Overview of Boundary Conditions	20
4.1	Refinement Box Sizing in different grids	27
5.1	Massflow rates and side-skirt efficiency and drag coefficients	38
5.2	Fuel Savings (normalized)	38
5.3	Massflow rates (<i>kg/s</i>)	39
5.4	Bleed rates (<i>kg/s</i>)	40
5.5	Mass flow rate (kg/s)	46
5.6	Mass Flow Rates (<i>kg/s</i>)	48
A.1	Model Constants	56
C.1	GCI study based on [3]	59
C.2	Surface Mesh Size Control	60

Nomenclature

Greek Symbols

Symbol	Description	Dimensions	Units
ν	kinematic viscosity of fluid	L^2/T	m^3s^{-1}
ϕ	Scalar Quantity	-	-
ϕ_c	Cell centered scalar quantity	-	-
ϕ_f	face centered scalar quantity	-	-
ρ	Density of fluid	M/L^3	kgm^{-3}

Other Symbols

Symbol	Description	Dimensions	Units
\bar{u}	mean flow velocity	L/T	ms^{-1}
FC	Fuel Consumption	L^3/T	m^3s^{-1}
MFR	Mass flow rate	M/T	$kg s^{-1}$
u'	fluctuating velocity	L/T	ms^{-1}

Introduction

The CO_2 emissions from Heavy Duty Vehicles (HDVs) rose by 36% between 1990 and 2010 [1]. Projections indicate that without policy action, total HDV emissions would increase by 78.5% in 2030 (figure 1.1). With the currently adopted policy and regulations it can be brought down to a 67% increase while the current technology potential can bring it down to a 46% increase in CO_2 emissions (Miller and Façanha [10]).

The importance of aerodynamics in fuel consumption reduction is illustrated in figure 1.2. Norris et al. [12] suggest that, by 2030, technology can bring about 33% reduction in fuel consumption in HDVs. In that 33%, 10% of reduction comes from aerodynamic devices. Thus improvement in current aerodynamic devices is crucial. Truck aerodynamic devices usually come as add-ons and they have been classified into gap, underbody, rear devices as shown in figure 1.3. The gap devices include extended roof over the tractor, gap reducers on the side. Underbody devices include Side-skirts and fairings while rear devices include extended tail. A study conducted by Mihelic et al. [9] for NACFE¹ is presented in figure 3.4a. The organization conducted research by structured interviews with major OEMs and many trailer aerodynamic device manufacturers in North America. It can be noted from figure 3.4a that adoption of trailer skirts in fleets has been increasing since 2009. This can be attributed to its high fuel savings (7%, highest among other aerodynamic add-ons) and least payback time (<1 year) (Mihelic et al. [9]).

This thesis is aimed at improving WABCO-OptiFlow's trailer side-skirt named SideWing™. Side-skirt's performance is crucial for both fleet owners and emission regulation agencies. Along with reduction in fuel consumption of $1.5L/100km^2$, WABCO's side-skirt also provides emission reduction of 3.8 tonnes of CO_2 per truck per year. Recent customer reviews, track data and on board systems suggest that Side-skirt is underperforming when mounted on a dual rear axle tractor-trailer combination (*6X4 tractor*). Going by data collected by WABCO, the performance has dropped to $1L/100km$. The goal of this thesis is to identify the root cause of this problem by comparing single and dual axle cases with and without side-skirt.

Before moving forward, it is necessary to understand the difference between single and dual axle tractor models. A truck usually has two main components, the tractor and the trailer. Tractors haul the trailers and both have their own aerodynamic devices. Side-skirt is a trailer aerodynamic device which is placed along the sides of the trailer. The tractors come in many

¹North American Council for Freight Efficiency

²Average Fuel Consumption at 85kmph

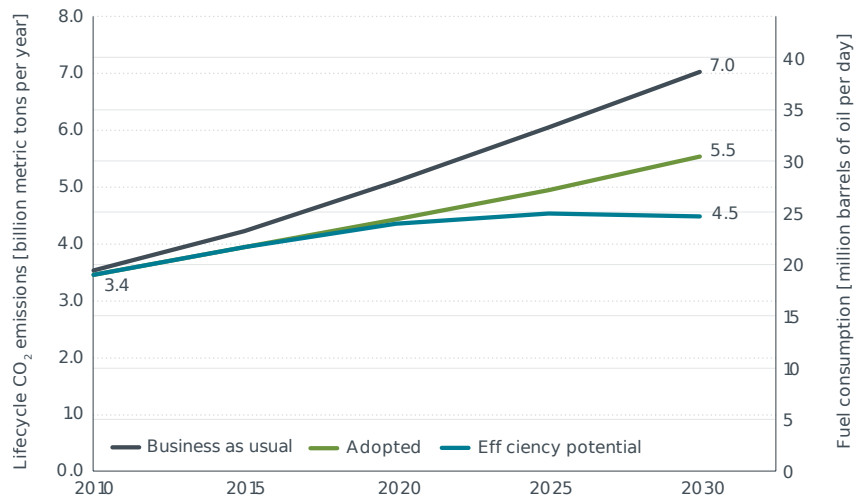


Figure 1.1: CO₂ emissions of Tractor-Trailer by Miller and Façanha [10]

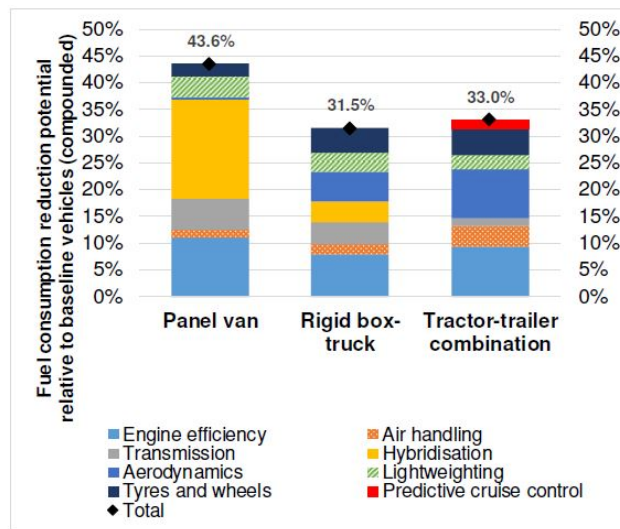


Figure 1.2: Fuel consumption reduction potential in 2030 [12]

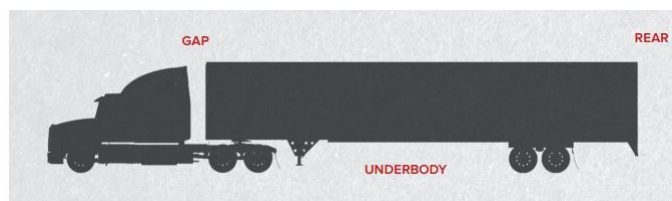


Figure 1.3: Add-on devices classification

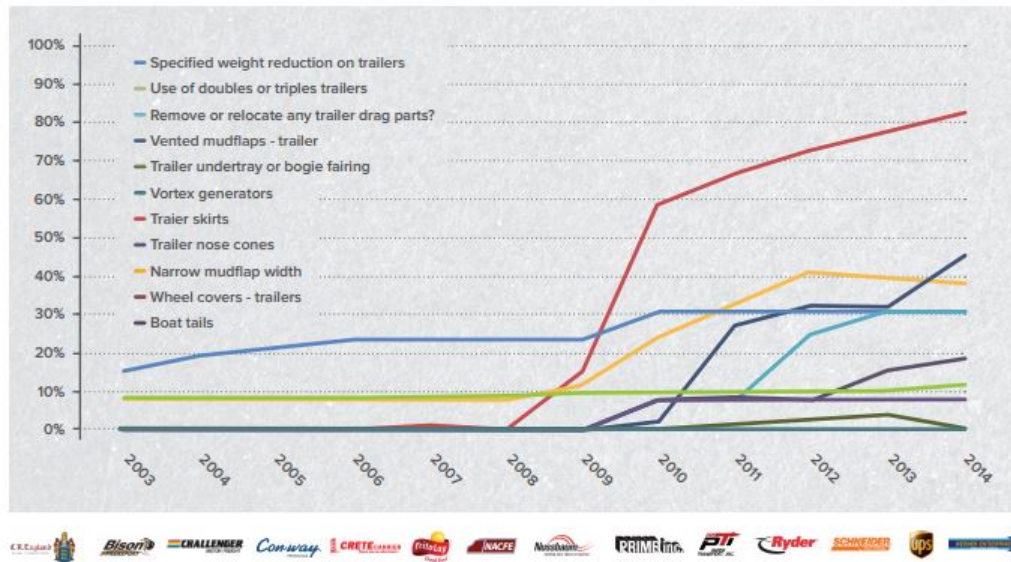


Figure 1.4: Add-on devices adoption comparison

configurations, out of them the ones studied in this thesis are 4X2 (single rear axle or simply single axle) (figure 1.5a) and 6X4 (dual rear axle or simply dual axle)(figure 1.5b). The additional axle is also powered in this dual axle variant or in other words the both the rear axles power the vehicle.

(a) 4X2 Single Axle
Courtesy Volvo(b) 6X4 Dual Axle
Courtesy Autoline

Figure 1.5: Tractor configurations

1.1. Research Goals

- Understand the working principle of a trailer side-skirt through literature. Isolate the parameters the responsible for drag reduction in single axle case.
- Quantify the underperformance in terms of fuel savings or drag.
- Relate the changes observed in parameters influencing the performance of side-skirt when in dual axle condition (6X4). Correlate the changes in parameters to hindered performance of side-skirt.

Side-skirt basically prevents high momentum fluid flowing from side of trailer into the underbody of the vehicle in the upper region while in the lower region it is vice versa [20]. Since in this case the problem arises with the addition of an axle to tractor, it is reasonable to look into flow coming off the wheels/wheelhouse and underbody of truck. Regert and Lajos [15] have identified six vortices leaving the front wheel. The same has been proven by Krajnović et al. [8]. Investigation of propagation of these vortices downstream and their interactions with other elements like fuel tank, side pod and rear wheel is primary objective of this thesis. Along with this the influence of underbody flow on Side-skirt's performance must be first investigated. This allows us to isolate flow structures responsible for Side-skirt's enhanced performance in single axle condition. Later, this can be extended to dual axle condition.

2

Aerodynamic Background

2.1. Flow Physics

Side-skirts are in the wake of tractor rear wheel. More importantly, they experience flow emanating from the wheel patch and tractor underbody. Also, in the context of this thesis it is important to learn about flow features emanating from the wheelhouse which eventually seems to influence the side-skirt. The following sections discuss wheelhouse flow and some aspects of underbody flow. Due to limited research in this area, literature on rear wheelhouse flows is not found. Nevertheless, literature available on front wheelhouse is discussed hereinafter. Furthermore, some aspects of side-skirt and its behaviour is also discussed towards the end of this chapter.

2.1.1. Wheelhouse Flow

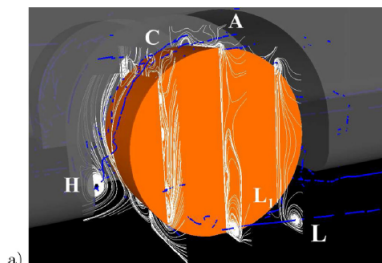
In this section the understanding of the flow coming off front wheel is highlighted and an overview of previous studies is given. Since the side-skirt is situated in the wake of the rear wheels as shown in figure 2.1 , it is assumed that the flow is influenced by both the front and rear wheel and also by some part of front bumper, headlamp cover and by some underbody elements. The presence of wheelhouse has a significant influence on direction and structure of the vortices leaving the wheels [15]. Figure 2.2a is the LES simulations conducted by Kra-jnović et al. [8] which gives an idea about vortex structures leaving wheelhouse. Figure 2.2b is the RANS simulations conducted by Regert and Lajos [15] and gives a much more comprehensive view (mention of direction of rotation of wheel vortices) of all the vortex structures.

Furthermore, the above figures represent vortices originating from front wheels but further investigations will be conducted during the thesis period on propagation of these vortices downstream and their interaction with vortices originating from rear wheels. Also, the influence of other elements such as sidepods, fuel tank and certain other bodies lying downstream of these vortices will also be investigated. An important point to be considered here is that all the above simulations were conducted on a simplified model as shown in figure 2.4 but in order to understand the cause of under-performing side-skirt CFD simulation must be conducted on a more realistic truck model.

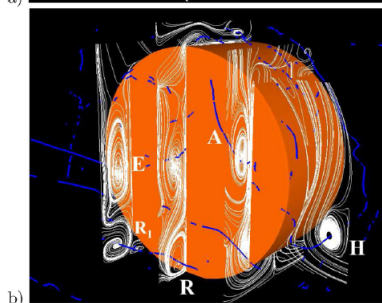
A study was conducted by Hobeika [7] on different rim configurations and tyre patterns (figure 2.3a). It was found that rim and spoke design influence drag significantly. Hobeika [7] also validated his CFD simulations experimentally on one of their rim configurations. Vdovin [23] also conducted accurate wind tunnel experiments with five belt system on different rim



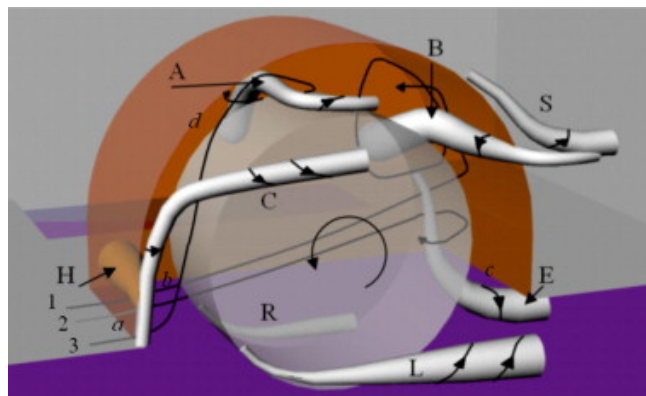
Figure 2.1: Region of Flow Investigation highlighted







a)



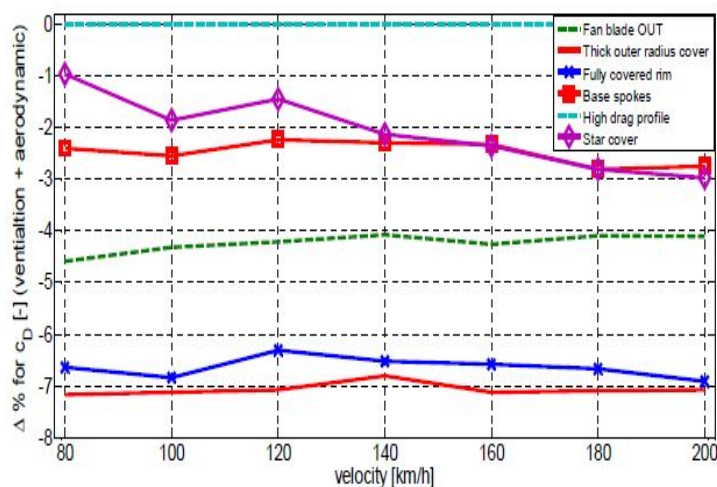
(a) Vortex cores and time averaged streamlines by [8]



(b) Vortex structures as found by [15]

Code	Rim Name	Picture
C	Creon	
CR	Creon Rotated	
O	Oden	
F	Flat	

(a) Rim configurations studied by [7]



(b) Normalized drag coefficient of rim configurations by [23]



Figure 2.4: Simplified truck model used by [15]

configurations. It was again proven that there is significant drag difference between basic fully covered rims (almost cylindrical wheel) and regular rims used on cars (figure 2.3b).

From Figure 2.2b it can be noticed that six vortices emerge out of wheelhouse. According to Scheeve [17] these dominant six vortices are qualitatively independent of grid, numerical scheme and shape of body. Whereas the strength and size vary with changing geometry but their presence remains. So, this will serve as a good first check in future simulations.

2.1.2. Underbody Flow

Another important region of flow which might influence the performance of Sidewing is underbody flow. It is also a region which has inevitable bodies which produce a lot of disturbance in flow. The wake of underbody elements which are in close proximity of side-skirt (rear wheel cover, transmission system etc.,) can also interact with side-skirt's flow and influence its performance. This fact must be investigated as there is no specific literature that could be found on it (in dual rear axle condition). Figure 2.5 shows the underbody flow as investigated by van Raemdonck [22] on a single axle condition. It is evident that a large recirculation region exists behind the rear axle and rear wheels. van Raemdonck [22] also stresses on the contribution of underbody drag relative to the total drag experienced by tractor-trailer combination. It is stated that tractor underbody contributes to 26% of the total drag of truck and the underbody of trailer contributes to 6% of total drag of truck [22]. So more than 30% of the total drag experienced by the truck is from underbody flow [22]. Since this low momentum region interacts with free stream on the sides of trailer, it disturbs the flow. Thus enclosing this region reduces drag.

This is achieved by side-skirts.

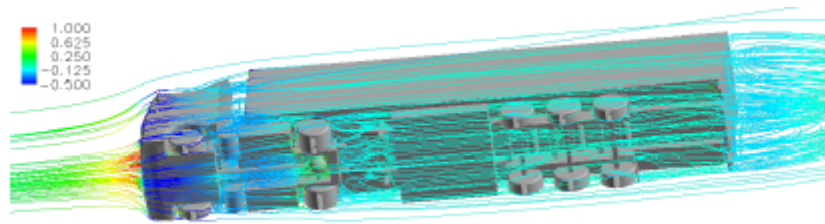


Figure 2.5: Underbody flow simulated by [22]

Furthermore, Scheeve [17] gave insights about the unsteadiness of the underbody/trailer side flow. This is the region involving the propagation of six vortices mentioned in the previous section. Figure 2.6 shows the variation of $C_{p_{tot}}$ at $Z/D = 0.5$, where D is the diameter of the wheel over two different iterations using RANS. It can be seen that there is not much variation in the flow beside the front wheel whereas there is large variation in front of the trailer wheel between two iterations. We can also observe a large variation in flow in the wake of the rear wheel. This shows that six primary vortices and underbody wakes are highly unsteady. Interestingly, Scheeve [17] did not recommend Unsteady simulations using URANS, as the unsteadiness in turbulence is not deterministic. Instead, he recommends DES simulations if computational resources are available.

Furthermore, it is worth discussing Stephens and Babinsky [20]'s results. They conducted PIV experiments on an 1:10 scale European truck model with side-skirts in a water tunnel. Stereoscopic and planar PIV were used in their experiments. Though their aim was to investigate flow around a side-skirt on a single rear axle (4X2) truck, they provided some qualitative results which can be expected in dual axle condition too.

It can be seen from figures 2.7 and 2.8 that side-skirt prevents the underbody flow from entering the freestream flow. This prevents the wake originating from the wheels to slow down further (as in no side-skirt case). Thus preventing the increase in velocity deficit along the sides of truck. This is substantiated by the velocity contour plot shown in figure 2.9a and 2.9b in a streamwise plane ($x/b=2.51$ plane, b -width of vehicle).

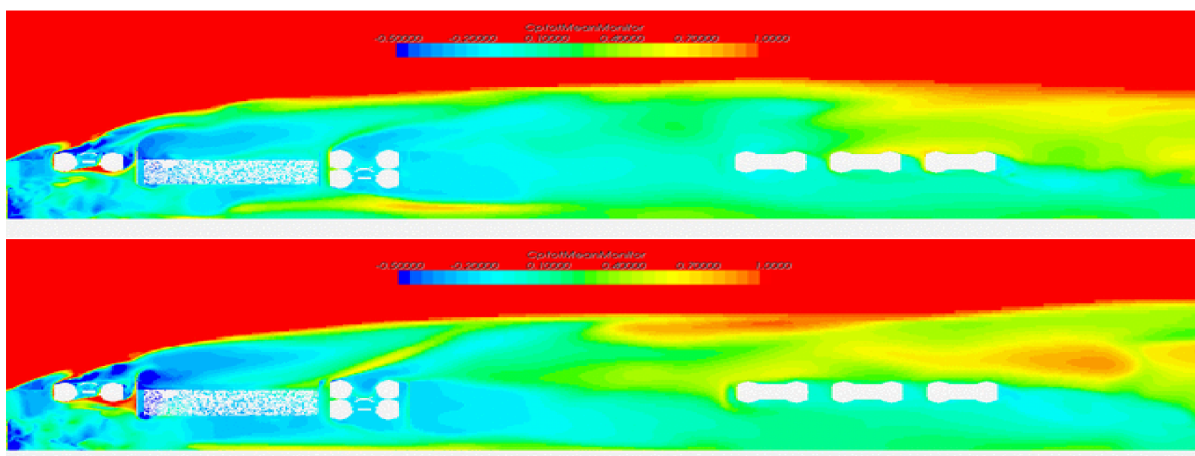


Figure 2.6: Underbody flow by Scheeve [17] (steady state) at two different iterations. Plots of C_{p_t} at $Z/D = 0.5$

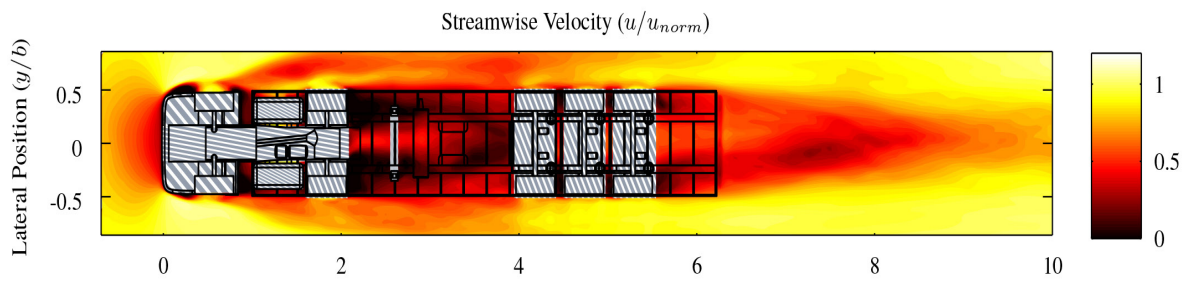


Figure 2.7: Underbody normalized Velocity contour for **no side-skirt** case by Stephens and Babinsky [20], $Z/b = 0.16$, horizontal plane

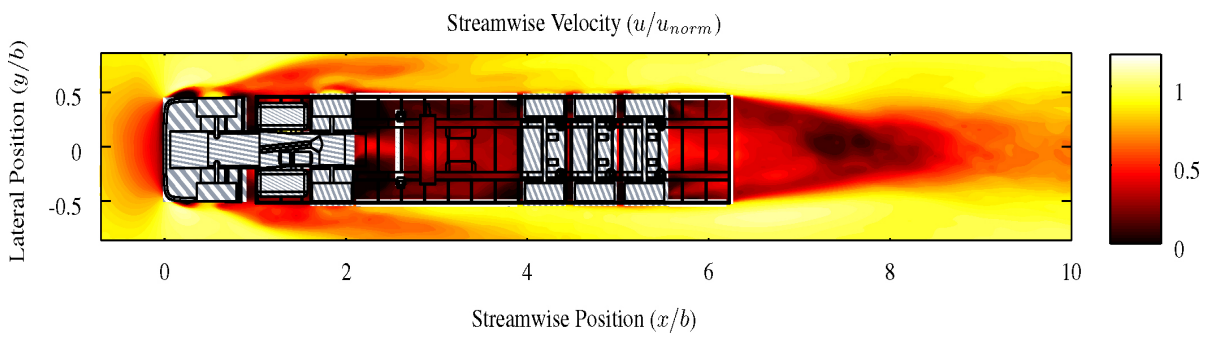


Figure 2.8: Underbody normalized Velocity contour for **side-skirt** case by Stephens and Babinsky [20], $Z/b = 0.16$ (b =width of truck), horizontal plane

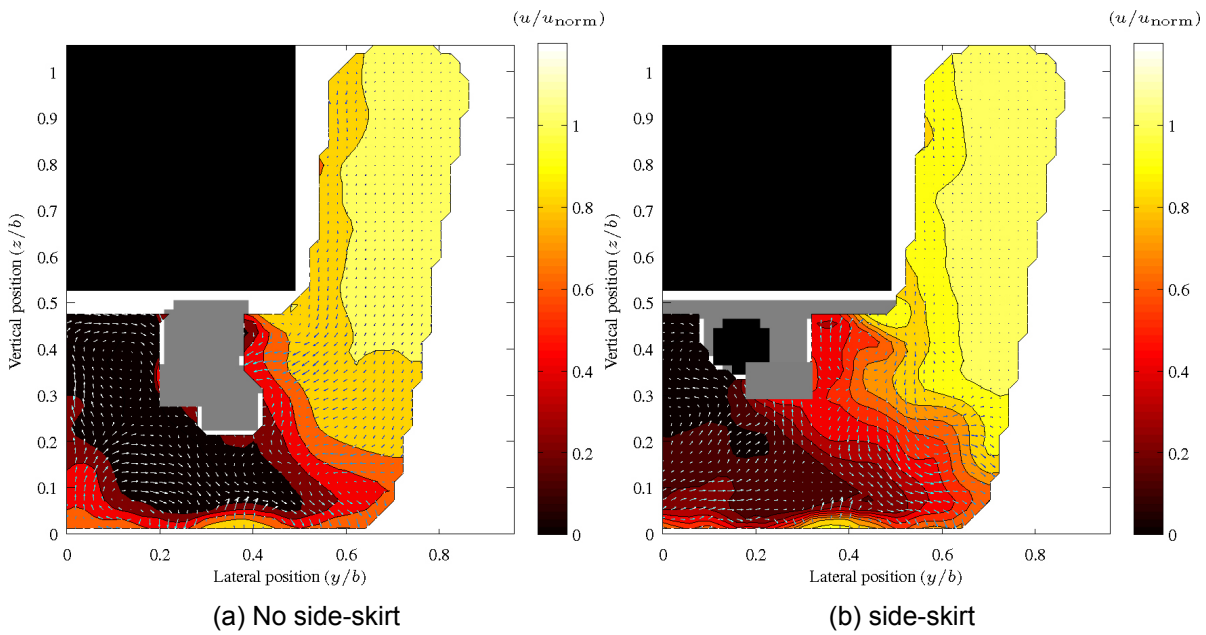
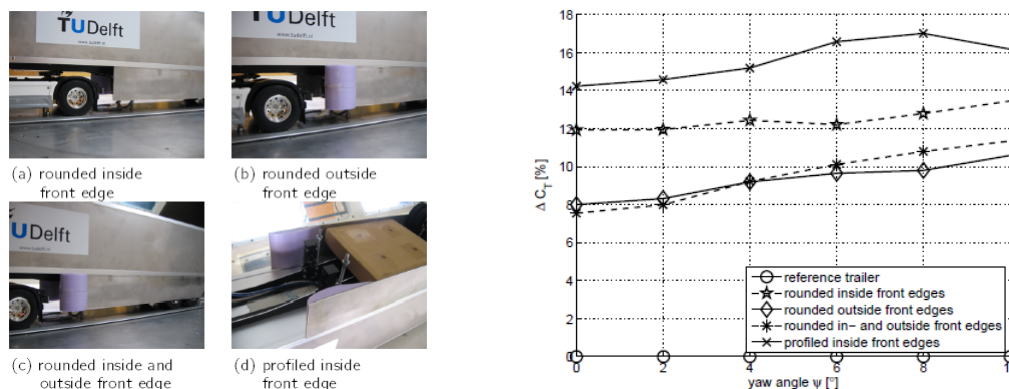


Figure 2.9: Velocity Contour in $x/b=2.51$

2.1.3. Performance Study of WABCO-OptiFlow's SideWing™

To understand the performance of side-skirts better van Raemdonck [22]'s work was studied. Various shapes of straight skirt were studied by van Raemdonck [22]. All the shapes were simulated in Low Turbulence tunnel at different yaw angles on a stationary ground plate. The different shapes tested are shown in figure 2.10a.



(a) Different shapes of straight skirt tested by [22] (b) Drag reduction results of skirts ([22])

Profiled inside front edge is currently SideWing™. It has an airfoil profile at the beginning of the skirt to avoid flow separation at high yaw angles. All the shapes were tested at different yaw angles.

From figure 2.10b where change in wind averaged drag coefficient (ΔC_T) with respect to reference trailer case is plotted, it can be understood that the airfoil profiled skirt performs well at all yaw angles while providing a drag reduction of 14% at zero deg yaw angle.

2.1.4. Full Scale tests with Side-skirts

To further validate the design, side-skirts were tested by van Raemdonck [22] on both track and road. The road test was a four week road test on selected routes. During these tests fuel consumption was measured. The track test results showed that side-skirt reduced the fuel consumption by 4.6% in tail wind and by 13.6% in head wind. Furthermore, the road tests also confirmed this where a 9.29% fuel consumption reduction is observed over the entire trip.

2.2. Research question, aims and objectives

The main research questions that can be formulated after last section are,

1. What is the influence of six vortices coming off the front wheelhouse and underbody flow on side-skirt's performance?
2. How are the six principle vortices affected by rear wheelhouse flow?
3. What are the flow features originating from the rear wheelhouse and what is their influence on side-skirt's performance?
4. What is/are major flow feature differences between single (4X2) and dual(6X4) axle condition? Which of them really affect the performance of side-skirt? How do these flow features change in the presence of side-skirt in the respective configurations (single and dual rear axle configurations)?

3

Theoretical Methodology

Due to complexities involved in the region of interest (figure 2.1), it was decided very early in this project to not resort to any experimental methods. This decision was taken as the complex wind tunnel models required would be expensive. For example, the main difficulty in this case is arranging a moving belt for the length of the truck. At T U Delft, there are no moving belt wind tunnels of the scale that can accommodate a scaled model of truck. Secondly, the amount of pressure taps required on this model would make it even more expensive. Thus, only CFD is used in this project to evaluate the flow field between the rear wheel and the side-skirt. The following section describes the numerical set-up

3.1. Numerical Set-up

In this section a brief review of CFD preparation and turbulence model used will be discussed. Furthermore, the capabilities of RANS¹ and DES² will be evaluated in this section to understand their ability to predict local separation accurately. Finally, choice of cell type, wall modelling and rotation flow modelling will be discussed towards the end of this section.

3.1.1. CFD Approach

Going by Scheeve [17]'s recommendations, it is evident that the region of interest we are looking at is highly unsteady because of numerous separated regions. Thus a deeper look into CFD approaches which can predict separation better is conducted in this section. Two approaches RANS and DES are discussed here.

Sreenivas et al. [19] conducted simulation using $k - \epsilon$ and $k - \omega$ models with and without DES modifications on a GTS (Generic Transport System) model. Overall drag was within 10% of experimental value for both models but the DES model predicted asymmetric vortices in the wake of the truck (closer to experimental result). Figure 3.1 shows the results obtained by them. Sreenivas et al. [19] also suggest that with further fine tuning DES approach can produce even accurate results.

¹Reynolds Averaged Navier Stokes

²Detached Eddy Simulation

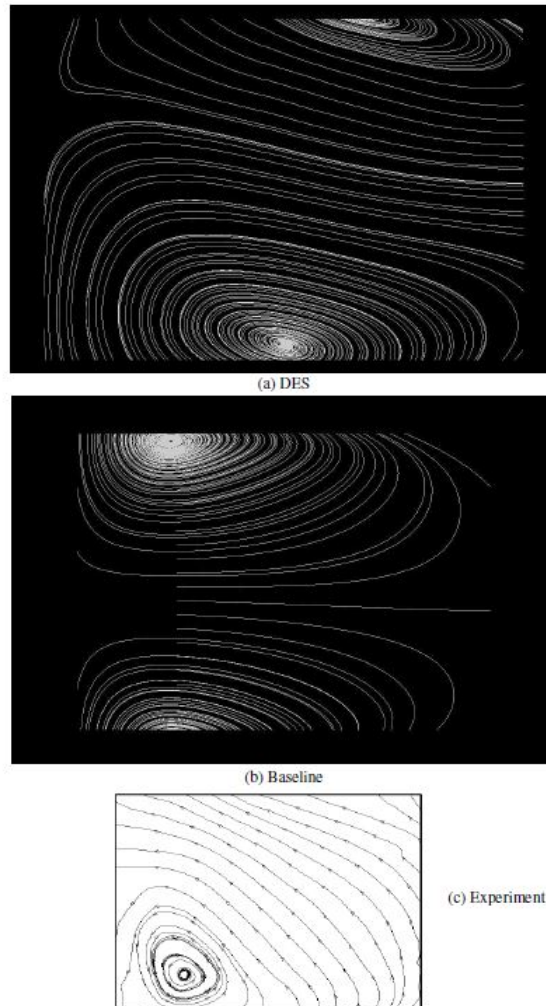


Figure 3.1: DES/RANS base wake prediction (Baseline refers to RANS)

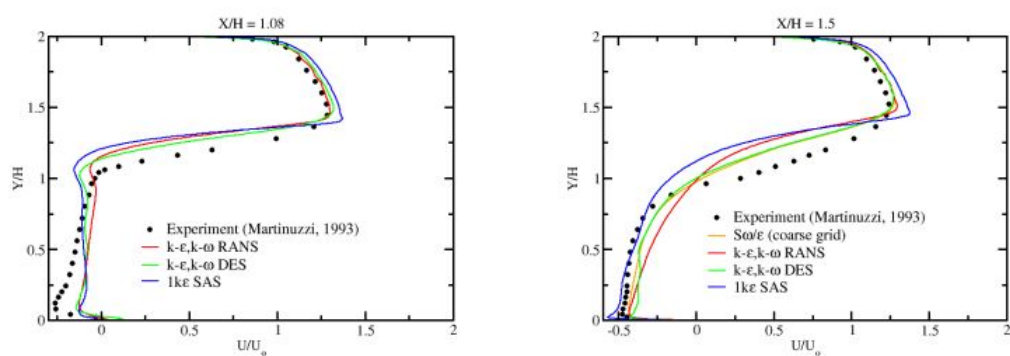


Figure 3.2: DES/RANS wake prediction behind a cube

Furthermore, Nichols et al. [11] conducted similar studies on a surface mounted cube. They too found out that DES model predicts flow structures well in the separated region. They compared axial velocity in the center plane (figure 3.2). It can be noticed that although DES is more accurate than RANS, the RANS approach is not quite far from experimental value.

Since DES approach requires higher mesh resolution away from the wall (to resolve smaller scales via LES approach), it will be computationally expensive to simulate our region of interest behind the rear wheel of tractor with a complex, reasonably detailed model. Although RANS is inaccurate in the base wake region it is still preferred over DES approach in this thesis. This is based on a trade-off between accuracy and computational effort. This decision is also motivated by the fact that the highly influential flow features around a truck are characterised by large time-scales and length scale comparable with the length of the truck. RANS is capable of predicting such flow features with reasonable accuracy as long as the time-step is greater than mean turbulent time-scale and less than time-scale of one cycle of oscillation.

3.1.2. Reynolds Averaged Navier Stokes (RANS)

Reynolds Averaged Navier Stokes approach considers the decomposition of flow quantities into mean and fluctuating components equation 3.1. The mean components (\bar{u}) are computed while the fluctuating components (u') are modelled.

$$u_i = \bar{u}_i + u'_i. \quad (3.1)$$

substituting this decomposition in the incompressible Navier Stokes equation and taking time average, we get continuity and momentum equations which are similar to incompressible NS equations with some additional terms that needs modelling.

$$\frac{\partial \bar{u}_i}{\partial x_i} = 0, \quad (3.2)$$

$$\rho \frac{\partial \bar{u}_i}{\partial t} + \rho \frac{\partial (\bar{u}_i \bar{u}_j)}{\partial x_j} = -\frac{\partial \bar{p}}{\partial x_j} + \frac{\partial \bar{\tau}_{ij}}{\partial x_j} - \frac{\partial (\overline{\rho u'_i u'_j})}{\partial x_j}, \quad (3.3)$$

where $\bar{\tau}_{ij}$ and $\overline{u'_i u'_j}$ are mean stress tensor and Reynolds stress tensor respectively. The latter is the one that needs to be modelled. In ANSYS Fluent, Boussinessq approximation is used to obtain relation between Reynolds Stress and mean velocity gradients and turbulent kinetic energy (κ)

$$-\overline{\rho u'_i u'_j} = \mu_t \left(\frac{\partial \bar{u}_i}{\partial x_j} + \frac{\partial \bar{u}_j}{\partial x_i} \right) - \frac{2}{3} \left(\rho \kappa + \mu_t \frac{\partial \bar{u}_k}{\partial x_k} \right) \delta_{ij}. \quad (3.4)$$

3.1.3. Turbulence Modelling

According to Scheeve [17] the $k-\omega$ SST turbulence model seems to be the appropriate choice for this kind of flow as it behaves well in adverse pressure gradient and in predicting local separation. Even SAE Standard J2966 on heavy vehicles CFD[16] suggests the same. Scheeve [17] suggested that $k-\omega$ SST model had excellent agreement of drag coefficient with experimental values. Also the wall function approach in $k-\omega$ SST model saves computation time.

Furthermore, as there was no experimental data to compare the vortex structures results, Scheeve [17] plotted isosurfaces of Q-criterion and total pressure of different turbulence models simulated on same geometry and compared the results. It was found that $k-\omega$ SST model predicted the vortex structures reasonably well.

$\kappa - \omega$ SST

In this section the formulation of $k - \omega$ SST will be discussed. Firstly, the κ and ω transport equations are as follows,

$$\frac{\partial \rho \kappa}{\partial t} + \frac{(\rho \kappa u_i)}{\partial x_i} = \frac{\partial}{\partial x_j} \left(\Gamma_\kappa \frac{\partial \kappa}{\partial x_j} \right) + G_\kappa - Y_\kappa + S_\kappa, \quad (3.5)$$

$$\frac{\partial \rho \omega}{\partial t} + \frac{(\rho \omega u_i)}{\partial x_i} = \frac{\partial}{\partial x_j} \left(\Gamma_\omega \frac{\partial \omega}{\partial x_j} \right) + G_\omega - Y_\omega + S_\omega. \quad (3.6)$$

where G , Y and S are corresponding Production, Dissipation and Source terms while Γ represents effective diffusivity of κ and ω . They are further elaborated in Appendix A.

3.1.4. Wall Modeling

From the law of wall it is understood that the non-dimensionalized velocity u^+ behaves differently with non-dimensionalized y^+ in different regions of viscous layer. For $y^+ < 5$ (laminar sublayer), u^+ varies linearly with y^+ , whereas for $y^+ > 30$, u^+ varies logarithmically with y^+ . It is advised that resolving the region $y^+ < 5$ gives better results [25].

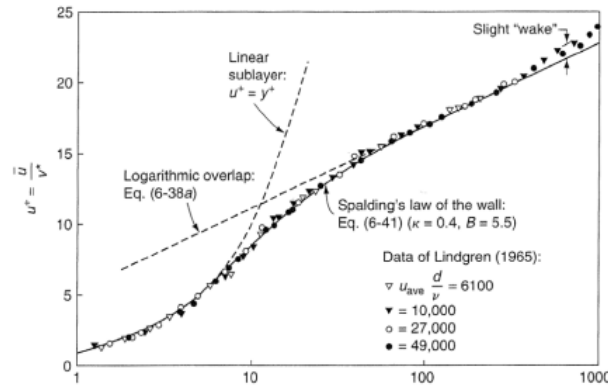


Figure 3.3: Behaviour of the boundary layer in the vicinity of the wall[24]

ANSYS Fluent two equation RANS models the flow near the wall based on wall function approach. The wall function approach does not resolve viscous sub-layer instead it models it based on empirical relations as given below,

The specific dissipation rate (SDR) at the wall is specified by equation,

$$\omega_w = \frac{\rho(u^*)^2}{\mu} \omega^+, \quad (3.7)$$

The above equation is computed by the following ω^+ definitions which are based on viscous sublayer and logarithmic layer. One of these formulations is chosen based on the first grid point off the wall[2].

$$\omega^+ = \frac{6}{\beta_i (y^+)^2}, \quad (3.8)$$

$$\omega^+ = \frac{1}{\sqrt{0.09}} \frac{du_{turb}^+}{dy^+}. \quad (3.9)$$

3.1.5. General Scalar Transport Equation

In this section a general scalar transport equation and its discretised version are introduced in order to explain discretisation scheme in the following sections.

$$\int_V \frac{\partial \rho \phi}{\partial t} dV + \oint \rho \phi \vec{v} \cdot d\vec{A} = \oint \Gamma_\phi \nabla \phi \cdot d\vec{A} + \int_V S_\phi dV. \quad (3.10)$$

Discretised Version for a cell

$$\frac{\partial \rho \phi}{\partial t} V + \sum_f^{N_{faces}} \rho \phi_f \vec{v}_f \cdot \vec{A}_f = \sum_f^{N_{faces}} \Gamma_\phi \nabla \phi_f \cdot \vec{A}_f + S_\phi V, \quad (3.11)$$

Reducing the equation 3.11 into steady state incompressible form,

$$\sum_f^{N_{faces}} (\rho \vec{v}_f \phi_f - \Gamma_\phi \nabla \phi) \cdot \vec{A}_f = S_\phi V, \quad (3.12)$$

Linearized Version

In Fluent, the non-linear discretised transport equation is linearized so that it can be solved using linear system of equations involving sparse matrices.

$$a_p \phi = \sum_{nb} a_{nb} \phi_{nb} + b. \quad (3.13)$$

where subscript nb refers to neighbour cells and a_p and a_{nb} are linearized coefficients of ϕ and ϕ_{nb} . For more information on the coefficients and the linearization please refer to Appendix B

3.2. Discretisation Schemes

3.2.1. Spatial Discretisation

In a finite volume method like the one used in ANSYS Fluent, cell values are stored at the centroid of the cell but to compute convective terms, face values are required. In order to do so, cell values are interpolated using discretisation schemes. In this thesis, the author used second order upwind schme for all terms except diffusive terms in the discretised equation. As diffusive terms are discretised using central-differencing scheme by default. Although, at the beginning of the simulation, first order upwind scheme is employed and later switched after few iterations.

Second Order Upwind (SOU)

In this scheme, face values are interpolated from the cell values using a Taylor's series expansion.

$$\phi_f = \phi + \nabla \phi \cdot \vec{r} \quad (3.14)$$

where,

- ϕ_f face value of the corresponding cell.
- ϕ cell centre value
- $\nabla \phi$ gradient computed in one of the upstream cells
- \vec{r} position vector from cell centroid to face centroid.

Central-Differencing Scheme

As discussed earlier, diffusive terms are discretised using this scheme, hence its formulation is discussed here. Furthermore, even face values of Pressure are also computed from their cell centered values using the same scheme.

$$\phi_f = \frac{1}{2}(\phi_0 + \phi_1) + \frac{1}{2}(\nabla\phi_0 \cdot \vec{r}_0 + \nabla\phi_1 \cdot \vec{r}_1), \quad (3.15)$$

Where, all the quantities have similar definition as prescribed in the last section except that the subscripts "0" "1" indicate quantities from face sharing cells. The main difference in this scheme is the evaluation of gradients, here gradients are reconstructed using cell centered values of face sharing cells whereas in SOU, Least square cell based gradient evaluation scheme is used which will be discussed later in next section .

3.2.2. Gradient and Derivative Evaluation

Least Square cell based gradient In this method, the relation between gradient of a cell and its cell values with respect to one of the neighbouring cells is expressed as,

$$(\nabla\phi)_o \cdot \Delta r_i = \phi_0 - \phi_1, \quad (3.16)$$

Writing the above equation for each neighbouring cell (each face), we get a system of linear equations,

$$[J][\nabla\phi]_o = \Delta\phi. \quad (3.17)$$

Solving the above system of equation in a least square sense yields the derivative at cell centers. Furthermore, least square cell based gradient method is accurate on irregular meshes (skewed and distorted) and it's accuracy is comparable with node-based gradient method which is considered to be most accurate.

3.2.3. Temporal Discretisation

The time term in discretised general transport equation must be discretised just like the other terms. In this thesis, a first order implicit scheme is used. This backward difference scheme is implicit in nature and thus the RHS ($F(\phi)$) is evaluated at the future time level $n + 1$. Implicit schemes are unconditionally stable when compared to explicit schemes.

$$\frac{\phi^{n+1} - \phi^n}{\Delta t} = F(\phi^{n+1}). \quad (3.18)$$

This scheme was used because it allows large timesteps by running at high Courant numbers (200). This allows large physical time runs (> 10 s) with fewer timesteps as most of the flow features around the truck have large time scales.

3.2.4. Final Discretised System (Linearized)

The linearized momentum equation can be obtained by substituting $\phi = u$ in equation 3.13,

$$a_p u = \sum_{nb} a_{nb} u_{nb} + \sum_{nb=f} P_f A \cdot \hat{i} + S. \quad (3.19)$$

Furthermore, the discretised continuity equation is defined as follows, where J_f is the mass flux through face f .

$$\sum_f^{N_{faces}} J_f A_f = 0. \quad (3.20)$$

3.3. Solver Algorithm

A Coupled Algorithm is used in this thesis. In this algorithm momentum and pressure-based continuity are solved simultaneously in a full implicit way unlike other segregated algorithms like *SIMPLE* and *SIMPLEC*. The main idea behind choosing this algorithm is that it allows large time steps and can treat skewed cells appropriately[2]. Furthermore, in steady state simulations (used to initiate unsteady simulations) it allows faster convergence. For more information about this algorithm refer to Appendix B

The algorithm is outlined as follows,

- Starting with n^{th} iteration values $(\dot{m}_f^{(n)}, v^{(n)}, p^{(n)})$.
- Solve momentum and continuity equations for v^* and p^* .
- Compute the corrected mass flow rate (\dot{m}_f^*) (or flux) using Rhie-Chow interpolation.
- Compute other scalar quantities like κ and ω .
- Return to first step and iterate until convergence.

3.4. Truck Model Profile

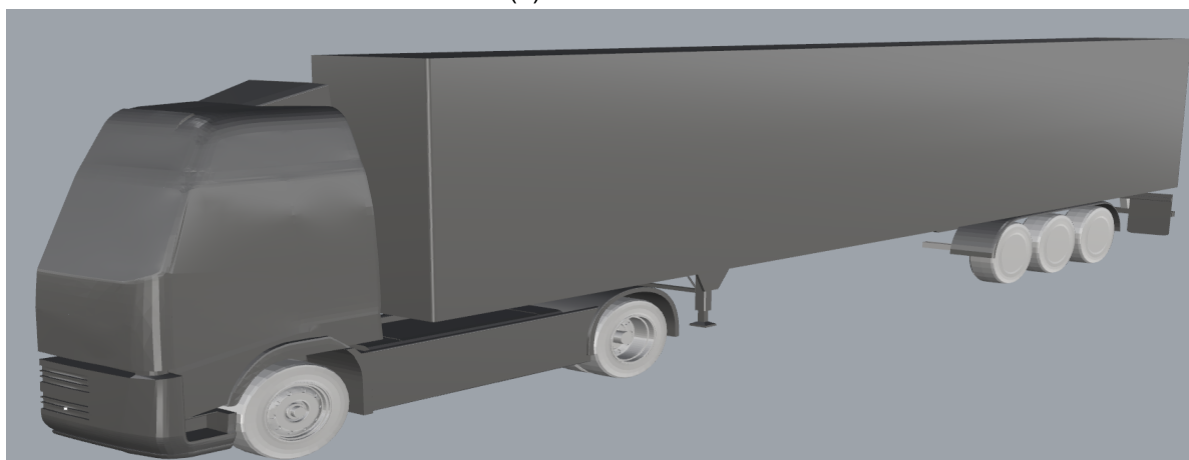
This section introduces the truck model used in this thesis and the modifications made to it in the process of simplifying it. For example, Mirrors are eliminated as they are away from the region of interest and they simply add to the complexity. Both models are illustrated in figures 3.4a and 3.4b. Some underbody components like suspension are simplified as shown in figures E.1a and E.1b. The simplification was an intuitive process where small elements whose width in the streamwise direction was not significant are eliminated. Furthermore, the dimensions of 4X2 and 6X4 configurations studied in this thesis are depicted in figures 3.5a and 3.5b. The total wheelbase of both the configurations is kept at 3.8m and the additional axle is added in front the pre-existing one. The distance between these axles is about 1.3m. These are dimensions commonly seen with many truck manufacturers.

Table 3.1: Truck Dimensions

Dimension	Length (m)
Truck Length, L	16.5
Height of Truck, H	4.0
Width of Truck, W	2.55
Distance between front and rear axles, L_{axles}	3.8
Distance between rearmost wheel and side wing, L_{RW-SW}	1.0

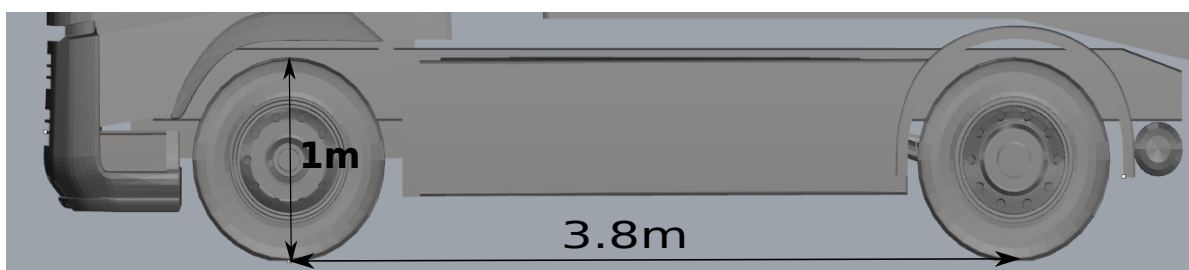


(a) Volvo FH-13

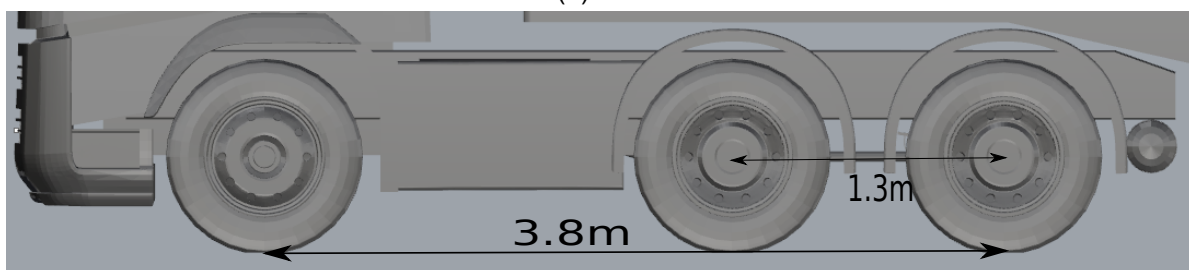


(b) Simplified Volvo FH-13(half model)

Figure 3.4: Truck Model



(a) 4X2



(b) 6X4

Figure 3.5: Configuration Studied

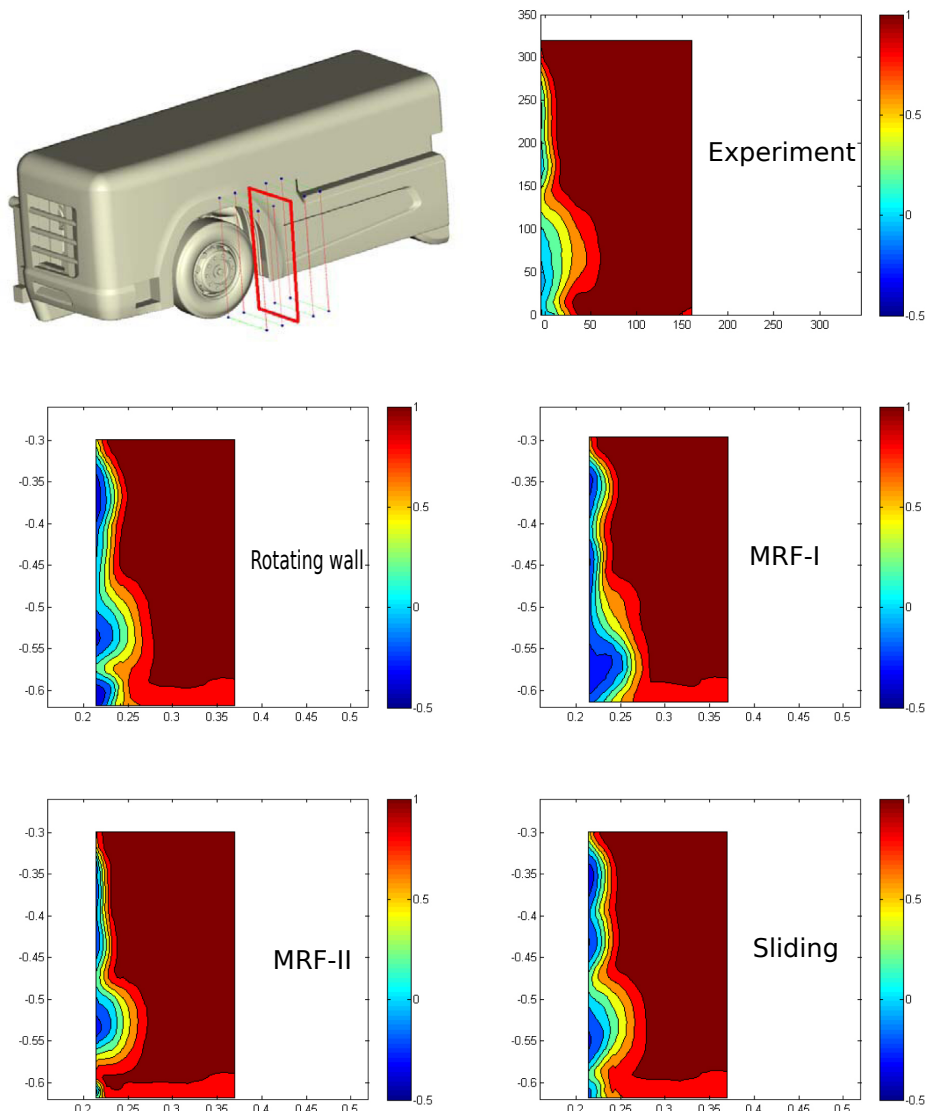


Figure 3.6: Coefficient of total pressure in a plane located 100 mm behind the wheel axle. From top left: Location of measurement plane, experimental results, Rotating Wall, MRF I, MRF II and Sliding Mesh.

3.5. Rotating Flow Modeling

As our region of interest is profoundly affected by rotating wheels, modelling them appropriately is important. Söderblom et al. [18] conducted simulations on wheelhouse flow using different methods to model rotating flows. They compared Rotating Wall, Moving Reference Frame³ and Sliding mesh (unsteady simulation). The authors compared pressure coefficient on inner, mid and outer planes of wheelhouse with experiment. All techniques had good agreement with experiment in inner plane while some techniques were way off in mid plane and outer plane. Although all the techniques were quite close in pressure prediction. A large difference was seen between them in total pressure coefficient plots on a plane right behind the wheel as shown in figure 3.6.

All techniques have their own flaws in predicting the flow features, ultimately the choice comes down to ease of use. Rotating wall seems to be the easiest since it does not require multiple domain meshing like in other techniques. This eventually reduces meshing and

³Stationary and moving parts are meshed as separate domains

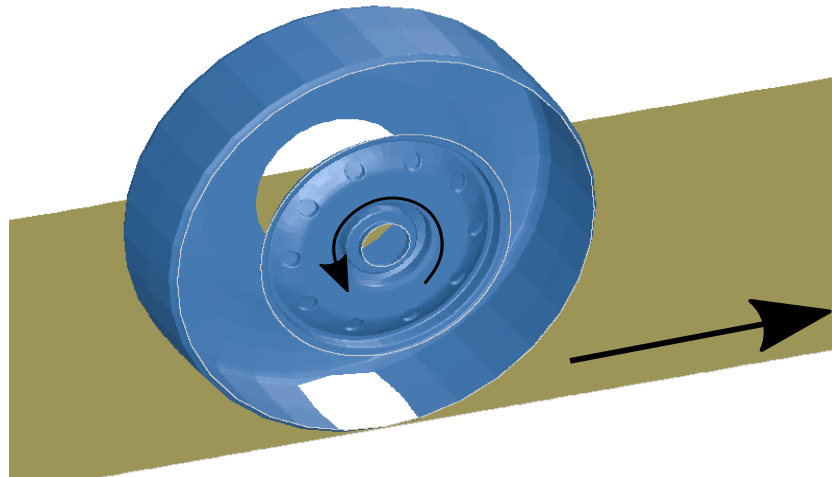


Figure 3.7: Rotating Wheel Implementation. Wheel cut off 2mm at the bottom to emulate wheel patch. The cut-off edges are joined with ground plane

turnaround times. Thus, rotating wall technique is used in this thesis as shown in figure 3.7

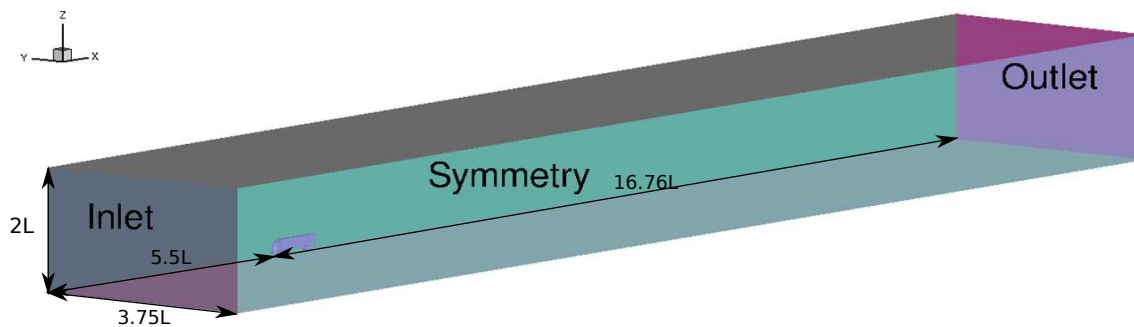
3.6. Domain Sizing and Boundary Conditions

The dimension of the domain are chosen based on the recommendation by SAE standard J2966[16] on truck aerodynamics. They suggested a downstream length of 5 – 8 times the length of the truck. This smaller domain resulted in unstable simulations due to reverse flow. This meant that the outlet is too close to the wake box of the truck. Thus a longer domain is chosen for future simulations whose dimensions are based on the ones used by Scheeve [17]. The domain ultimately used in this thesis are shown in figure 3.8.

Furthermore, the boundary conditions used on this domain are given in table 3.2. The Inlet is defined by a constant velocity of 25m/s and the outlet was kept at atmospheric pressure (101325Pa). The mid-plane is given the symmetry boundary condition as only the half model is studied in this thesis. The rest of the domain's walls including the ground plane are defined as moving walls with tangential velocity of 25m/s . This condition eliminated any gradients near these walls if a stationary wall is used. All the surfaces of the truck are stationary except the wheels. the wheels are given an angular velocity of 50rad/s , this meant that the linear velocity at the periphery of the wheels is 25m/s . This ensured a nice flush of boundary conditions avoiding any redundant or multiple velocity definitions at the intersection of wheels and ground plane.

Table 3.2: Overview of Boundary Conditions

Boundary	Value
Inlet	$V = 25\text{m/s}$ (normal)
Outlet	$P = 101325\text{Pa}$
Wheels	$\omega = 50\text{rad/s}$
Ground Plane	$V = 25\text{m/s}$ (tangential)
Bounding Box Walls	$V = 25\text{ m/s}$

Figure 3.8: Domain size, $L = 16.5m$

3.7. Type of Cells

Scheeve [17] compared tetrahedral and polyhedron cells. Tetrahedrons are best suited for rotating flows or flow where main direction of flow is not orthogonal to faces of cells. The comparison between these two cells suggests that polyhedron cells yield results with similar accuracy for a lesser number of cells but are computationally expensive. This is because each polyhedron element has more neighbouring cells compared to tetrahedrons. But in our case since a lot of intricate features had to be captured in the region of interest, tetrahedrons seem expensive and thus keeping in mind the computational resources available at TU Delft Cluster polyhedron cells are chosen. Due to the limited computational power Scheeve [17] chose hexahedral cells for his simulations.

3.7.1. Polyhedron Cells

Peric and Ferguson [14] (main article Peric [13]) of *Cd-adapco* in one of their articles suggests that the major advantage of polyhedron cells is that they have many neighbours, so gradients can be much better approximated (using linear shape functions and the information from nearest neighbours only) than in the case with tetrahedron cells. Polyhedron cells are also less sensitive to stretching than tetrahedrons. Furthermore, they mention that polyhedrons are especially beneficial for handling recirculating flows. Since most of the flow phenomena that we are expecting in our case involves recirculating flows, it is suitable to use polyhedrons.

The reason behind choosing polyhedron cells at this stage is well explained by Symscape [21]'s case study on polyhedron, tetrahedral and hexahedral cells. The study was conducted on *backward facing step* as shown in figure 3.9. They compared the volume element count, convergence, accuracy and runtime of all three types of cells.

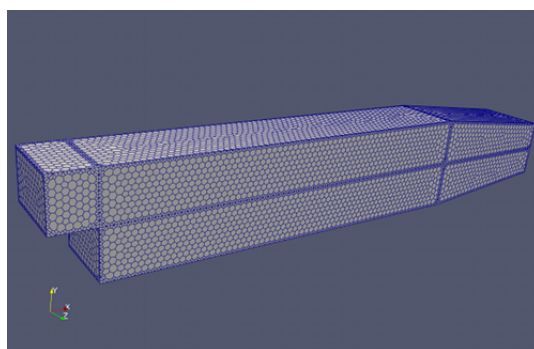


Figure 3.9: 3D model as used by simscape

Tetrahedral cells needed the highest number of volume cells to fill the whole volume followed by hexahedral and polyhedron cells as shown in figure 3.10a. The reason for least polyhedron cells is because they are formed from tetrahedral mesh by forming polygons around each node in the tetrahedral mesh. Thus a polyhedron element is basically a combination of several tetrahedrons. Hence, the reduction in number of cells.

Furthermore, polyhedrons also showed a very high order of convergence compared to other two cell types. Simscape compared the pressure residuals of each type of element in the figure 3.10b. Polyhedrons have a higher order of convergence than tetrahedrons and a similar convergence rate with hexahedrons. Symscap [21] also compared the number of iterations needed by each element type to reach an absolute residual of 1×10^{-4} in figure 3.10c. It again gives a solid proof that polyhedrons require least iterations to reach that residual value.

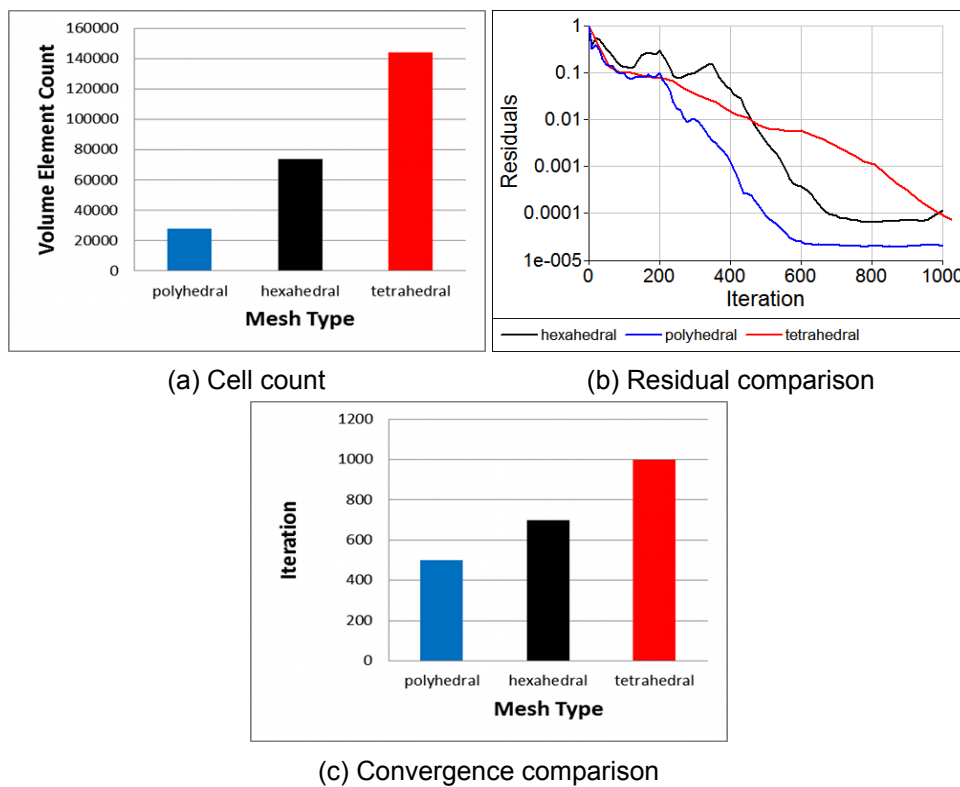


Figure 3.10: Cell Type Comparison-I

The accuracy of the simulations was compared by Symscap [21] by comparing the pressure drop between front and back of the step model. From figure 3.11a it can be noticed that all three cells reach a steady state value. A plot of number of iterations required by each cell type to reach the steady state value is given in figure 3.11c. Polyhedrons seem to reach the steady value with least number of iterations. Thus a faster convergence can be achieved with no compromise in accuracy. Final comparison included the runtime of simulations of each type of cells. Going by above data it is evident that polyhedrons take the least amount of time to reach convergence. This is illustrated in figure 3.11b where runtime are scaled with tetrahedron element runtime. Polyhedrons astonishingly take 70% less time to reach convergence compared to tetrahedrons. This is a major factor for choosing them.

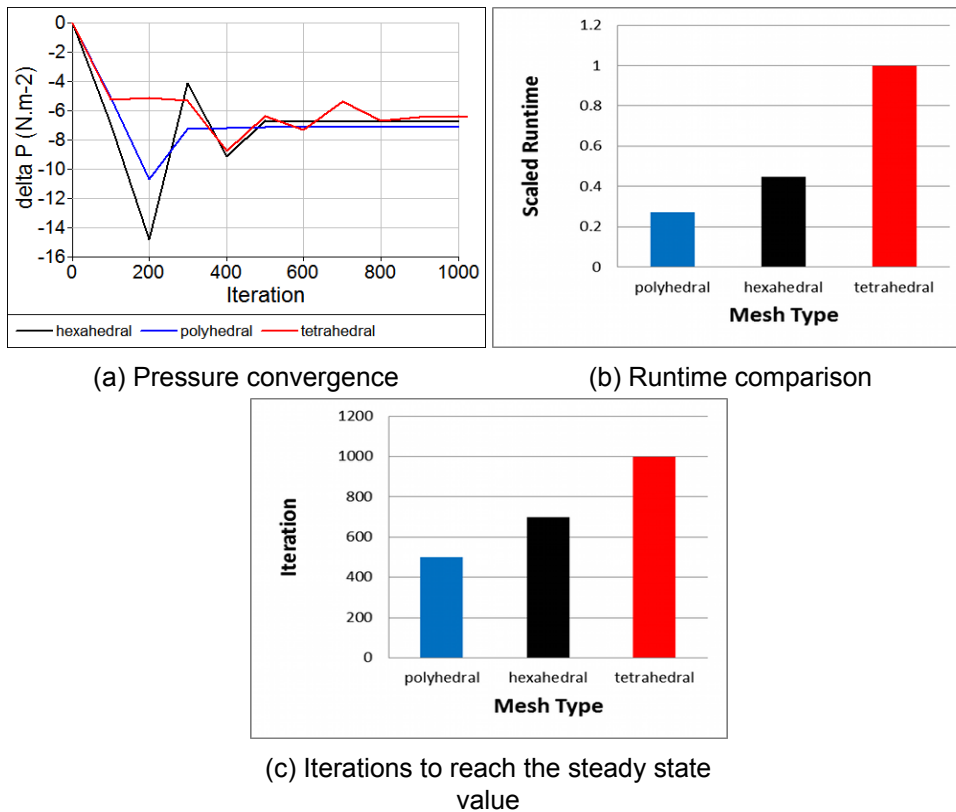


Figure 3.11: Cell Type Comparison-II

3.8. Physical Run Time

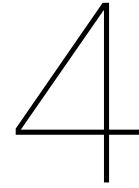
During grid convergence study (Chapter 4) using steady state simulations, abrupt or no convergence was found. In other words the results obtained did not show any convergence. Thus, at this point it was decided to switch to unsteady simulations. Since Unsteady simulations will be run for four principal cases (single and dual axle with and without side-skirt), it necessary to know what should be the time-step and what is the physical run time required to capture all the flow features. Elofsson et al. [6] conducted simulations on realistic model (in yaw) and simplistic model (no-yaw) conditions. They suggested that in yawed case one complete oscillation spans for about 4s whereas in no-yaw condition it is about 10s. Running a simulation for 5 convective cycles of 10s each is an impossible task considering the limited capabilities of TU Delft Cluster. Thus averaging techniques are looked into. The important technique used to average unsteady simulations is moving average, wherein only certain number of samples are considered out of pool of samples to compute the mean. Elofsson et al. [6] suggested that 4s of averaging window is good enough to obtain a drag coefficient within a confidence range of ± 0.002 . This seems to be an acceptable accuracy since we are expecting a drag difference of about 14% (± 0.1) (van Raemdonck [22]) between side-skirted and baseline (non side-skirted) cases. Thus, a 4s averaging window is chosen, the implications of this choice are further discussed in section 5.3.

Furthermore, the time step is chosen to be 0.15ms (milli seconds) as the constant size with a maximum Flow Courant number of 200. This allows larger time steps and hence, large physical runtime with fewer time steps. An adaptive time stepping algorithm is also used in order to obtain larger physical run time wherein the timestep is adapted based on a tolerance set for truncation error (ANSYS [2]). The timestep is allowed to vary between 0.1ms to 0.4ms.

Using these settings a physical runtime of 11s was achieved for each simulation.

3.9. Summary of Numerical Set-up

- The four principal configurations (single and dual axle with and without side-skirt) are simulated in an unsteady manner using URANS approach.
- All simulations are conducted in no-yaw condition with a freestream velocity of 25m/s. This is the highway speeds achieved by trucks.
- The rotating wheel is modelled by assigning rotational velocity to the wheel surface. The intersection of wheel and ground have similar velocity.
- All simulations are conducted using ANSYS Fluent in parallel combination using at least 200 Intel Xeon processors.



Mesh Sensitivity

In this section the surface mesh sizing of different components along with refinement box sizing for volume cells is discussed. Towards the end of the chapter a grid convergence study is also presented.

4.1. Meshing Strategy

The surface mesh is initially generated using appropriate size controls namely curvature, proximity and soft in order to ensure that geometric features are accurately represented. The simplified model from *Rhinoceros™* is imported into *Fluent TGrid Meshing* in Rhinoceros native format called *.3dm*. Furthermore, a thorough geometry cleaning is conducted in order to obtain a water-tight model. Later, a surface mesh is obtained using the different size controls which are elaborated in Appendix C. During the surface mesh process shrink wrap technique is extensively used to obtain the water-tight model from CAD import. This surface mesh is later re-meshed using a coarser size field as shrink wrapping requires finer mesh resolution in order to capture intricate geometric features.

Furthermore, polyhedral volume cells are generated using appropriate refinement boxes around the truck model to capture flow features appropriately. Along with polyhedral cells, prism layers are also grown close to the wall. Prism layers are cells laid normal to wall in order to model boundary layer. Since in this thesis wall functions are utilised, the first point off the wall can be placed in such a way that it lies in logarithmic region. In other words, the maximum y^+ on the truck is kept within 100 [16].

4.1.1. Mesh constraints

In order to obtain high quality mesh, certain size constraints are imposed. Firstly, in order to limit y^+ of 100 on the truck surface (figure 4.1). The first-off grid point was placed at $1mm$ from the wall. This size was decided after iterating with certain steady state runs. Another constraint laid on the first cell off the wall is the aspect ratio requirement. The aspect ratio of prism layers is kept at around 50 for mid-layers while layers close to wall had higher aspect ratio. This limited the maximum surface edge length to $50mm$ on truck components. This especially had an impact on the surface edge length size of trailer faces.

The number of prism layers needed is decided based on the flat plate theory. The truck is considered to be a flat plate of equivalent length and the flat plate boundary layer thickness equation is employed to compute the height of boundary layer at the end of the truck. Since

trailer top surface is in direction of free stream flow and there are no obstructing elements, it can be deduced that the maximum boundary can be seen on trailer top surface. Hence, maximum layers are needed on top surface of trailer.

$$\delta = \frac{0.16x}{Re_x^{\frac{1}{7}}} \quad (4.1)$$

For turbulent BL on a flat plate, Prandtl's $(1/7)^{th}$ Power law expressions is generally recommended [24]. Equation 4.1 predicted the boundary layer height of $\approx 228mm$ for Reynolds number of 27.5 million based on truck length. Laying Prism layers for that height resulted in more than 70 million cells. Thus a trade-off is made between BL accuracy and computational time. This trade-off resulted in prism layers upto 60 mm and there onwards the polyhedral cells are laid and their size (height) is controlled using appropriate growth rate. In order to prove that this trade-off did not impact the solution a lot, u - velocity in the wall normal direction is plotted in 4.2a. Figure 4.2a shows the extent of full BL at the end of trailer ($\delta_{trailerend} = 1$) is 1 m. This is also the height until which the growth rate control is acting (figure 4.2b). Above this growth rate control cell size is rapidly increasing with distance from the wall (4.2b). It can also be noticed that Prandtl's analytical solution predicts the boundary layer height 5 times lesser than what CFD predicts.



Figure 4.1: y^+ contour over truck

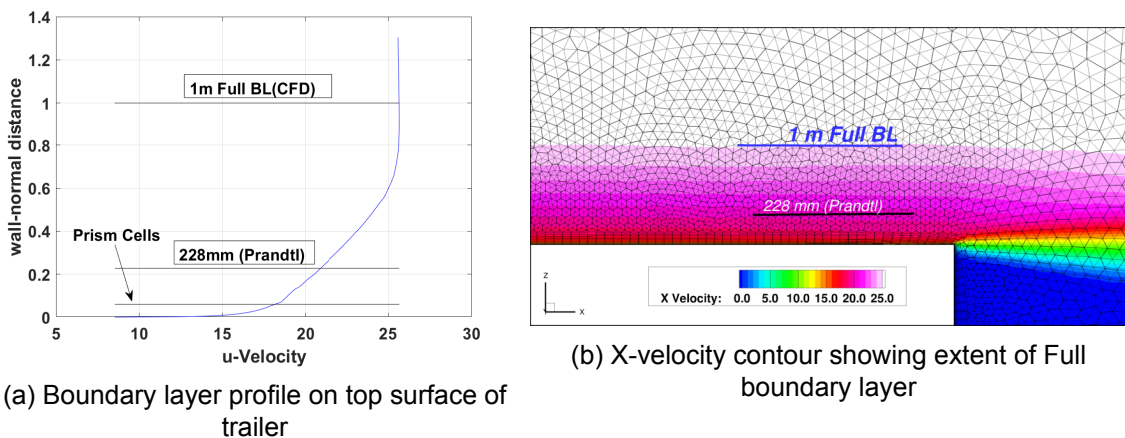


Figure 4.2: Boundary layer at the end of trailer, ($X/D = 10$, measured from trailer leading edge)

In the volume mesh process, certain refinement boxes are defined around the truck in order to capture flow features accurately. Although most of the wheelhouse flow features are mesh

Table 4.1: Refinement Box Sizing in different grids

Box Color	Finest (mm)	Fine (mm)	Medium (mm)	Coarse (mm)
Green	40	50	50	180
Purple	50	50	N/A	150
Red	40	50	50	150
Magenta	40	60	70	350
Cyan	130	130	130	350
Number of Cells (millions)	49	45	38	22

independent [17] this is necessary to achieve drag convergence. This is of utmost importance as total and component drag is what that sets apart different configurations. The refinement boxes used are depicted in the figures 4.3a and 4.3b and they are further discussed in the next section on Mesh Sensitivity Analysis.

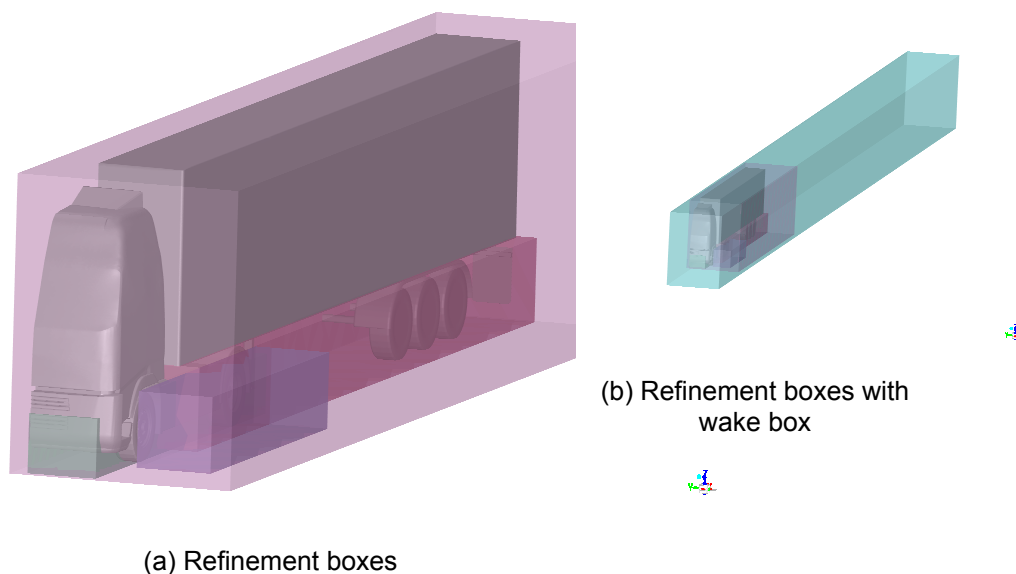


Figure 4.3: Refinement Regions

4.2. Mesh Sensitivity Analysis

The boxes are employed in such a way that they encompass underbody of the drag completely and wheelhouse flow features leaving the wheel. This meant extending the refinement boxes at least a meter away from the truck to capture the separated regions. Furthermore, four representative grids are used for mesh sensitivity analysis as mentioned in table 4.1. The study was based on the guidelines stated by Celik et al. [3] which will be discussed in detail in next section.

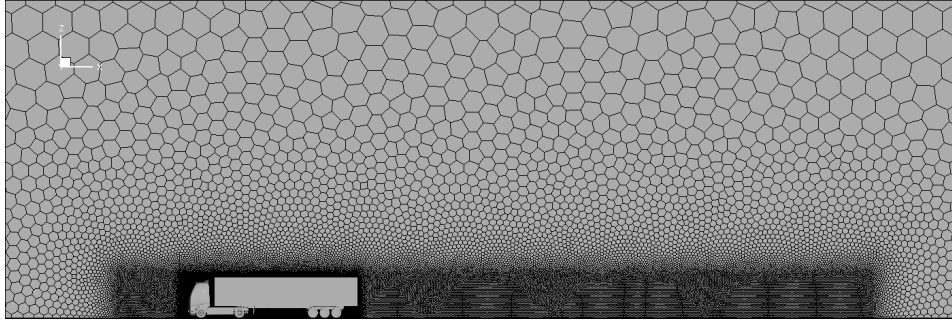
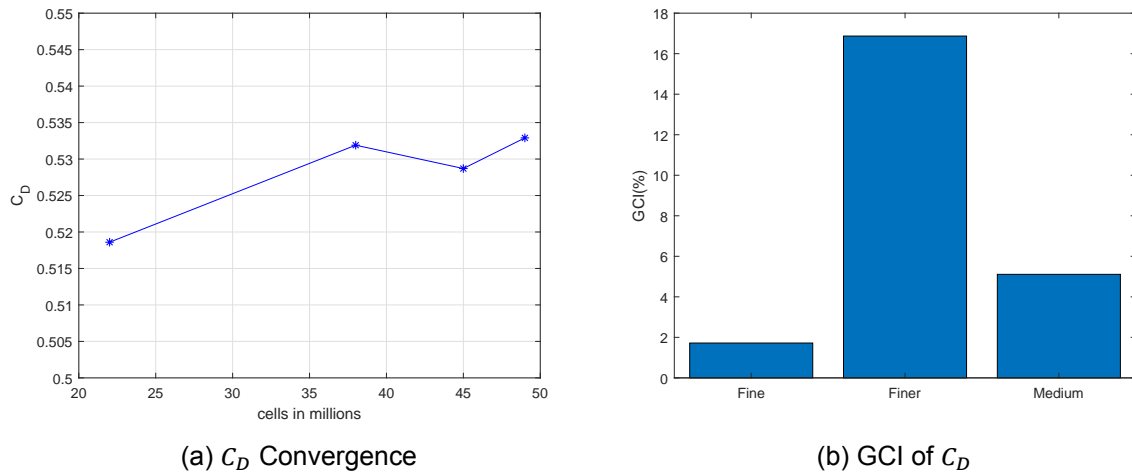


Figure 4.4: Overview of Mesh



As part of this study drag coefficient of the entire truck is monitored for all grids obtained from Unsteady RANS simulations. The unsteady simulations were run for around 20,000 timesteps until the drag coefficient converged to value with high frequency oscillations. The four representative grids had 22(*coarse*), 38(*medium*), 45(*Fine*) and 49(*Finest*) million cells respectively. Figure 4.5a shows the convergence of drag with respect to number of cells. An oscillatory convergence is observed in this flow problem. As the Finest mesh had 49 million cells it was impossible to get finer mesh owing to limitations of TU Delft hpc12 Cluster capabilities. Due to oscillatory convergence it was difficult to decide on representative grid based on figure 4.5a so Grid Convergence Index of drag coefficient is looked into in figure 4.5b.

4.2.1. GCI study

According to Celik et al. [3] the convergence and discretisation error are represented by a parameter called *Grid Convergence Index (GCI)*. GCI is proportional to relative error between grids. It is defined in equation 4.2. For more information about the parameters in equation 4.2 see Appendix C. The study stipulates that the the refinement ratio of finer and coarse grids must be ≥ 1.3 . This is one of the driving factors in refining the mesh and is indicated in the table C.1 in Appendix C.

$$GCI(\%) = \frac{1.25e_a^{ij}}{r_{ij} - 1} \quad (4.2)$$

where,

- e_a^{ij} - relative error between grids i and j .
- r_{ij} - refinement ratio between grids i and j .

So, according to GCI study (figure 4.5b) the fine grid (45 million cells) has the least discretisation error ($GCI = 1.72\%$) and least approximate relative error (0.61%). Hence, *Fine* grid was chosen as the representative grid for further simulations.

5

Results

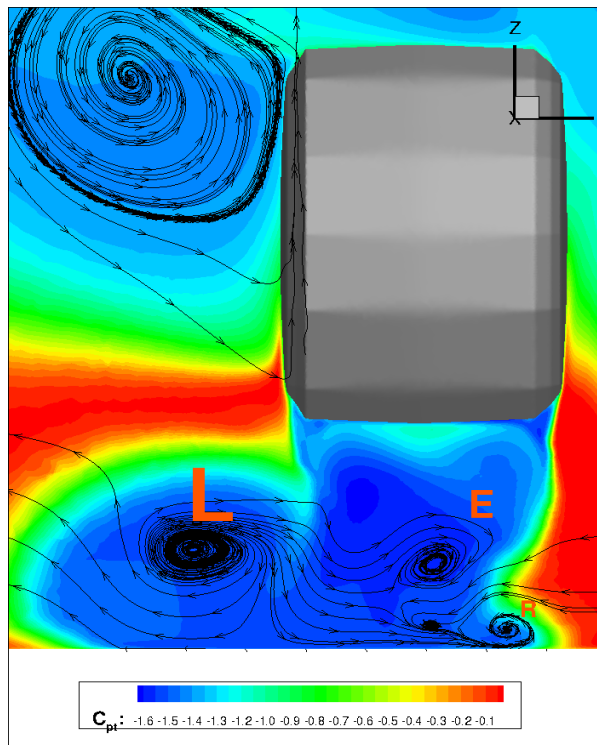
In this chapter, the results obtained are compared with literature. Initially flow features are compared and then some spectral analysis validation is done. After the validation, the side-skirt behaviour is explained. Furthermore, the no-side-skirt cases are first discussed and then the side-skirted cases. Amidst these results the mass flow rate analysis crucial to this thesis is presented. Lastly, the steady state simulations conducted on some modifications is also presented. At the end of the chapter, all the flow dynamics is also summarised.

5.1. Validation

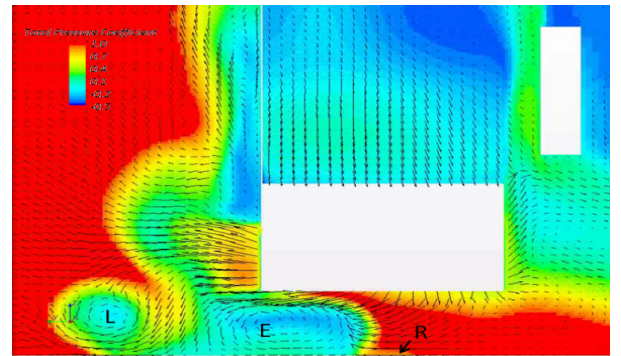
The flow features are confirmed by comparing single axle case (4X2) with the results of literature. Specifically, the results are compared with Regert and Lajos [15] and Scheeve [17] for vortices coming off the front wheelhouse while results of Stephens and Babinsky [20] are used for flow topology around the side-skirt.

The first validation starts with vortices coming off the front wheel. Vortices L, E and R are found in the lower wake of the front wheel (figure 5.1a). Furthermore, L and R vortices originating from the two ends of wheel patch are counter-rotating while E rotates opposite to vortex L. All three rotation direction conform with the results of Regert and Lajos [15] (figure 5.1c).

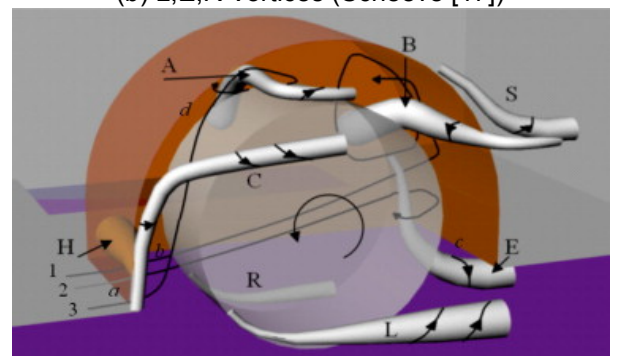
Looking at the upper wake of front wheel certain differences are found. These can be attributed to geometry since the model used by Regert and Lajos [15] was very simple. Firstly, Vortex C (figure 5.1c compare with figure 5.2a) as observed by Regert and Lajos [15] is a bit different. The observation made over different time shots suggests that it changes position with time by moving (origin) from the leading edge of wheelhouse to front portion of truck. Thus, here it is referred as **FB** owing to its origin, the Foot Board (figure 5.2a). Furthermore, in the same figure, a new vortex originating from the front curve is recognized and is named as **FMG** owing to its close proximity to Front Mud Guard (figure5.2a). Vortex FMG is not a native wheelhouse vortex and is not recognised in any literature. Lastly, Vortex B (figure 5.2b) is found at exact angular position with respect to wheel but its behaviour out of the wheelhouse is quite erratic. Instead of being washed away from free stream flow like in figure 5.1c, it moves in a direction opposite to freestream flow before being washed away by freestream flow.



(a) L,E,R Vortices, perpendicular to streamwise direction looking from the back of the front wheel, $X/D = 0.2$, wheel center being the origin

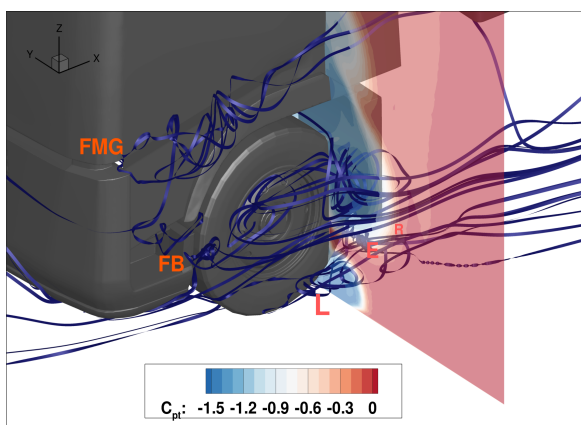


(b) L,E,R Vortices (Scheeve [17])

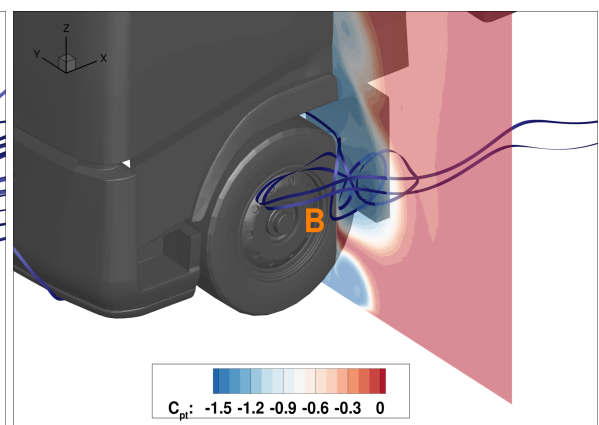


(c) Vortex structure by Regert and Lajos [15]

Figure 5.1: L,E,R Vortices Validation



(a) FMG,FB vortices



(b) Vortex B

Figure 5.2: Vortex Profile, $X/D = 0.2$

Now, the validation is done downstream of the front wheel especially below the trailer. This is also the position where side-skirt is positioned in side-skirted cases. Stephens and Babinsky [20] concluded that side-skirt prevents high momentum fluid (from freestream) from being mixed with low momentum fluid (in the underbody) at the top and prevents viceversa at the bottom. This is confirmed by tracking stream traces in the Z-plane (figure 5.3). In figure 5.3, it is clear that flow tends to move out of underbody at/near the ground plane while it is opposite as we move away from ground plane. This can be attributed to pressure depression which will be explained in the following sections. In figure 5.3, the size of the wake behind the rear wheel grows as we move away from the ground plane (blue region becomes bigger). This already hints at the fact that there exists a low pressure region behind the rear wheels. The low pressure region grows bigger as move away from the ground. This is possibly the reason for the flow to enter trailer underbody as we move away from the ground plane. Nevertheless, at the ground plane the flow leaves the underbody (close to trailer wheel), this is due to the stagnation point formed at the first trailer wheel and also due to the blockage offered by the trailer wheel axles.

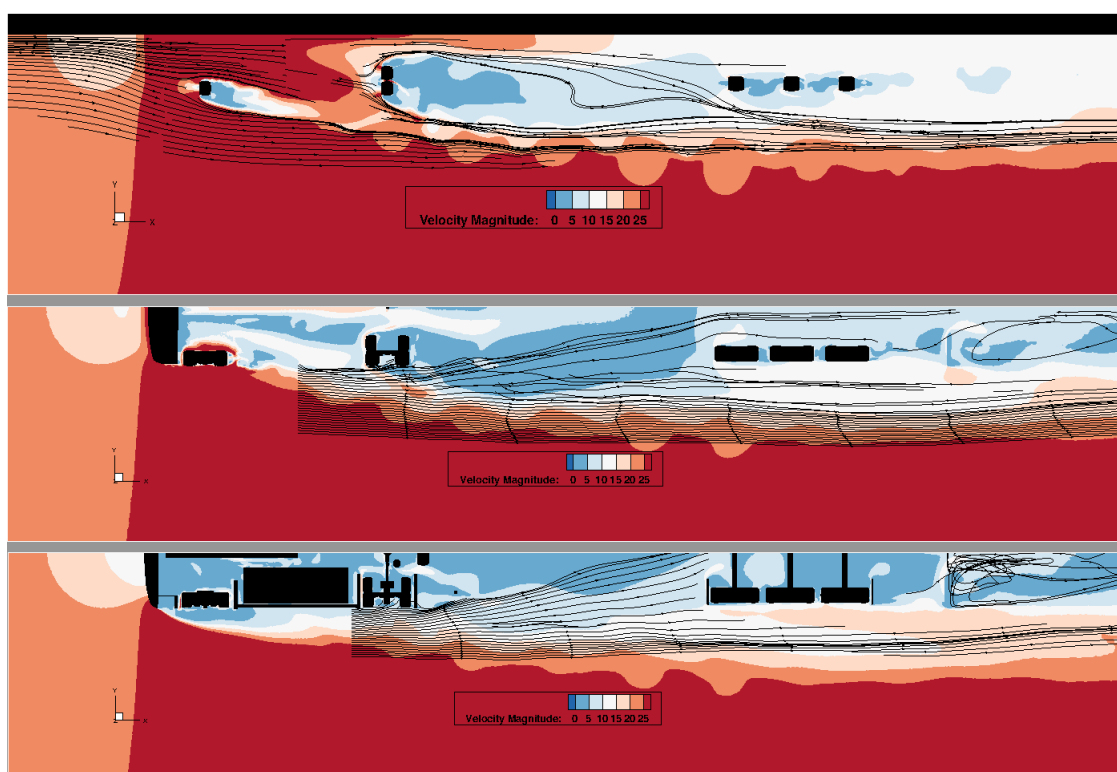


Figure 5.3: Downstream validation with Stephens and Babinsky [20] on **no-side-skirt case**. $Z/D=0.01$ (top), $Z/D=0.2$ (middle), $Z/D=0.5$ (bottom)

5.1.1. Spectral Validation

In this section, the standard deviation spectrum of drag coefficient is evaluated with results of Elofsson et al. [6]. Elofsson et al. [6] conducted simulations on a realistic Scania truck model and a simplistic model (similar to the one used in thesis). They ran their simulations for about 60s in both yaw and no-yaw condition. They suggest that one complete cycle of oscillations on a truck spans around 4s. This translates to lowest dominant frequency of 0.25Hz . Figures 5.4a and 5.4b show the comparison between simulations conducted by them and the simulation (4X2) in this thesis. It can be noticed that in no-yaw condition, there is a shift in dominant

frequency from 0.1Hz to 0.25Hz (current thesis) while the levels of standard deviation are very close. One more observation in figure 5.4b that can be made here is that the current thesis spectrum is very close to yawed case spectrum of Elofsson et al. [6] with dominant frequency at 0.25Hz . Nevertheless, though there is a discrepancy in the lowest dominant frequency, it can be concluded that the longest flow feature has a timescale in the range $4 - 10\text{s}$.

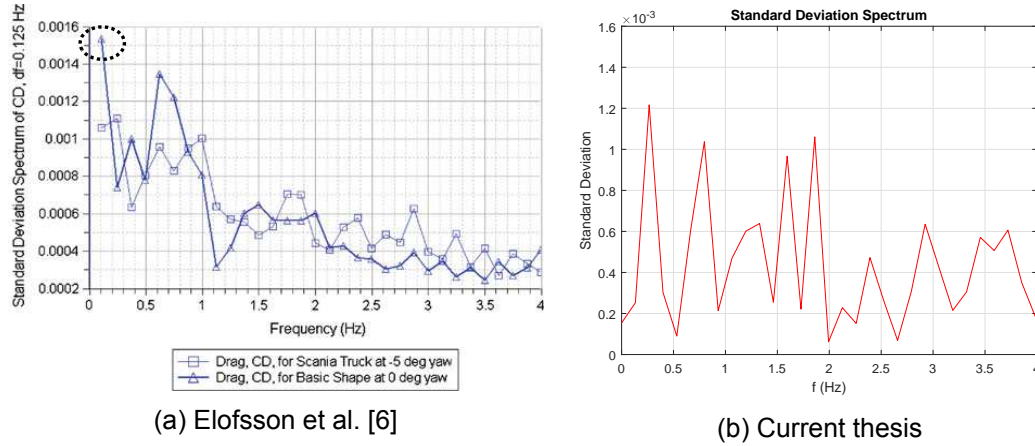


Figure 5.4: Standard Deviation Spectrum

5.1.2. Downstream Behaviour

This section throws some light on downstream behaviour of the front-wheelhouse vortices and other vortices originating from front and cabin of the truck. Firstly, Vortices L, E and R merge downstream (figure 5.5). This happens because there is a strong yawed flow (bleed flow) emerging from the underbody washing away all vortices in the lower-wake of the front wheel. In the absence of the bleed flow, they would still merge but further downstream. The strong yawed flow or side flow emanating from underbody is due to blockage experienced by flow due to underbody components like shaft assembly, rear wheels.

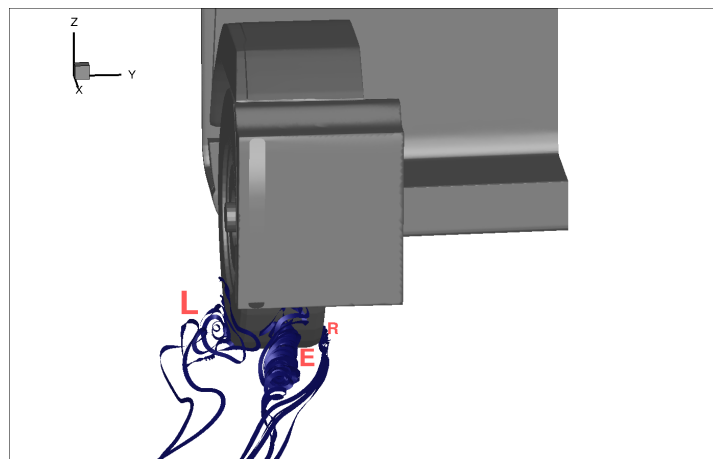


Figure 5.5: L,E,R vortices (Only E & R merging is shown in this image, L merges further downstream)

Furthermore, as we are interested in downstream behaviour of vortices identified in figure 5.2a, a different approach is devised in figure 5.6 to understand them. Figure 5.6 shows the iso surfaces of total pressure coefficient coloured by x-vorticity. The individual vortices identified in figure 5.2a can now be seen as blobs of large separated region. Especially, the FB vortex,

though it originates as a vortex at the foot board immediately breaks apart into smaller vortices (small red regions of similar vorticity). Nevertheless, these smaller vortices eventually join the other vortices originating from wheelhouse to form a large separated region as shown in figure 5.6. The large blob originating from FB vortex, is the one influenced by rear wheel low pressure regions and the low pressure region in the wake of the rear wheel. This will be explained in the following sections with streamlines.

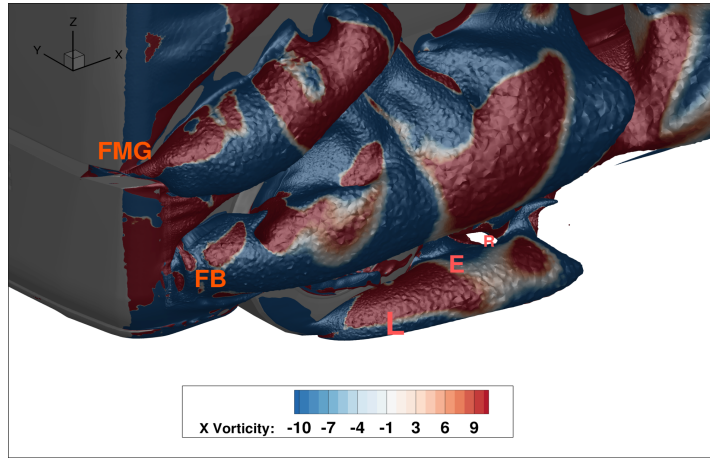


Figure 5.6: All vortices coalesced as large blobs of separated region. The original positions of vortices observed in figure 5.2a is also highlighted, Isosurfaces of $C_{P_t} = -1.2$ coloured by X-vorticity

5.2. Side-skirt Behaviour

The behaviour of side-skirt must be understood in single axle configuration before doing any analysis on dual axle configuration. Stephens and Babinsky [20] have clearly stated that side-skirt prevents flow mixing along the sides of trailer near the underbody. Thereby restricting any momentum losses which eventually increases drag. This behaviour is confirmed in figure 5.7, side-skirt separates the region of low (*underbody*) and high (*side of truck*) momentum. Side-skirt in this case is performing the function of an air-dam separating these two regions of varied velocity. At this point, a parameter is defined to understand the performance of side-skirt (η_{SS}). It is defined as the ratio between mass flow into the underbody in side-skirt case to mass flow into the underbody no-side-skirt case (equation 5.1).

$$\eta_{SS} = \frac{(\dot{m}_{UB})_{SS}}{(\dot{m}_{UB})_{no-SS}} \quad (5.1)$$

Furthermore, validation of the side-skirt's performance with literature must be done. van Raemdonck [22] tested side-skirt in a wind tunnel and predicted a drag reduction of 14% in no yaw condition while only 5.86% was predicted in this thesis for single axle case. van Raemdonck [22]'s tests were conducted with stationary elevated ground plane. This discrepancy comes from the windtunnel setup used by van Raemdonck (figure 5.9). Firstly, the absence of moving ground makes a huge difference in this case. The performance of the side-skirt is dictated by the flow dynamics close to the ground. A stationary ground implies more momentum losses and the entire side-skirt might be submerged in a thicker boundary layer than in reality. Secondly, the RANS approach used in this thesis models the turbulence. These two factors might be the cause of the discrepancy.

Furthermore, as the side-skirt does not extend all the way to the ground, the flow escaping beneath it is examined to gain deeper insights. In Figure 5.10, Y-momentum is plotted on a

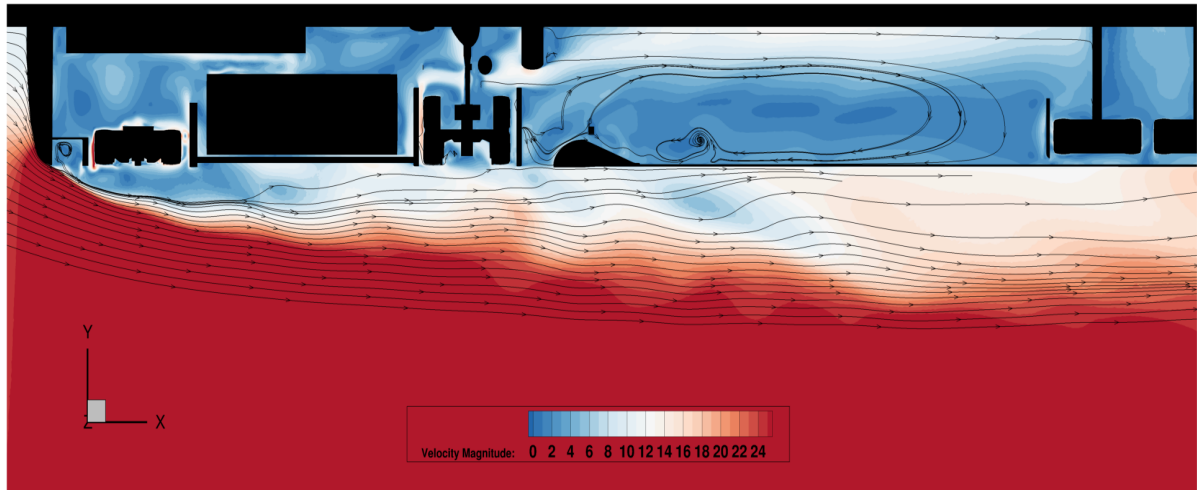


Figure 5.7: Side-skirt restricting flow, $Z/D=0.52$

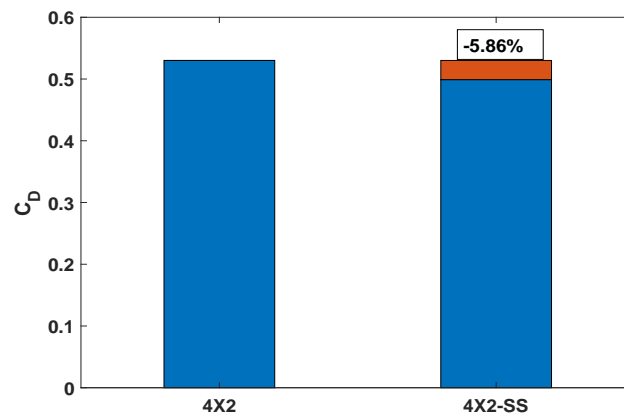
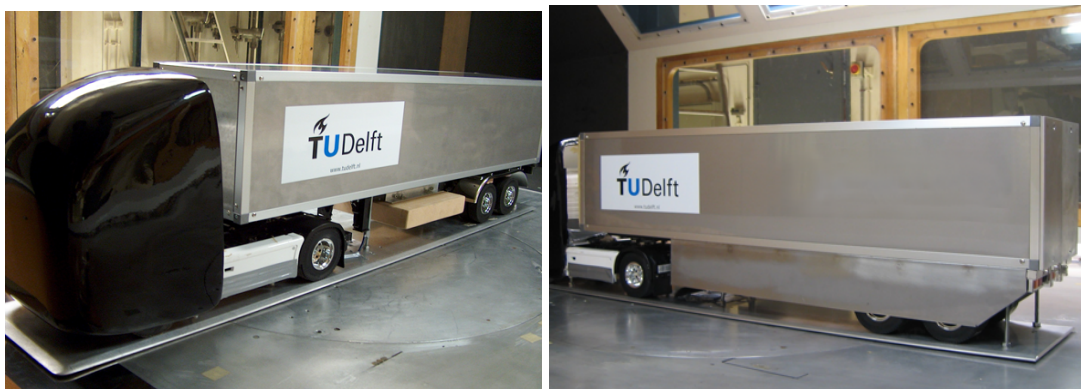


Figure 5.8: Side-skirt performance in 4X2 (single axle condition)



(a) Isometric View (no side-skirt)

(b) Isometric view rear (side-skirt)

Figure 5.9: Windtunnel setup of van Raemdonck

y-plane close to the truck surface. A positive y-momentum represents inflow (*red*) into the underbody while a negative y-momentum represents outflow (*blue*) from the underbody. It can be noticed that there is an outflow from $X/D = 0$ to $X/D = 7$. These positions correspond to tractor front wheel up until mid-side-skirt. From $X/D = 7$ to $X/D = 11$ there is an acute inflow (opposite to no-side-skirt case (figure 5.3)). These positions correspond to mid-side-skirt to first trailer wheel. Thus, it can be concluded that the side-skirt although is restricting flow mixing at the top, it is ineffective at the bottom, close to the ground. Nevertheless, the fact that CFD is showing the right trends is already quite promising.

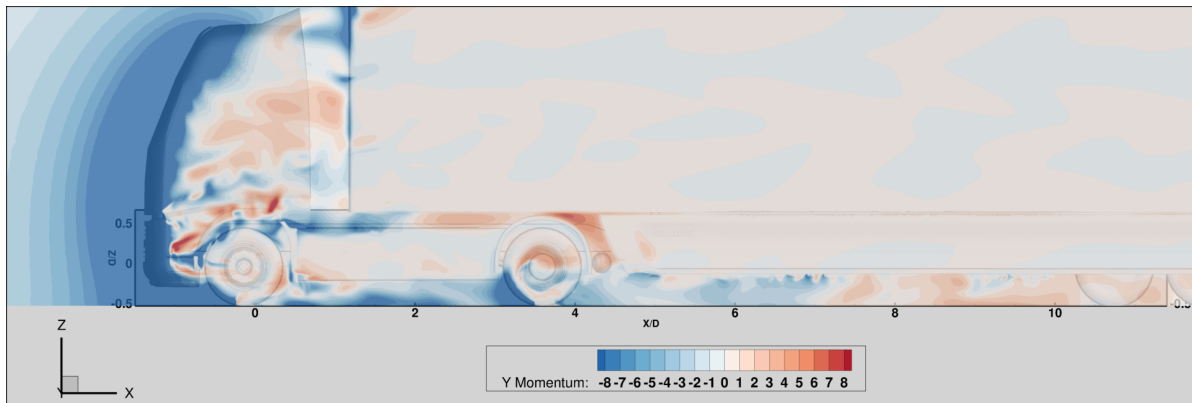


Figure 5.10: Y-momentum analysis, **outflow** (*blue*), **inflow** (*red*), slice $Y/D = -0.01$

5.3. Averaging Window Analysis

As indicated in section 3.8, the implications of averaging window will be shown in this section. In figure 5.11a the average drag coefficient is plotted against averaging window size (in seconds). Although the average varies with window size, the variation is in the order of 0.0001 drag count ($C_D = 0.00001$) which is very insignificant to our analysis. In figure 5.11b, the standard deviation observed while averaging over each window size is plotted. The standard deviation varies from 0.0052 to 0.0054 with different window sizes. This confirms that averaging window does have some influence over the drag coefficient but it can be ignored. To be more accurate the averaging window was chosen as 4s.

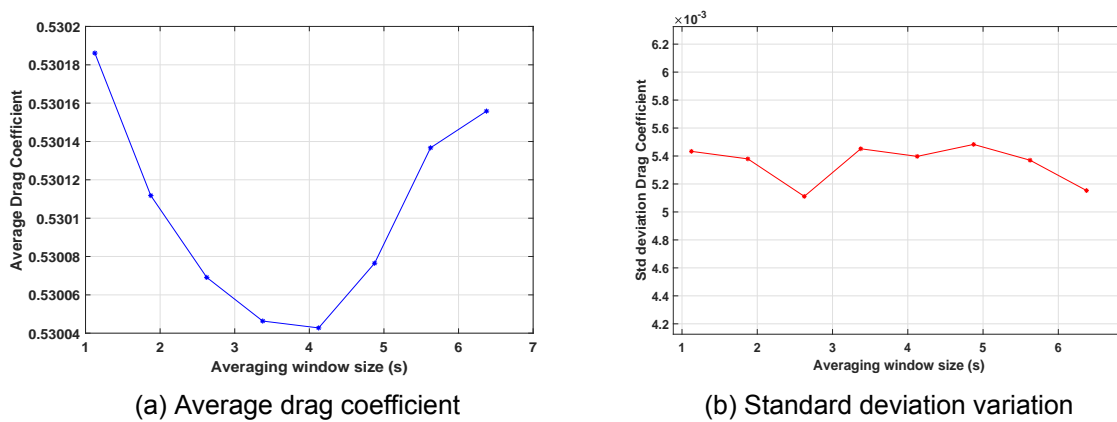


Figure 5.11: Averaging window analysis

5.4. Underperformance Quantification

Simulations were conducted on the four principal configurations. The drag difference between the side-skirt fitted case and baseline case (no side-skirt) is compared in this section (table 5.1). In 6X4 case the side-skirt is underperforming by little margin in terms of drag. Furthermore, as the function of side-skirt is to restrict mass flow in and out of underbody, the mass flow rate monitors are investigated.

Table 5.1: Massflow rates and side-skirt efficiency and drag coefficients

Configuration	$\dot{m}_{UB}(Kg/s)$	η_{SS}	C_D	ΔC_D
4X2	4.506	-	0.5301	-
4X2 – SS	0.5303	0.8823	0.4990	-0.0311 (-5.86%)
6X4	8.07	-	0.5266	-
6X4 – SS	4.51	0.4411	0.5023	-0.0243 (-4.61%)

Table 5.1 suggests that in single axle case side-skirt is able to restrict 88% of mass flowing into the underbody compared to no-side-skirt case while in dual axle case it drops to 44%. This steep drop in ability to restrict mass entering/leaving the underbody of trailer is the main cause of reduced fuel savings as seen in dual axle cases.

5.4.1. Fuel Savings

Understanding the above mentioned scenario in terms of fuel savings gives a better perspective about the savings/losses occurring in this case. Also, it allows an easy comparison with WABCO-OptiFlow's track test data. In this section, the drag reductions as predicted by CFD simulations is converted into fuel savings using an empirical formula (equation 5.2) (derivation Appendix D).

$$\frac{\Delta FC}{FC} = \eta_{engine} \frac{\Delta C_D}{C_D} \quad (5.2)$$

where,

- FC- Fuel consumption
- η_{engine} - Thermal efficiency of the engine

The thermal efficiency of the diesel engines used in HDV was studied by Delgado and Lutsey [5] (figure 5.12). An engine efficiency of 45% can be used from this distribution.

Table 5.2: Fuel Savings (normalized)

Configuration	CFD(%)	Track test data (%)
4X2-SS	1	1
6X4-SS	0.79	0.49

In table 5.2 a similar trend can be seen both in track test results (obtained from WABCO-OptiFlow) and CFD results. In 6X4 condition the fuel saving drops. Although the drastic drop in fuel savings is only seen in track test, CFD still predicts a smaller drop in fuel savings. This inaccuracy can be attributed to capabilities of RANS turbulence model. Also, the track tests were conducted on a highly detailed real life model in realistic wind conditions whereas the CFD model is simplified and tested only on no-yaw condition. The drop in fuel efficiency with respect to single axle case in CFD is around 21% while track test shows a drop of 51%.

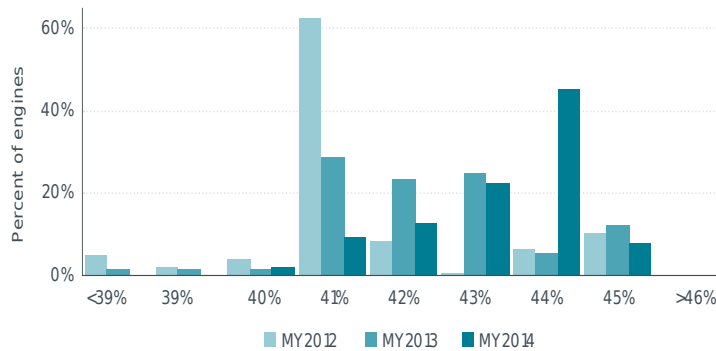


Figure 5.12: Brake thermal efficiency distribution of engines based on certified model year [5]

5.5. Cause of underperformance

The underperformance was quantified in last section. In this section, the drop in drag reduction in dual axle case will be related to flow features and other flow parameters. In order to investigate the source of the problem, a simple approach is designed. Since, the performance of side-skirt is entirely dependent on its ability to restrict mass entering the underbody, monitoring mass flow rates at different planes along the sides of the truck seemed a reasonable approach. The mass flow is monitored across the planes as shown in the figure 5.14 . The corresponding mass flow rates are represented in table 5.3. The negative mass flow rates in the table are leaving the underbody and the positive ones are entering the underbody.

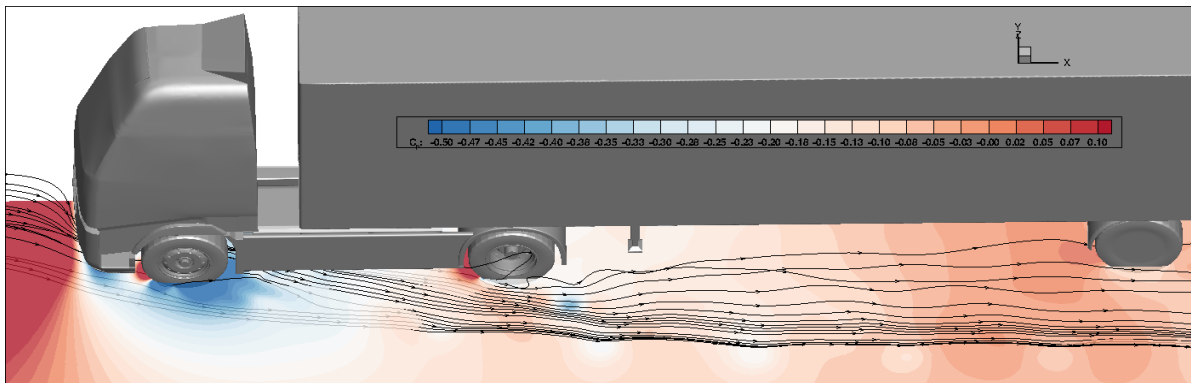


Figure 5.13: Underbody bleed

Table 5.3: Massflow rates (kg/s)

Position	FW	FUEL TANK	RW1	GAP	RW2	RW_SS_GAP	SS
4X2	-2,77	-2,26	-1,31	-0,32	-1,294	0,20	4,50
6X4	-3,10	-3,15	-2,83	-0,44	-1,47	0,22	8,07
4X2_SS	-2,08	-2,72	-1,29	-0,31	-1,19	-0,06	0,53
6X4_SS	-2,65	-3,31	-2,72	-0,41	-1,14	0,19	4,51

It is evident from table 5.3 that the addition of a tractor axle bleeds more air towards the sides. In figure 5.13 it can be seen that the flow escapes onto the sides, starting beneath the fuel tank and even figure 5.10 represents the bleed flow through negative y-momentum

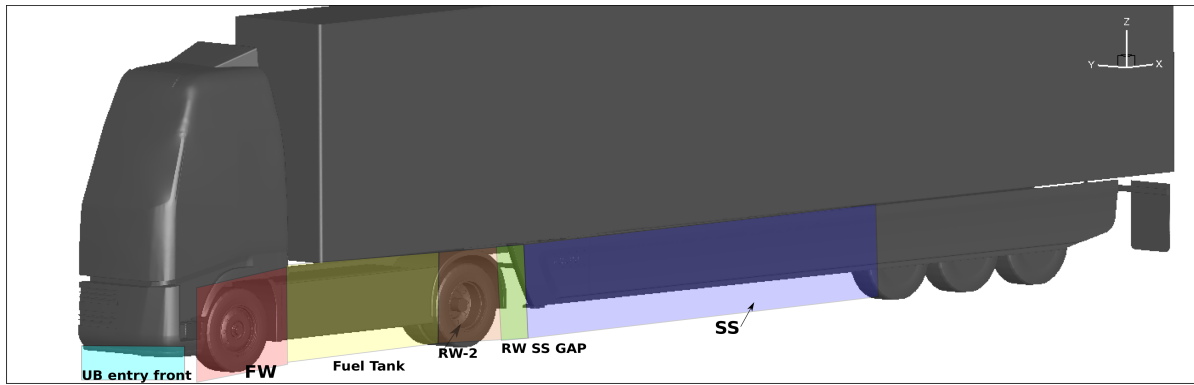


Figure 5.14: Massflow rate plane positions

regions. This is because of the blockage introduced by shaft and other underbody components. Even in the single axle case(4X2) a significant amount of air is bled onto the sides from the underbody. Table 5.4 represents the mass flow rates at the UB entry front (below front mudguard), side bleed (flow escaping onto the sides from the tractor), UB in (flow entering the trailer underbody). The *UB in* mass flow rate is considered only until the leading edge of first trailer wheel not until the entire length of the trailer. In the single axle cases about 70% of the flow entering is bled through the sides whereas in dual axle cases the behaviour is different. As there is more blockage introduced by the additional wheel and its shaft components, more flow is bled through the sides in 6X4 case. Furthermore, there is an acute increase in inflow into the trailer underbody in 6X4 case, almost double than that of single axle case 4X2. These statistical data suggest that the additional inflow into the trailer underbody might be because of the additional bleed introduced because of the additional wheel/axle. In other words, the increased bleed rate is the one entering the trailer underbody.

Table 5.4: Bleed rates (kg/s)

Position	UB entry front	Side Bleed	UB in (below trailer)
4X2	10,679	-7,96	4,7
6X4	10,439	-11,02	8,29
4X2_SS	10,598	-7,6	0,46
6X4_SS	10,49	-10,24	4,7

There is an influx of mass into the trailer underbody in no-side-skirt cases. The majority of mass influx is originating at Foot Board (figure 5.15a). In other words, majority of streamlines entering the trailer underbody are from foot board. The streamlines in figure 5.15a curl around the rear wheel due to the low pressure region present behind the rear wheel, in its wake. Furthermore, a low pressure region not only exists behind the rear wheel but starts inside the wheel-well (figure 5.15b). The low momentum fluid inside the wheel-well is ejected out into the side flow (figure 5.16) further adding to momentum losses in the side flow. Wheel-well low pressure region is also equally drawing the bleed-flow beneath the fuel tank towards the trailer underbody along with the low pressure region in the wake of wheel. Interestingly, only some of the streamlines originating from bleed-flow beneath the fuel tank are ingested into the trailer underbody while majority of *FB* vortex is ingested into the trailer underbody. The rest of the fuel tank bleed-flow eventually joins the freestream.

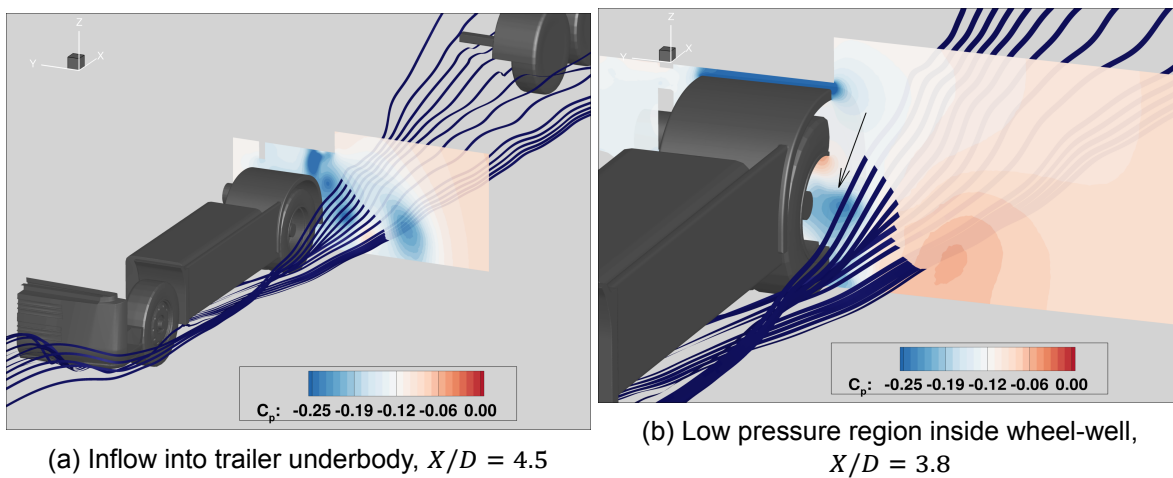


Figure 5.15: Inflow and low pressure regions

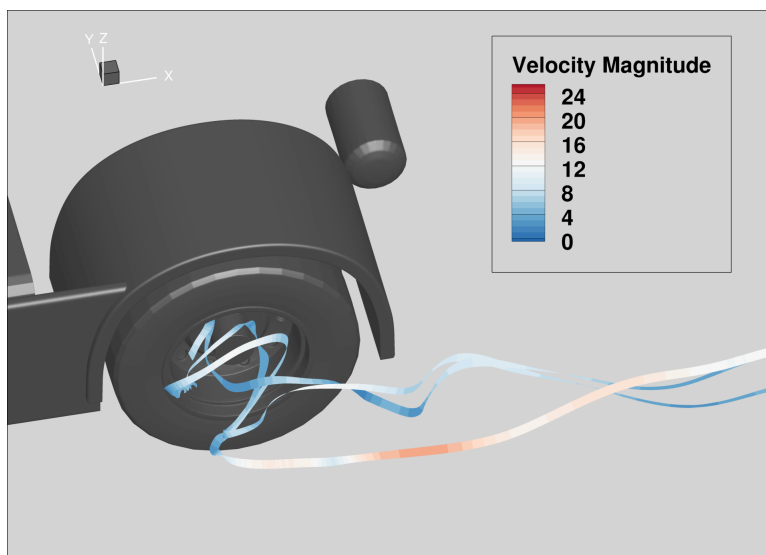


Figure 5.16: Low momentum fluid ejection from rear wheel-well. Streamlines emanating from Wheel-well and joining the freestream

5.5.1. No side-skirt cases

As mentioned in the previous section, a higher bleed rate is seen in dual axle case. The changes in flow features originating due to this higher bleed rate are discussed in this section in comparison with single axle case. The additional wheel increases suction behind the rear wheels (figure 5.17b) thereby increasing mass influx into the trailer underbody (table 5.4). To understand the extent of the low pressure suction region, isosurface of $C_p = -0.16$ is given in figure 5.18 for both cases. Furthermore, in figure 5.18 the isosurfaces are coloured by C_{P_t} to understand the energy content in the flow as total pressure is reminiscent of energy in incompressible flows. A close comparison of these iso-surfaces reveal that in 6X4 case there is a larger suction region behind the wheels and this region also has lower C_{P_t} value implying that there is larger region with momentum loss.

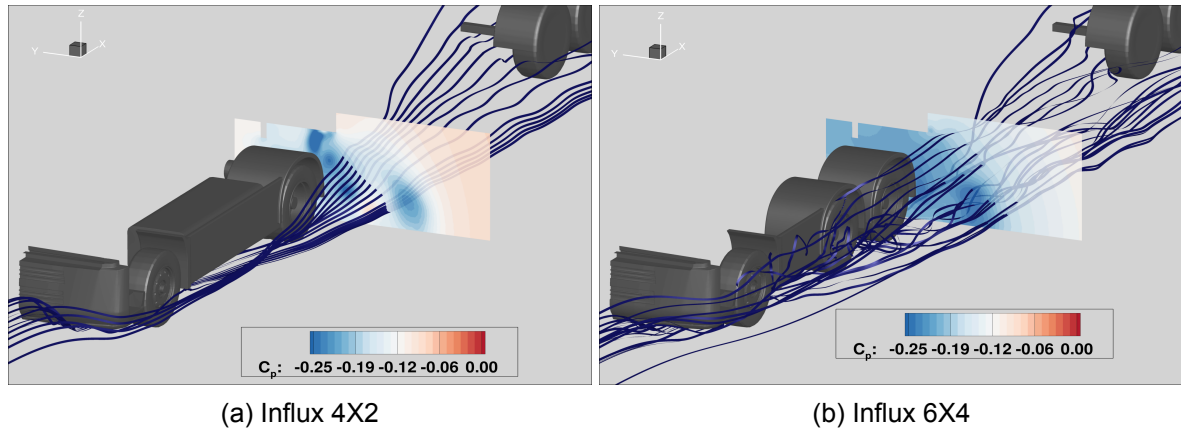


Figure 5.17: Influx at $X/D = 4.5$

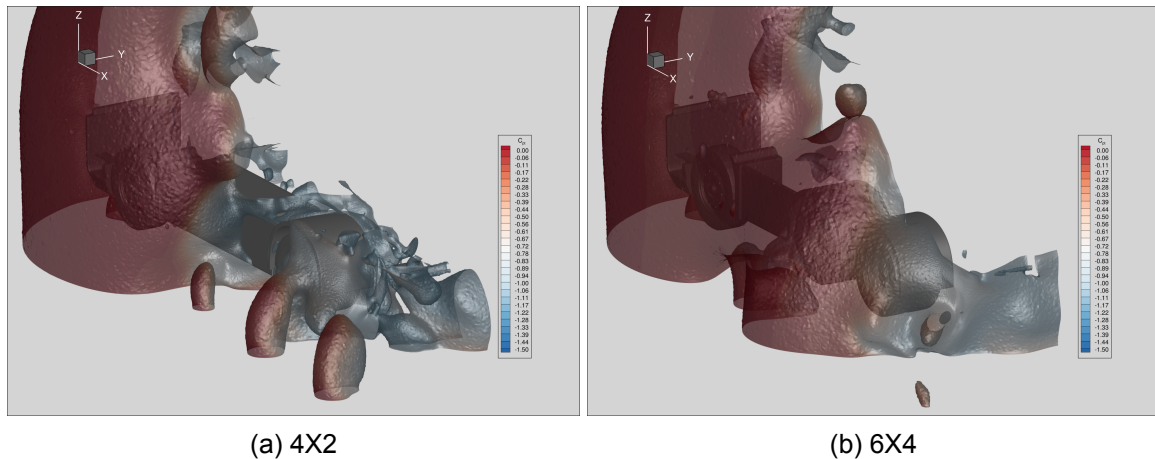


Figure 5.18: Suction region, isosurfaces of $C_p = -0.16$ colored by C_{P_t}

5.5.2. Side-skirt cases

In the side-skirt cases, the FB vortex is restricted from entering the trailer underbody whereas it still finds a way to enter by curling up around the lower edge of side-skirt. This effectively means that there is an acceleration of flow at the lower edge of side-skirt and hence suction region. This suction region along with the low pressure region created by additional axle draws more flow into the underbody in 6X4 case than 4X2 case (figure 5.19). The bleed-flow beneath the fuel tank remains similar to no side-skirt cases, here too they join free stream

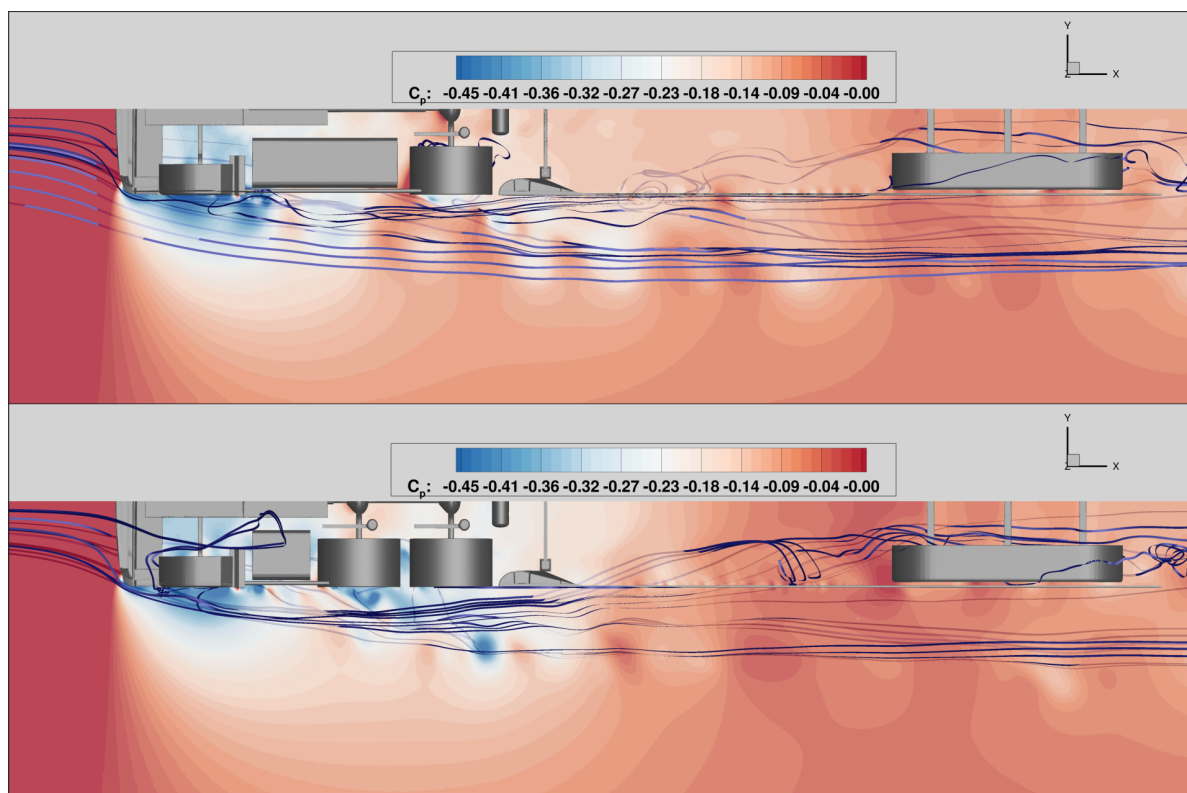


Figure 5.19: Influx difference in side-skirt cases, slice $Z/D = 0.3$

after separating from rear wheels. The most interesting observation that can be made here is the interaction between bleed flow, the wheel-well flow and the flow entering the underbody. In figure 5.20, the point of entry of the flow into the underbody is marked, right in front of the marker there exists a pressure ripple in both cases. This is a high pressure ripple emanating from separation point on the leading edge of the first rear wheel. The high pressure ripple acts as a trigger for the flow close to the side-skirt/truck surface in being pushed beneath the underbody where there already exists a low pressure region (due to wake of the rear wheels). In the absence of these high pressure ripples there may not be any flow entering the underbody or there will be lesser mass entering the underbody because in that case the pressure difference on both the sides of the side-skirt might be zero or less drastic resulting in lesser mass flow into the underbody (this is the behaviour seen in $4X2 - SS$ case too).

The increased suction behind $6X4$ rear wheels explains more influx into the underbody but it does not clearly tell us why the FB vortex-blob is pulled downwards towards the ground. This action is very important as this aids the streamlines to enter the underbody beneath the side-skirt. To understand this, streamlines emanating from the front portion (mainly FB vortex-blob and its free shear layer downstream) along with C_p are plotted in figure 5.21. In the first streamwise plane plotted in figure 5.21 there exists a low pressure region that is pulling the the streamlines above it towards the ground in $6X4 - SS$ case in comparison with $4X2 - SS$ case. This behaviour continues until those streamlines reach the entry point (into the underbody) in the $6X4 - SS$ case. It must be noticed that this behaviour is absent in $4X2$ side-skirt case where the streamlines take a more curved path moving upwards away from the ground. This acute low pressure region right off the first rear wheel-well in $6X4 - SS$ case is the combined effect of bleed flow exiting beneath the fuel tank, the low momentum fluid ejected from the first wheel-well and some low momentum fluid emanating from the gap between two rear wheels.

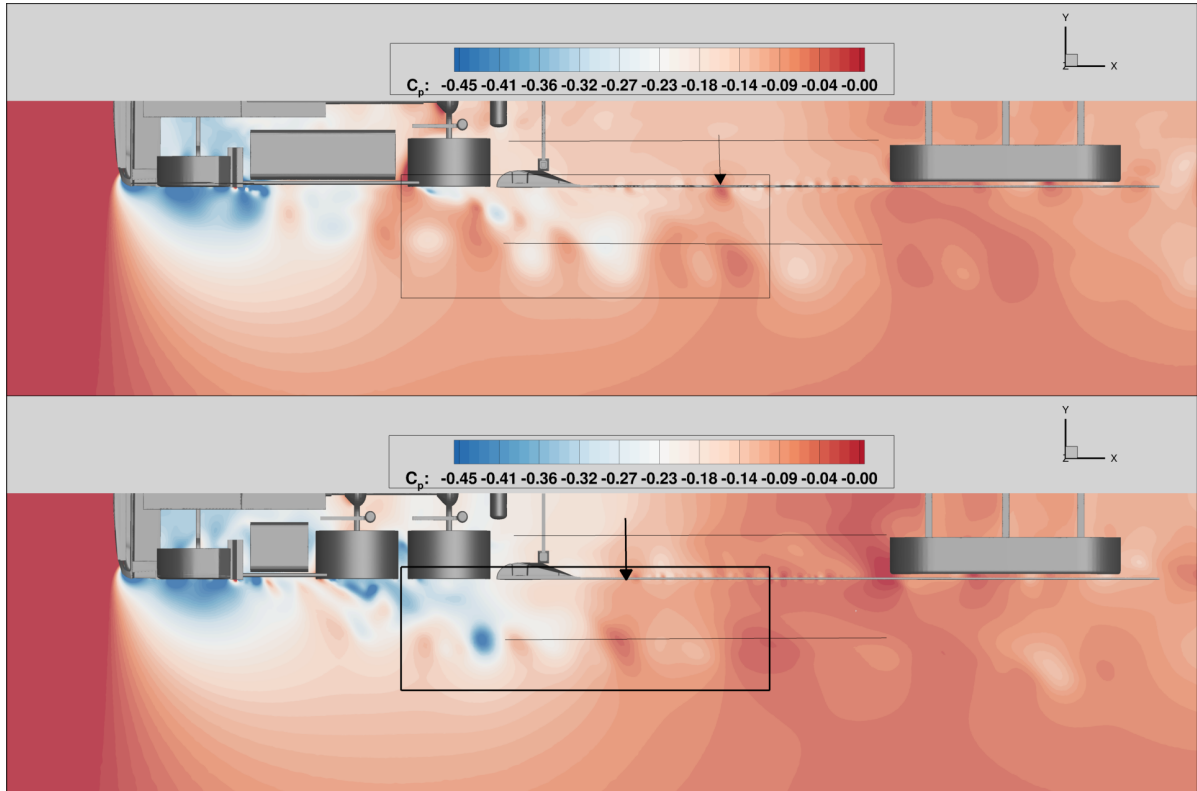


Figure 5.20: Ripples emerging from rear wheels, along with inflow entry marked, $Z/D = 0.3$

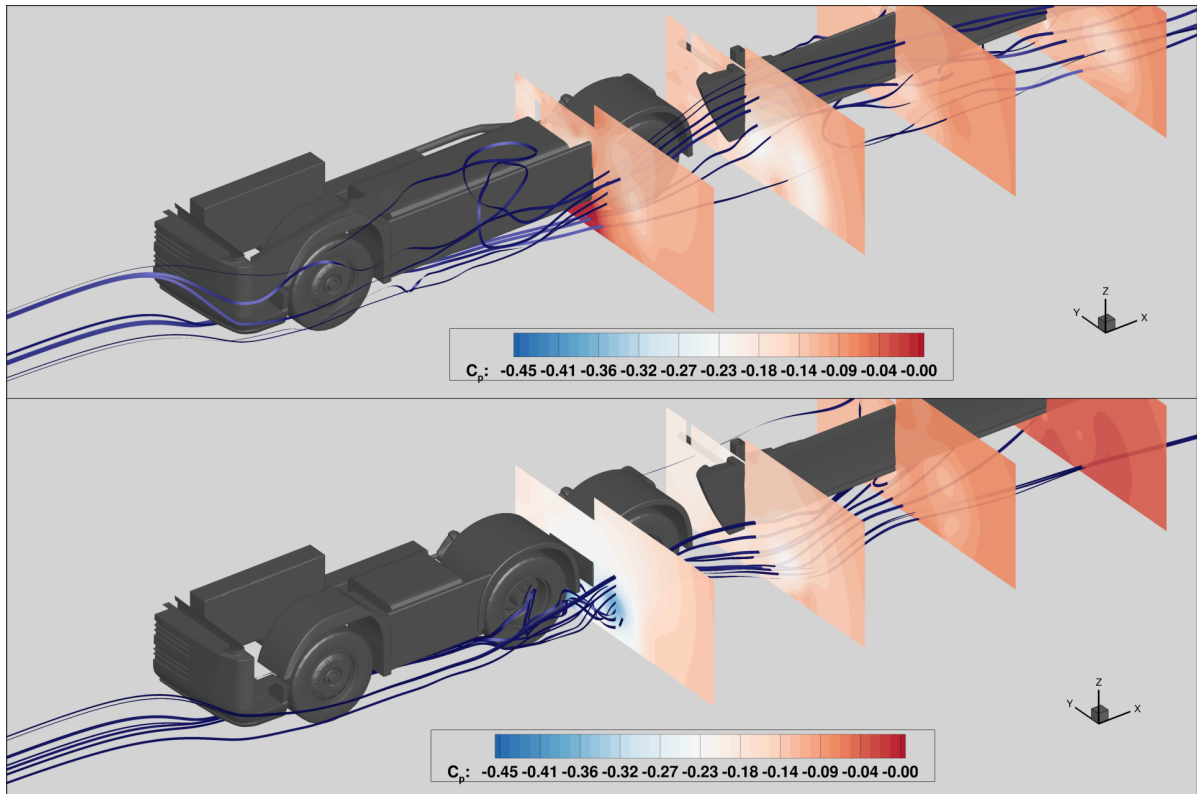


Figure 5.21: Bleed flow, wheel-well flow, inflow interaction

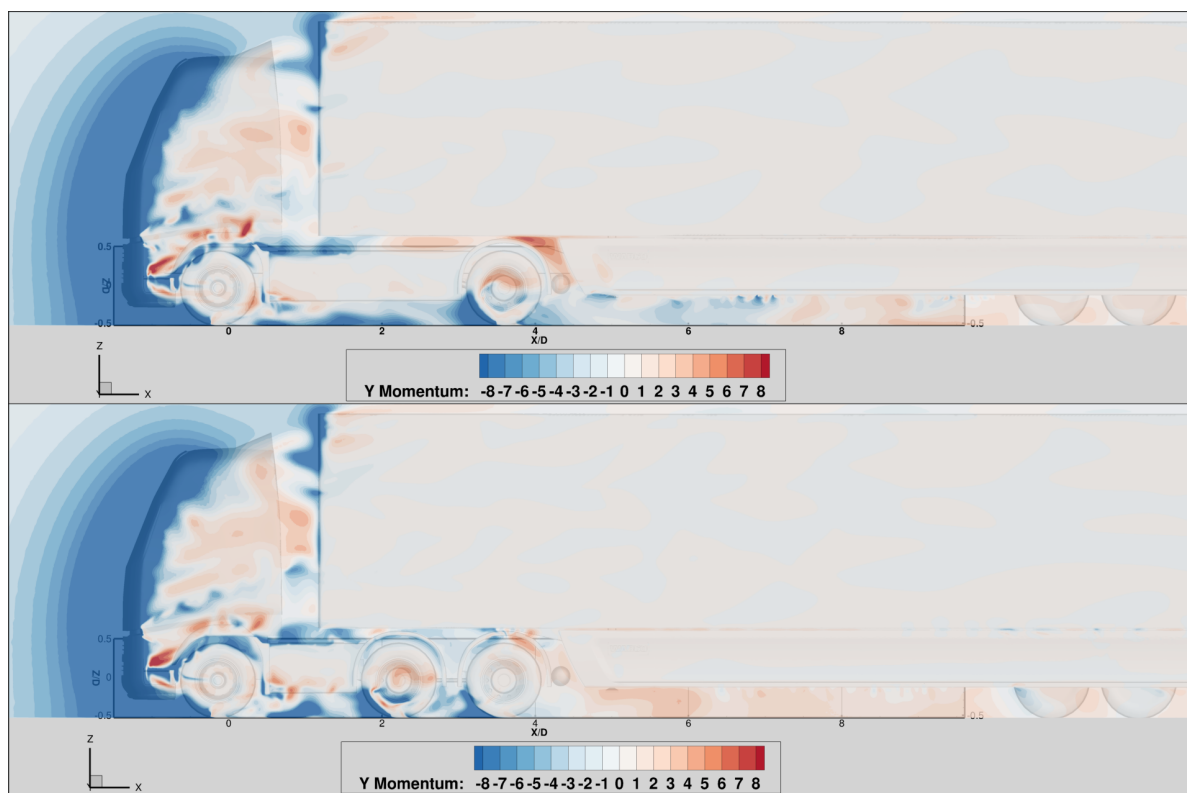


Figure 5.22: Y-momentem analysis, **outflow** (blue), **inflow** (red), slice $Y/D = -0.01$

To further substantiate mass flow rate analysis, Y-momentum analysis is done on both single and dual axle cases. Figure 5.22 shows that in $6X4 - SS$ case there is strong inflow beneath the side-skirt, for almost the entire length unlike $4X2 - SS$ case where inflow was seen only close to the first trailer wheel.

The trend seen in Y-momentum analysis can be explained by pressure difference plot in figure 5.23. It represents the pressure difference between the inside (trailer underbody) and outside (sides) with respect to the inside of the trailer. The pressure difference were taken along the line as shown in figure 5.20. In figure 5.23, the negative peaks correspond to *outflow* because the pressure on the outside is lower than the pressure on the inside while positive peaks refer to *inflow* as the pressure on the outside is higher than the pressure on the inside. In $4X2 - SS$ case, it can be noticed that from $X/D = 4.5$ to $X/D = 6$ there are negative peaks implying *outflow*. This results corresponds with Y-momentum analysis (figure 5.22). Further downstream positive peaks can be found which imply *inflow*, again going with the Y-momentum analysis. In $6X4 - SS$ case, there is negative peak at around $X/D = 5$ implying *outflow*. There is region right behind the last rear wheel. The positive peak at around $X/D = 6$ is also the entry point of the flow entering the underbody. The peaks downstream in both single and dual axle cases arise due to presence of first trailer wheel but these do not influence the flow too much. In other words one can expect an outflow in these regions but it is not seen probably because of *flow inertia*. This is so because the streamwise momentum might outweigh the pressure forces acting in a direction perpendicular to streamwise direction.

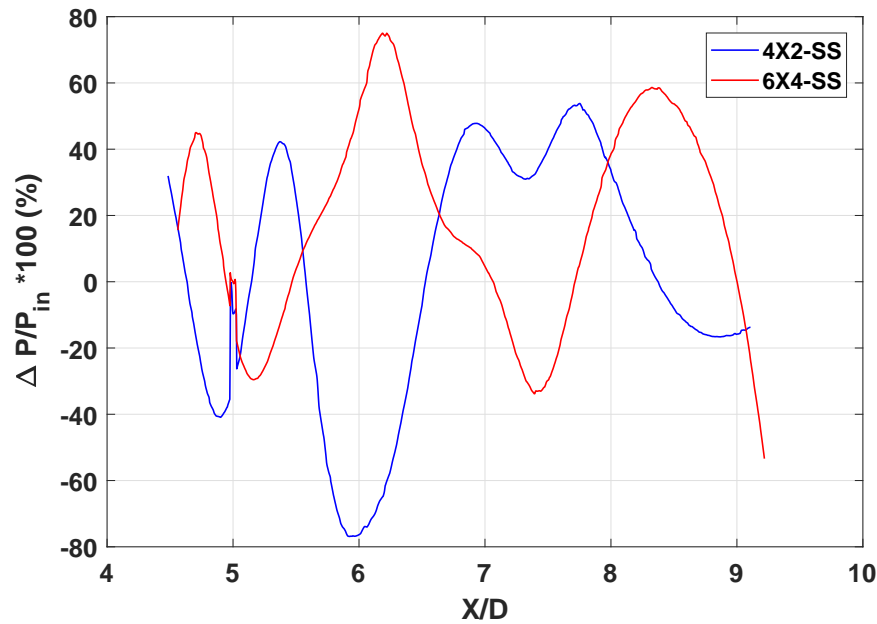


Figure 5.23: Pressure difference between inside of trailer and outside along the length of the side-skirt

5.6. Instantaneous and Time averaged solution

The conclusions drawn in the previous sections were based on instantaneous results. Limited samples obtained during the simulations were used to come up with those conclusions. It must be noted here that the behaviour observed in the above instantaneous plots was observed in other time samples too. In order to ensure that the behaviour observed above is time independent, time averaging is done for 4X2 case. In this case a single-axle-no-side-skirt case was simulated for one full cycle (4s). For the mean solution 25 samples were used in this cycle corresponding to sampling frequency of 6.25Hz. A sample was taken every 0.16s. From figure 5.24 it can be deduced that the instantaneous and time averaged mostly match with certain differences. The small scale ripples disappear while overall pressure layout remains mostly the same. Especially the inflow hypothesis still holds good. In figure 5.24a, the *time averaged* plots indicate that the entry point inflow streamlines is right in front the high pressure region. More instantaneous plots are provided in D figure D.4. Furthermore, it can be concluded that there is close correlation between the shedding frequency of these ripples (from first rear wheel) and the mass entering the underbody beneath the side-skirt. Lastly, the MFR validation is done with respect to the values found earlier in table 5.3 where only 4 time samples were considered. In table 5.5, the comparison between MFR (5 samples) and MFR (full cycle) is presented and are in good agreement.

Table 5.5: Mass flow rate (kg/s)

Position	FW	FUEL TANK	RW1	GAP	RW2	RW_SS_GAP	SS
4X2	-2,77	-2,26	-1,31	-0,32	-1,29	0,20	4,50
4X2_mean_1cycle	-2,84	-2,72	-1,12	-0,31	-1,28	0,11	3,95

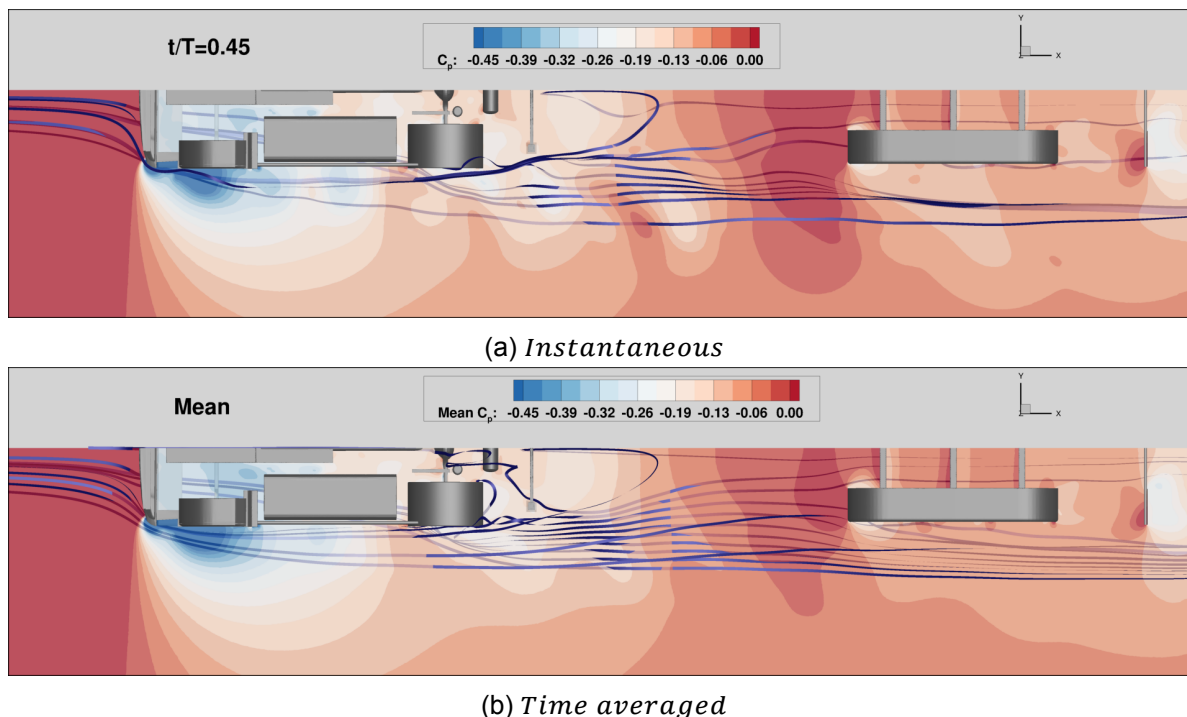


Figure 5.24: Instantaneous and Time averaged

5.7. Summary of all dynamics

- In the single axle case, side-skirt is able to restrict majority (88%) of mass flowing into the underbody. The bleed flow beneath fuel tank conveniently leaves the underbody without much restriction and separation. Eventually, majority of bleed flow joins the free stream without having to curl around the rear wheels and end up in the underbody.
- The addition of one more axle results in higher suction in the wake of last rear wheel, the extent and size in space of this low pressure region is quite large compared to single axle case. This region extends from wake of the wheel to the sides along the width of the truck. This potentially acts like a larger vacuum cleaner right behind the wheel which increases the bleed rate from all components especially the one beneath fuel tank.
- The additional axle also creates a larger separated region when they leave tractor underbody around the first rear wheel. The underbody bleed now escapes around it. A larger separated region induces a low pressure region in and around the rear wheel-wells drawing more flow closer to the trailer underbody and towards the ground. The half of wheel-well are below the side-skirt coverage area, the additional suction makes it easier for the flow to escape below the side-skirt into the underbody.
- The correlation between the high pressure ripple and the entry point of the flow entering the underbody is quite interesting. The high pressure ripples are emanating from the free shear layers separated from the first rear wheel in both single and dual axle cases. It was also observed that the mass flowing into the underbody beneath the side-skirt is highly influenced by the position of high pressure ripple with respect to side-skirt. In other words, the closer the ripple to the side-skirt, the more mass flow into the underbody.

5.8. Modifications

The motivation for modifications are discussed in this section. Within the given time frame of this thesis only two modifications were tried and tested and that too only steady state simulations were conducted. Based on previous sections it can be concluded that the low pressure region behind the rear wheels in 6X4 condition is cause for higher bleed rates in underbody flow and eventually more mass flow into trailer underbody. Furthermore, closing off the wheelwells or wheel houses cuts-off the low momentum ejection which was pulling the streamlines down towards the wall. Thus it is beneficial to avoid this low pressure region and excessive bleed and ejection. One way to achieve this would be to reduce the extent or completely eliminate the low pressure region. Since it is the wake of wheels, it is not possible to completely eliminate low pressure region. Reducing the extent can be achieved by blocking any source that aggravates the existing low pressure region. This means avoid any acceleration of flow in and around the wheels. This is achieved by simply blocking bleed flow. Two important regions of bleed flow are the one beneath the fuel tank and the wheelhouses themselves. The final modifications are extended sidepod (figure 5.25b) and wheelhouse cover (figure 5.25c). Both these modifications include gap cover which covers the gap between the two rear wheels.

5.8.1. Evaluation of modifications

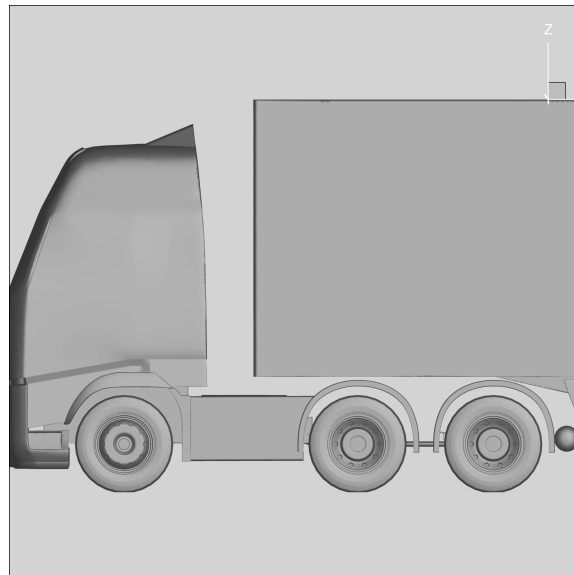
The drag coefficients of MODs and 6X4-SS are compared in this section. Firstly, the steady and unsteady state results of 6X4-SS must be compared. Figure 5.26 shows that the steady state simulation under-predicts the drag coefficient. Furthermore, the drag coefficients of MODs are compared with steady state result of 6X4-SS. Both the modifications exhibit higher drag. In order to further understand the increase in drag, MFR analysis is again conducted on 6X4-SS steady and MOD cases (table 5.6). Table 5.6 clearly sets apart unsteady simulations from steady simulations and highlights the unreliable results obtained from steady state simulations. Firstly, in 6X4 – SS case, there is no underbody flow. This is a big deviation from the hypothesis that was suggested in earlier sections. The MOD MFR's are also quite inconsistent, in that the MOD2 shows significant underbody flow while MOD1 shows no UB flow. These anomalies led to the conclusion that steady state results are highly unreliable and must not be considered for any evaluation of problems.

Table 5.6: Mass Flow Rates (*kg/s*)

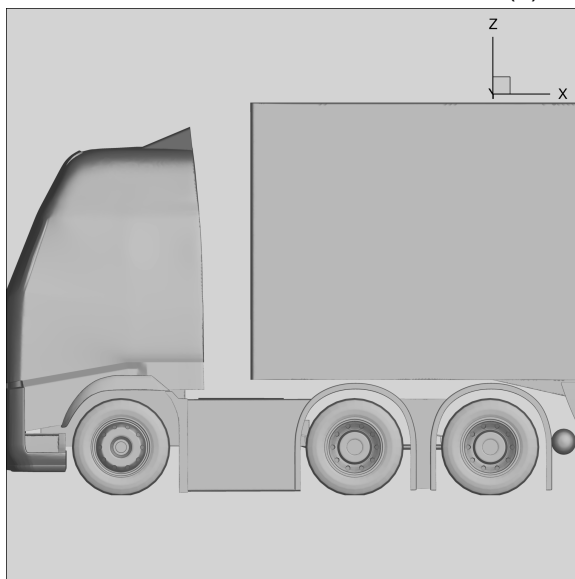
Position	FW	FUEL TANK	RW1	GAP	RW2	RW_SS_GAP	SS
6X4_SS	-2,65	-3,31	-2,72	-0,4124	-1,149	0,1919	4,51
6X4_SS_Steady	-2,73	-1,931	-2,12	0,0085	0,596	-0,172	-0,01
MOD1	-0,03	-1,22	-4,56	-1,79	-0,88	-0,07	-0,3
MOD2	-4,56	-1,79	-0,88	-0,07	-0,3	0,073	5,48

5.8.2. More insights into MODs

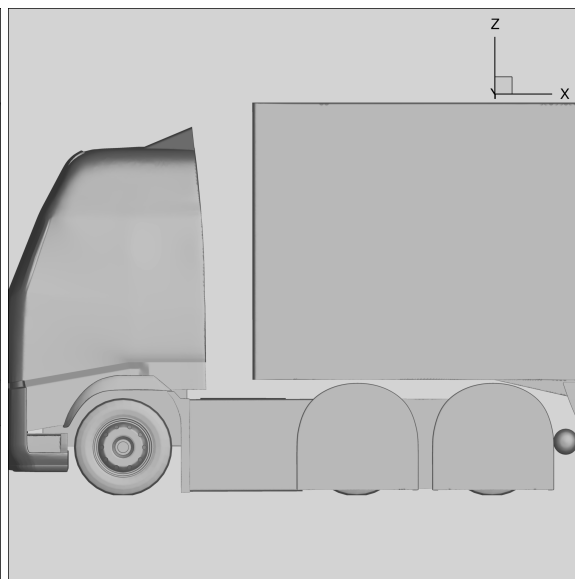
Although the steady state simulations on MODs were not fruitful, some insights were developed by looking at the results and contemplating on the ideas of MODs. The idea to cut-off the bleed seems straight forward but it has its own consequences. Since, bleed cut-off implies that the flow now has to take the path where there is more blockage, it is highly possible that the drag may increase. The bleed cut-off must be carefully done in order to obtain drag reduction or in this case restore side-skirt efficiency. The balance between increase in drag due to forcing the flow to take the path of more blockage and drag reduction obtained in avoiding



(a) 6X4 – SS



(b) MOD1



(c) MOD2

Figure 5.25: Modifications

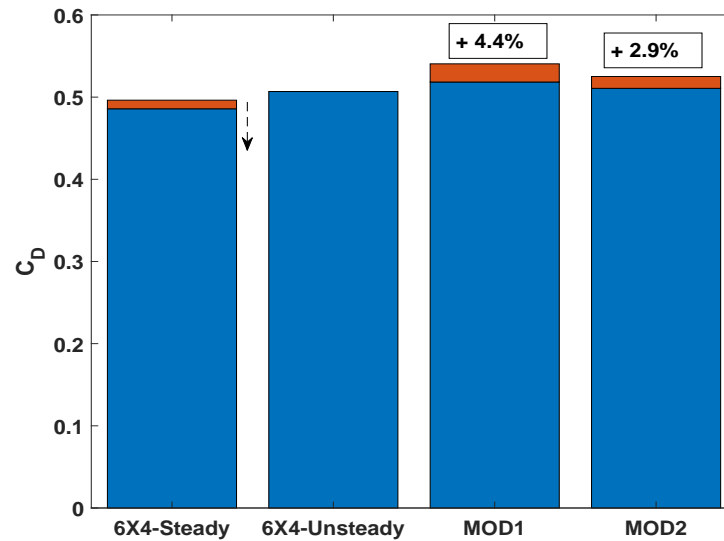


Figure 5.26: C_D comparison of MODS

more mass flowing into the underbody is very crucial. Furthermore, a better solution would be to use vanes to divert the flow as needed, but since we are dealing with underbody having delicate structures like vanes is not recommended from a structural point of view.

5.9. Geometry Simplification

The truck model used in this thesis is quite amplified yet very detailed in some areas. It has accurately modelled wheels with grooves and wheel-wells. During post-processing it was observed that the grooves in the wheels did not actively influence the performance in that no significant flow features originated from them. On the other hand wheel-wells of rear wheels proved to be quite influencing in that they give rise to a low pressure region as explained earlier. So, it can suggested from this thesis that wheel grooves can be dropped in future simulations while wheel-wells must be reasonably modelled in terms their depth.

It is also important to discuss here about the addition of more underbody components like suspension, battery box etc. Adding more components means more blockage, so this means they might aggravate the bleed rate and worsen the situation. More bleed implies more underbody flow.

6

Conclusions and Recommendations

The research objectives (sec 2.2) formulated are concluded in this chapter along with some recommendations for future work.

1. *What is the influence of six vortices coming off the front wheelhouse and underbody flow on side-skirt's performance?*

Among the six vortices identified in literature (figure 2.2b), the three vortices L,E,R emanating from the wheel-patch are swept away from the bleed flow escaping from the underbody. These three have no influence on the side-skirt performance. In fact, they are washed away from bleed flow and do not enter the trailer underbody. Furthermore, in the upper portion of the front wheel, the other vortices, A,B,S and C as identified in literature, coalesce and form one big separated region which is identified as FB in this thesis (figure 5.2a). Although signs of existence of vortex B alone was found. Nevertheless, the combined separated region has profound influence on the side-skirt performance than individual vortices. The combined separated region is the one which enters the trailer underbody and is responsible for inflow and hence the momentum exchange and eventually increased drag.

2. *How are the six principle vortices affected by rear wheelhouse flow?*

The combined separated region moves downstream but unlike other surrounding separated regions, this region does not expand towards the free stream. Instead they are drawn more towards the truck due to the low pressure region present on the sides of the truck. The rear wheel and wheelhouse has low pressure region behind them, in its wake. Additionally the wheel-well itself acts as a cavity for the oncoming flow and there exists a low pressure region inside it too. Both these low pressure regions draw more flow into the trailer underbody. Furthermore, the concept of bleed is also influenced by these low pressure regions. Firstly, the underbody shaft components offer a resistance to the flow beneath the truck. It escapes from the sides, which offers least resistance due to the low pressure regions mentioned earlier. Thus, bleed flow is a consequence of higher blockage in the underbody and low pressure regions.

3. *What are the flow features originating from the rear wheelhouse and what is their influence on side-skirt's performance?*

The ejection hypothesis can be attributed to wheelhouse flow. The cavity or the wheel-well entraps fluid in it and ejects it out because of rotation of the wheel. This is analogical to washing machine where there is no lid and all the fluid is ejected out. The low momentum fluid ejected from the wheel-well adds to the momentum losses and eventually contributed to the drag. The important flow feature affecting the side-skirt performance is the flow escaping into the trailer underbody beneath the side-skirt. This is due to the low pressure region existing behind the rear wheels, in their wake. Mixing of low and high momentum fluid in this manner is detrimental to side-skirt's performance as the function of side-skirt is to prevent this mixing by acting like an air dam.

4. *What is/are major flow feature differences between single (4X2) and dual(6X4) axle condition? Which of them really affect the performance of side-skirt? How do these flow features change in the presence of side-skirt in the respective configurations (single and dual rear axle configurations)?*

The major difference seen between the single and dual axle cases is the low pressure region behind the last rear wheel. In dual axle case (6X4), the low pressure region is bigger than compared to single axle case. The additional axle imposes more blockage to underbody flow which eventually separates at the leading edge of the first rear wheel. This is analogical to adding a bluff body like cylinder in front of pre-existing cylinder in yawed flow. The additional cylinder/axle gives rise to a bigger separation region on leeward side. This is one of the causes for the increased bleed rates in dual axle case. Furthermore, the ripples emanating from first rear wheel, also aid the flow in entering the trailer underbody. Their correlation is established in instantaneous results.

6.1. Recommendations

CFD Approach- One of the strongest recommendations from Scheeve [17] was not to use URANS as the unsteadiness is indeterministic. The results of this thesis done using URANS approach have given excellent results both in terms of validation with Scheeve [17]'s results and grid convergence. Scheeve [17] used steady state simulations to evaluate wheel-house modification whereas in this thesis steady state results predicted different trends compared to Unsteady RANS. Thus, the author of this thesis recommends URANS for this kind cases where there are large regions of separation. Unsteady simulations give better understanding of flow field than steady state. Furthermore, it is recommended to use DES or LES approach for these cases to gain better insights into spectral nature of the flow. These insights might help us in choosing the right modification in future to rectify this problem.

Domain Sizing- The SAE J2966 standard[16] recommendation of downstream length ($8L$) for the fluid domain resulted in reverse flow during initial simulations. It is recommended to use a longer fluid domain of about ($15 - 17L$) while keeping the length of the wake refinement box the same. This would not impact the number of cells too much because the region of extended length is already quite coarse.

Truck CAD Model- The geometry simplification as described in section (sec 5.9) must be implemented in future simulations as they can reduce the number of cells required to a certain extent. This might be helpful for DES/LES simulations as they have higher spatial and temporal requirements.

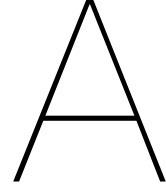
Extension to single axle case- The ripple hypothesis is also seen in single axle case.

This means if the separation of the bleed flow is controlled at the rear wheel in single axle case, there is scope for improving the efficiency of side-skirt in this case too.

Boundary layer height- The commonly used flat plate theory to estimate boundary layer height on top of the trailer-end is flawed. As seen in this thesis the boundary layer height is at least 5 times larger than what is predicted by flat plate theory.

Ripple Correlation The correlation between the the high pressure ripples emanating from first rear wheel and the variation of mass flow entering the trailer underbody will be crucial to future simulations. This gives confirms contribution of ripples to increase mass flow into the underbody. It can also be deciding factor whether to block the bleed beneath the fuel-tank or block wheelhouses.

Yawed Simulations All the simulations in this thesis were conducted in no-yaw condition but for truck's aerodynamic performance, yawed simulations are crucial. In fact the side-skirt is highly susceptible to wind direction as seen from WABCO's track test data.



Appendix A

Some of the terms κ - ω transport equations are elaborated in this section.

Effective Diffusivity

$$\Gamma_{\kappa/\omega} = \mu + \mu_t \quad (\text{A.1})$$

The eddy viscosity is modelled based on the following equation,

$$\mu_t = \frac{\rho\kappa}{\omega} \frac{1}{\max\left[\frac{1}{\alpha^*}, \frac{SF_2}{a_1\omega}\right]} \quad (\text{A.2})$$

where,

$$F_2 = \tanh(\phi_2^2) \quad (\text{A.3})$$

$$\phi_2 = \max\left[\frac{2\sqrt{\kappa}}{0.09\omega y}, \frac{500\mu}{\rho y^2 \omega}\right] \quad (\text{A.4})$$

$$\text{y-distance from the wall} \quad (\text{A.5})$$

Production Terms

$$G_\kappa = \mu_t S^2 \quad (\text{A.6})$$

$$\text{where } S = \sqrt{2S_{ij}S_{ij}}, \quad (\text{A.7})$$

$$G_\omega = \frac{\alpha\alpha^*}{\nu_t} G_\kappa \quad (\text{A.8})$$

$$\alpha = 1 \text{ High for Reynolds number flows} \quad (\text{A.9})$$

and blending function is used to vary α_∞ to comply with viscous sublayer and logarithmic law formulation. α_∞ is a constant in Standard $\kappa - \omega$ model

$$\alpha_\infty = F_1\alpha_{\infty,1} + (1 - F_1)\alpha_{\infty,2} \quad (\text{A.10})$$

$$\alpha_{\infty,1} = \frac{\beta_{i,1}}{\beta_{\infty}^*} - \frac{\kappa^2}{\sigma_{\omega,1}\sqrt{\beta_{\infty}^*}} \quad (\text{A.11})$$

$$\alpha_{\infty,2} = \frac{\beta_{i,2}}{\beta_{\infty}^*} - \frac{\kappa^2}{\sigma_{\omega,2}\sqrt{\beta_{\infty}^*}} \quad (\text{A.12})$$

Dissipation Terms

$$Y_{\kappa} = \rho\beta^*\kappa\omega \quad (\text{A.13})$$

$$\beta_i^* = \beta_{\infty}^* \left(\frac{\frac{4}{15+(Re_t/R_{\beta})^4}}{1+(Re_t/R_{\beta})^4} \right) \quad (\text{A.14})$$

with $R_{\beta} = 8$ and $\beta_{\infty}^* = 0.09$.

$$Y_{\omega} = \rho\beta\omega^2 \quad (\text{A.15})$$

Instead of having a constant β like in Standard $\kappa - \omega$ model, again a blending function is used,

$$\beta_i = F_1\beta_{i,1} + (1 - F_1)\beta_{i,2} \quad (\text{A.16})$$

$$F_1 = \tanh(\phi^4) \quad (\text{A.17})$$

$$\phi_1 = \min \left[\max \left(\frac{\sqrt{\kappa}}{0.09\omega y}, \frac{500\mu}{\rho y^2 \omega} \right), \frac{4\rho\kappa}{\sigma_{\omega,2}D_{\omega}^+ y^2} \right] \quad (\text{A.18})$$

where D_{ω}^+ is related to positive portion of cross-diffusion term.

$$D_{\omega}^+ = \max \left[\frac{2\rho}{\sigma_{\omega,2}\omega} \frac{\partial \kappa}{\partial x_j} \frac{\partial \omega}{\partial x_j}, 10^{-10} \right] \quad (\text{A.19})$$

Model Constants

Some of the model constants exclusive to $\kappa - \omega SST$ model are mentioned here, the values of all constants can be referred from [2]

Table A.1: Model Constants

Constant	Value
$\sigma_{\kappa,1}$	1.176
$\sigma_{\omega,1}$	2.0
$\sigma_{\kappa,2}$	1.0
$\sigma_{\omega,2}$	1.168
a_1	0.31
$\beta_{i,1}$	0.075
$\beta_{i,2}$	0.0828

B

Appendix B

B.1. Linearized Equation Coefficients

This appendix explains about the linearization of momentum equation. The idea and equations presented in this section are from Darwish et al. [4]. Some of the notations of Darwish et al. [4] are altered here in order to be consistent with ANSYS [2] notations.

The coefficients of 3.13 for an upwind scheme are as follows,

$$a_p = \sum_{nb} \left(\Gamma_f \frac{\vec{A}_f \cdot \vec{A}_f}{\vec{A}_f \cdot \vec{d}} + \|\dot{m}_f, 0\| \right) \quad (\text{B.1})$$

$$a_{nb} = - \left(\Gamma_f \frac{\vec{A}_f \cdot \vec{A}_f}{\vec{A}_f \cdot \vec{d}} + \|\dot{m}_f, 0\| \right) \quad (\text{B.2})$$

where \vec{d} is the vector joining adjacent cell centers.

B.2. Coupled Solver Algorithm

The linearized momentum equation in x-direction 3.19 is expanded as follows,

$$a_p^{uu} u_p + a_p^{uv} v_p + a_p^{uw} w_p + a_p^{up} P_p - \sum_{nb} a_{nb}^{uu} u_{nb} - \sum_{nb} a_{nb}^{uv} v_{nb} - \sum_{nb} a_{nb}^{uw} w_{nb} + \sum_{nb} a_{nb}^{up} P_{nb} = b^u \quad (\text{B.3})$$

And in the other two directions,

$$a_p^{vu} u_p + a_p^{vv} v_p + a_p^{vw} w_p + a_p^{vp} P_p - \sum_{nb} a_{nb}^{vu} u_{nb} - \sum_{nb} a_{nb}^{vv} v_{nb} - \sum_{nb} a_{nb}^{vw} w_{nb} + \sum_{nb} a_{nb}^{vp} P_{nb} = b^v \quad (\text{B.4})$$

$$a_p^{wu} u_p + a_p^{wv} v_p + a_p^{ww} w_p + a_p^{wp} P_p - \sum_{nb} a_{nb}^{wu} u_{nb} - \sum_{nb} a_{nb}^{wv} v_{nb} - \sum_{nb} a_{nb}^{ww} w_{nb} + \sum_{nb} a_{nb}^{wp} P_{nb} = b^w \quad (\text{B.5})$$

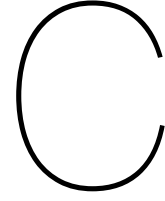
Final form of continuity or pressure equation after Rhie-Chow interpolation is,

$$a_p^{pp} p_p + a_p^{pu} u_p + a_p^{pv} v_p + a_p^{pw} w_p + \sum_{nb} a_{nb}^{pp} p_{nb} + \sum_{nb} a_{nb}^{pu} u_{nb} + \sum_{nb} a_{nb}^{pv} v_{nb} + \sum_{nb} a_{nb}^{pw} w_{nb} = b_p^p \quad (\text{B.6})$$

The above equations can be arranged in matrix form as follows. It must be noticed that the following equations are for a given cell.

$$\begin{bmatrix} a_p^{uu} & a_p^{uv} & a_p^{uw} & a_p^{up} \\ a_p^{vu} & a_p^{vv} & a_p^{vw} & a_p^{vp} \\ a_p^{wu} & a_p^{wv} & a_p^{ww} & a_p^{wp} \\ a_p^{pu} & a_p^{pv} & a_p^{pw} & a_p^{pp} \end{bmatrix} \begin{bmatrix} u_p \\ v_p \\ w_p \\ p_p \end{bmatrix} + \sum_{nb} \begin{bmatrix} a_{nb}^{uu} & a_{nb}^{uv} & a_{nb}^{uw} & a_{nb}^{up} \\ a_{nb}^{vu} & a_{nb}^{vv} & a_{nb}^{vw} & a_{nb}^{vp} \\ a_{nb}^{wu} & a_{nb}^{wv} & a_{nb}^{ww} & a_{nb}^{wp} \\ a_{nb}^{pu} & a_{nb}^{pv} & a_{nb}^{pw} & a_{nb}^{pp} \end{bmatrix} \begin{bmatrix} u_{nb} \\ v_{nb} \\ w_{nb} \\ p_{nb} \end{bmatrix} = \begin{bmatrix} b_p^u \\ b_p^v \\ b_p^w \\ b_p^p \end{bmatrix} \quad (\text{B.7})$$

The above system of equations can be written for each cell in the domain and a global matrix system of equation is formed. This equation is solved every iteration. Since each variable in the global equations are treated implicitly, this is the main reason behind rapid convergence [4].



Appendix C

Table C.1: GCI study based on [3]

Grid Convergence Index Calculations (based on Celik, B. I., et.al., 2008)				
	Finer Mesh	Fine Mesh	Medium	Course Mesh
Vehicle size (HxWxL) [m3]	84,15	84,15	84,15	84,15
Number of cells (N)	49000000	45000000	38000000	22000000
Representative mesh height (h) [m]	0,012	0,012	0,013	0,016
Drag Coefficient	0,5329	0,5287	0,5319	0,5186
Mesh Refinement Ratio (r)	1.33	1,03	1,20	1,27
epsilon	Convergence OK	-0,0042	-0,0133	-0,0101
Order of Convergence, P	4			
Error for P	56,19227			
Initial Guess for P	30,91147			
Extrapolated Drag Force (F) [N]	0,57			
Approximate Relative Error	0,79%	0,61%	2,50%	N/A
Extrapolated Relative Error	6,15%	6,89%	6,33%	8,67%
Grid Convergence Index (GCI)	16,87%	1,72%	5,11%	N/A

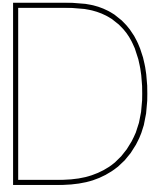
$$e_a^{ij} = \frac{c_D^j - c_D^i}{c_D^j} \quad (\text{C.1})$$

$$r_{ij} = \frac{h_i}{h_j} \quad (\text{C.2})$$

$$h_i = \frac{\text{Vehicle Volume}}{\text{Number of cells in grid } i} \quad (\text{C.3})$$

Table C.2: Surface Mesh Size Control

Control name	min (mm)	max (mm)	Normal Angle (deg)	components
curv-truck	2	50	18	all components of truck except wheels and shaft
curv-shaft	1	15	15	shaft components
curv-wheels	0.75	30	18	wheels of tractor only
curv-misc	1	20	18	miscellaneous componenets
curv-front	1	15	15	front grill and mudguard
curv-SW	0.5	50	16	trailer Side-skirt



Appendix D

D.1. Drag-Fuel formula derivation

We know that the fuel energy input into to a engine is spent on overcoming drag, the rolling resistance and auxillary power. Writing these in a equation form,

$$P = \eta_{engine} \left(\frac{1}{2} \rho V^3 S C_D + C_{RR} W V + auxillarypower \right) \quad (D.1)$$

In our case, the only change between principal configuration is the drag force, thus, studying the fractional change of the above equation gives us,

$$\frac{\Delta P}{P} = \eta_{engine} \frac{\Delta C_D}{C_D} \quad (D.2)$$

Since the power consumed is directly proportional to fuel consumed

$$\frac{\Delta FC}{FC} = \eta_{engine} \frac{\Delta C_D}{C_D} \quad (D.3)$$

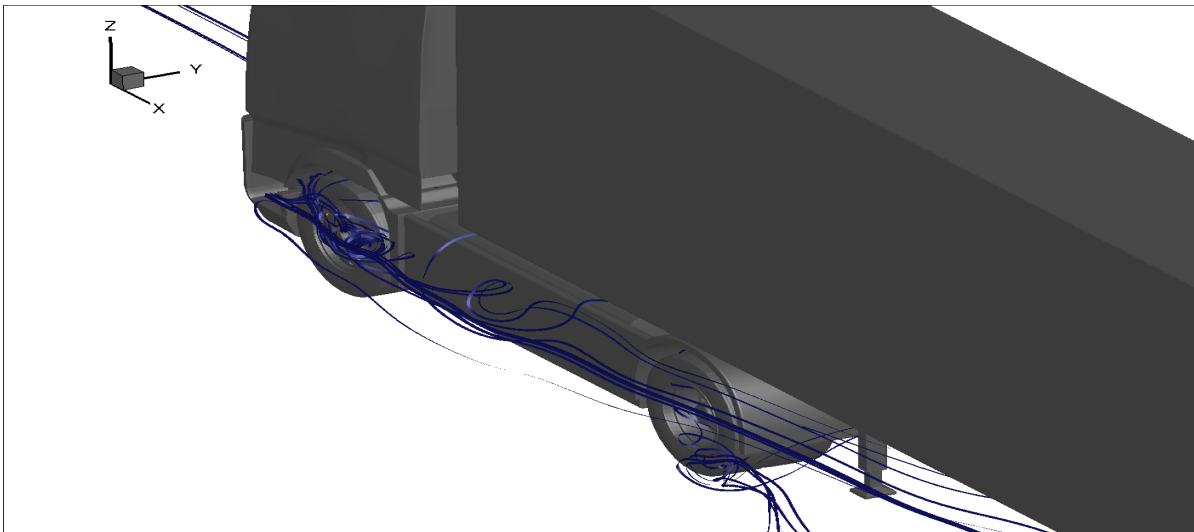


Figure D.1: flow entering trailer underbody

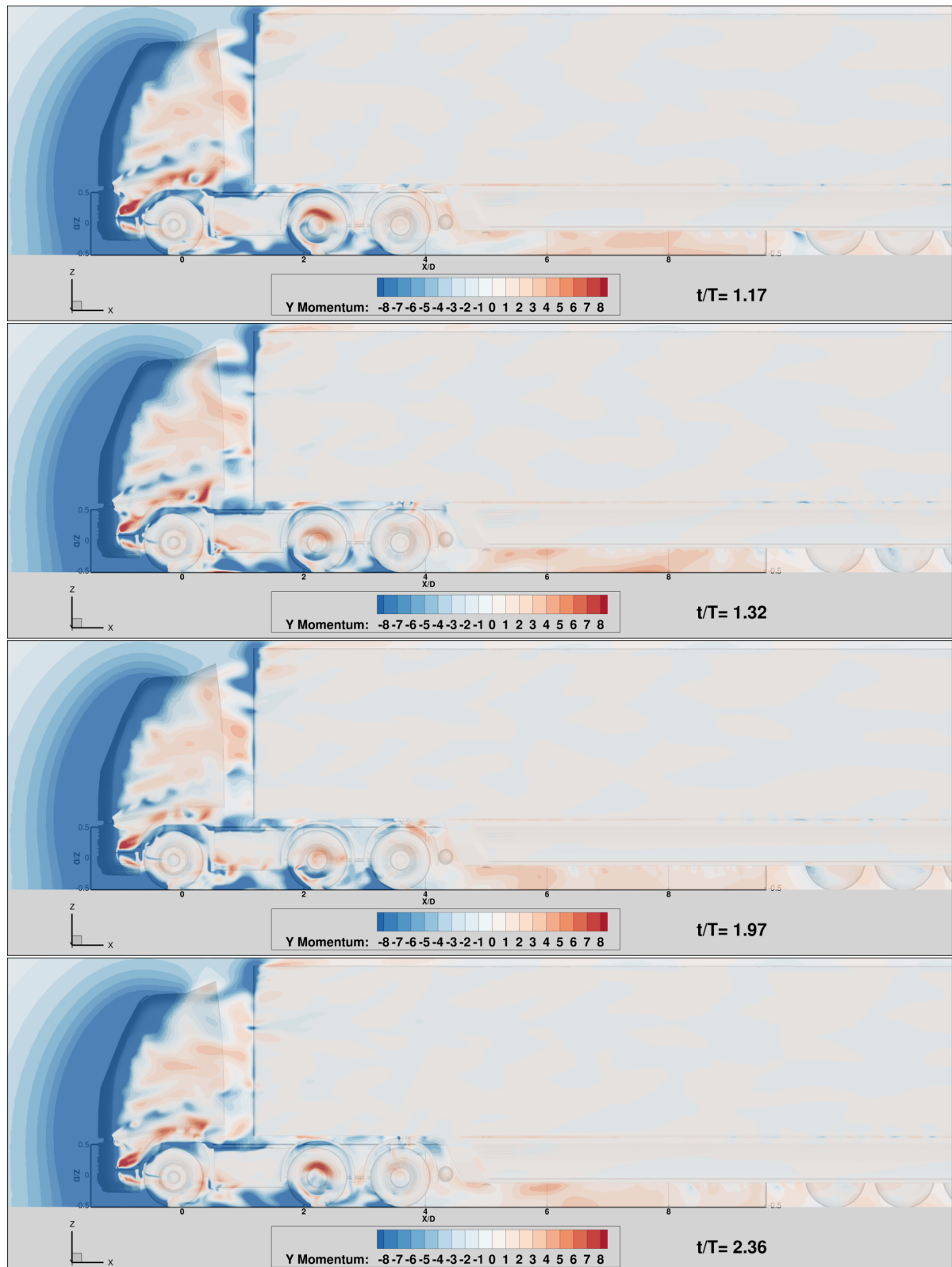


Figure D.2: 6X4 – SS Instantaneous Y-momentum, **outflow** (*blue*), **inflow** (*red*), slice $Y/D = -0.01$

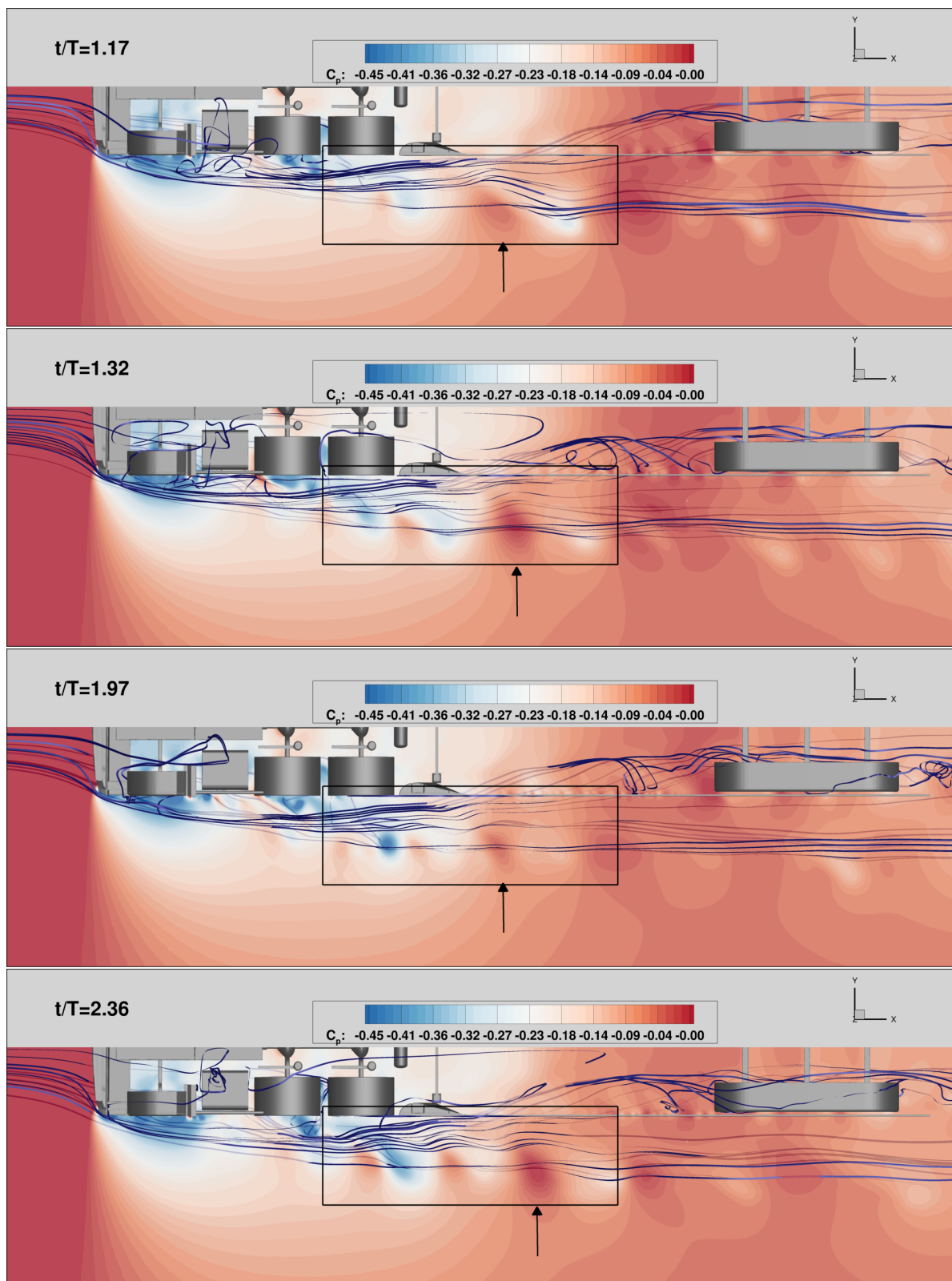


Figure D.3: Inflow and high pressure ripple correspondence

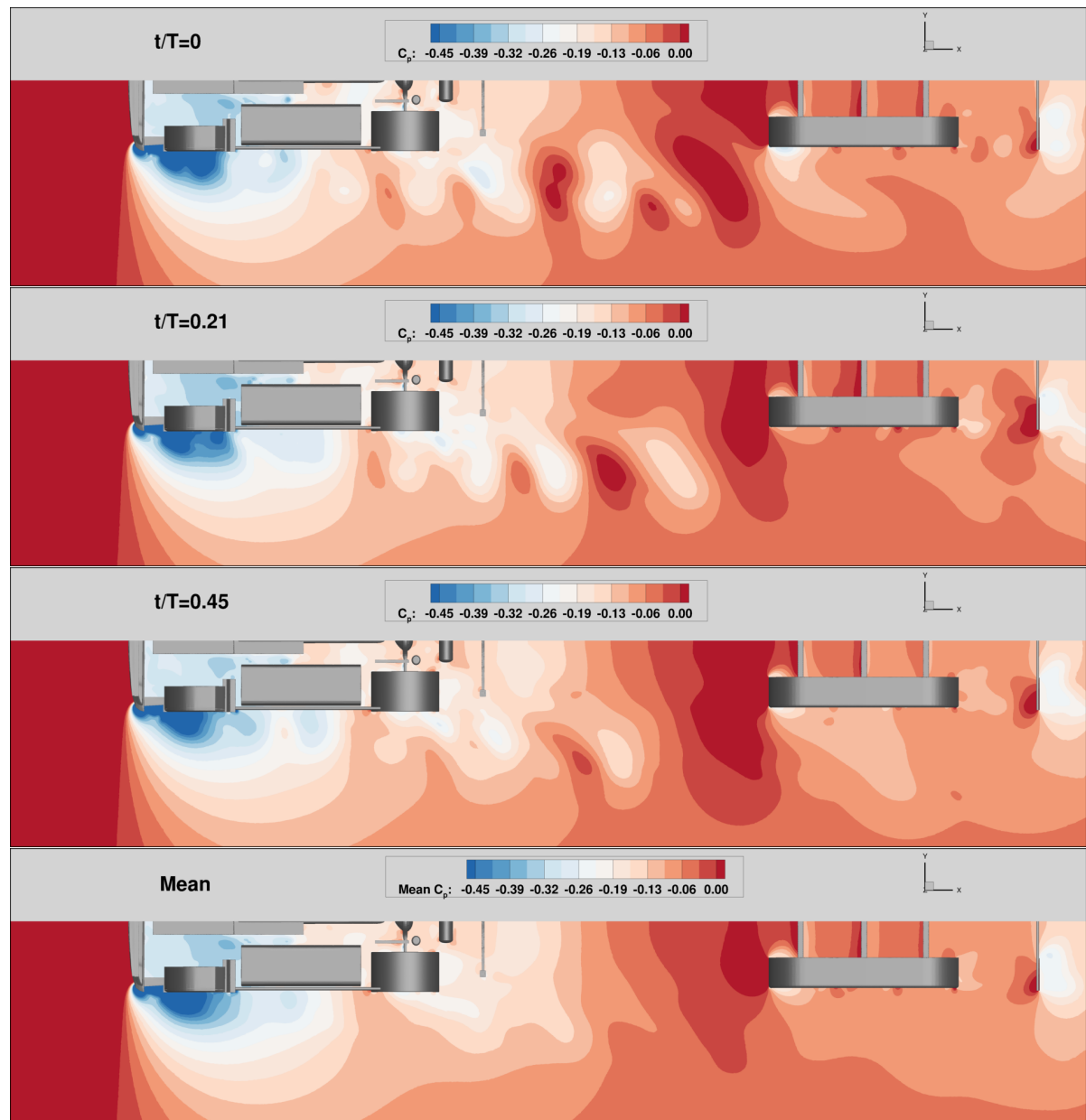
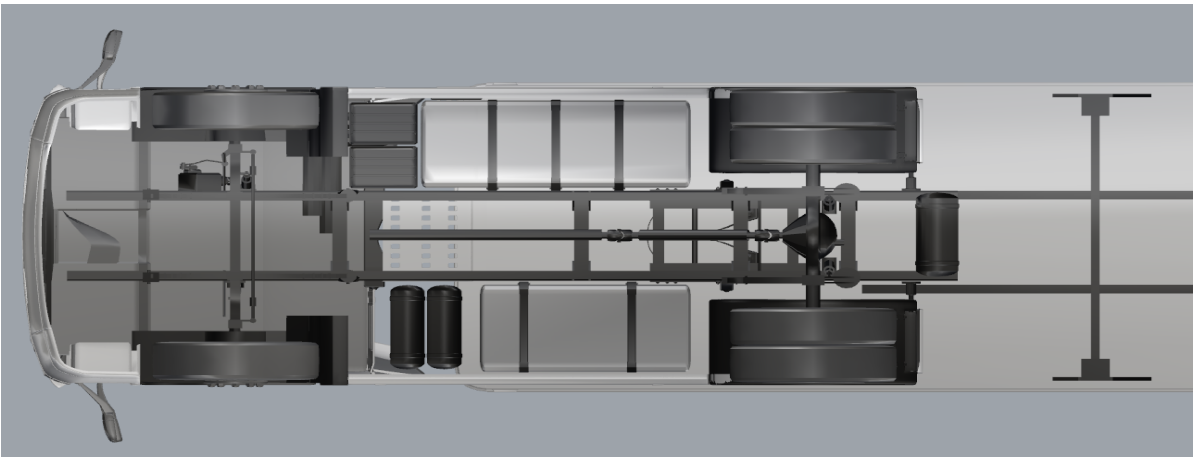


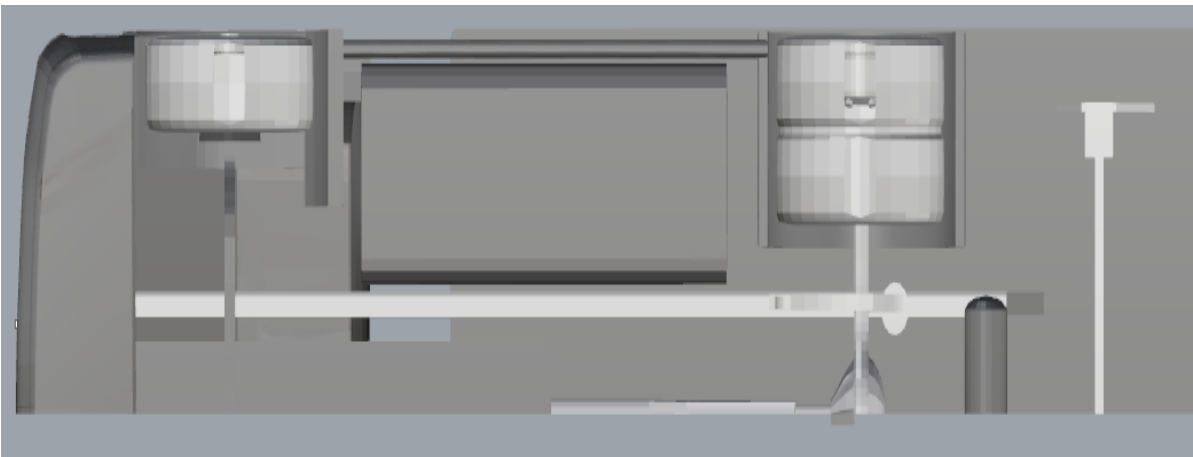
Figure D.4: Instantaneous and Time average plots

E

Appendix E



(a) Volvo FH-13 Underbody



(b) Simplified Volvo FH-13 Underbody (half model)

Figure E.1: Underbody

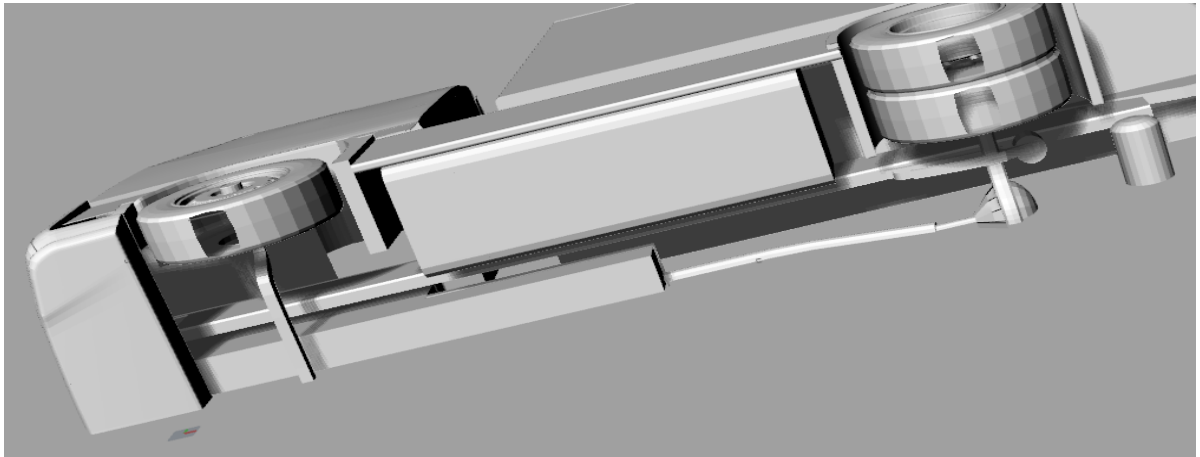


Figure E.2: Underbody with engine block, shaft components, axle, wheels cut-off to emulated wheel patch

Bibliography

- [1] Little change in future emissions without action. URL https://ec.europa.eu/clima/policies/transport/vehicles/heavy_en#tab-0-0.
- [2] ANSYS. ANSYS Fluent Manual.
- [3] Ismail B. Celik, Urmila Ghia, Patrick J. Roache, Christopher J. Freitas, Hugh Coleman, and Peter E. Raad. Procedure for Estimation and Reporting of Uncertainty Due to Discretization in CFD Applications. *Journal of Fluids Engineering*, 130(7):078001–078001–4, jul 2008. ISSN 0098-2202. doi: 10.1115/1.2960953. URL <http://dx.doi.org/10.1115/1.2960953>.
- [4] M Darwish, I Sraj, and F Moukalled. Numerical Heat Transfer, Part B: Fundamentals A Coupled Incompressible Flow Solver on Structured Grids A COUPLED INCOMPRESSIBLE FLOW SOLVER ON STRUCTURED GRIDS. 2007. doi: 10.1080/10407790701372785. URL <http://www.tandfonline.com/action/journalInformation?journalCode=unhb20http://dx.doi.org/10.1080/10407790701372785>.
- [5] Oscar Delgado and Nic Lutsey. Advanced tractor-trailer efficiency technology potential in the 2020–2030 timeframe, 2015. URL <https://www.theicct.org/publications/advanced-tractor-trailer-efficiency-technology-potential-2020-2030-timeframe>.
- [6] Per Elofsson, Guillaume Mercier, Bradley D. Duncan, and Samuel Boissinot. Accurate drag prediction using transient aerodynamics simulations for a heavy truck in yaw flow. In *Lecture Notes in Applied and Computational Mechanics*, volume 79, pages 343–360. Springer, Cham, 2016. ISBN 9783319201214. doi: 10.1007/978-3-319-20122-1_22. URL http://link.springer.com/10.1007/978-3-319-20122-1_22.
- [7] Teddy Hobeika. Investigation of Tyre Geometry Influence Improving landfill monitoring programs on Road Vehicle Aerodynamics with the aid in of - imaging techniques and geographical information systems. 2012.
- [8] S Krajnović, S Sarmast, and B Basara. Numerical Investigation of the Flow Around a Simplified Wheel in a Wheelhouse. *Journal of Fluids Engineering*, 133(11):111001–111001–12, oct 2011. ISSN 0098-2202. doi: 10.1115/1.4004992. URL <http://dx.doi.org/10.1115/1.4004992>.
- [9] Rick Mihelic, Dave Scheller, and Mike Roeth. Confidence Report on Trailer Aerodynamic Device Solutions, 2015. URL https://nacfe.org/wp-content/uploads/2018/02/TE_Trailer_Aero_CR_FINALFINAL.pdf.
- [10] Joshua D Miller and Cristiano Façanha. The State of Clean Transport Policy-A 2014 synthesis of Vehicle and fuel policy developments, 2014. URL https://www.theicct.org/sites/default/files/publications/ICCT_StateOfCleanTransportPolicy_2014.pdf.

- [11] Stephen Nichols, Kidambi Sreenivas, Steve Karman, and Brent Mitchell. Turbulence Modeling for Highly Separated Flows. In *45th AIAA Aerospace Sciences Meeting and Exhibit*, Aerospace Sciences Meetings. American Institute of Aeronautics and Astronautics, jan 2007. doi: 10.2514/6.2007-1407. URL <http://dx.doi.org/10.2514/6.2007-1407>.
- [12] John Norris, Giulia Escher, and Ricardo Energy. Heavy Duty Vehicles Technology Potential and Cost Study, 2017. URL https://www.theicct.org/sites/default/files/publications/HDV-Technology-Potential-and-Cost-Study_Ricardo_Consultant-Report_26052017_vF.pdf.
- [13] Milovan Peric. Flow Simulation Using Control Volumes of Arbitrary Polyhedral Shape. *ERCOFTAC Bulletin No 62*, 2004. URL <http://www.ercoftac.org/publications/ercoftac{ }bulletin/bulletin{ }62/>.
- [14] Milovan Peric and Stephen Ferguson. The advantage of polyhedral meshes. URL <https://pdfs.semanticscholar.org/51ae/90047ab44f53849196878bfec4232b291d1c.pdf>.
- [15] Tamas Regert and Tamas Lajos. Description of flow field in the wheelhouses of cars. *International Journal of Heat and Fluid Flow*, 28(4):616–629, 2007. ISSN 0142-727X. doi: 10.1016/j.ijheatfluidflow.2007.04.017. URL <http://www.sciencedirect.com/science/article/pii/S0142727X07000641>.
- [16] SAE International. Guidelines for Aerodynamic Assessment of Medium and Heavy Commercial Ground Vehicles Using Computational Fluid Dynamics, 2014. URL https://www.sae.org/standards/content/j2966_201309/.
- [17] TS Scheeve. *Truck wheelhouse aerodynamics Numerical investigations into the phenomenon in heavy truck wheelhouses*. Master's thesis, T U Delft, 2013. URL https://dlrka77tlqy5f1.cloudfront.net/LR/Organisatie/Afdelingen/Aerodynamics__Wind_Energy__Flight_Performance_and_Propulsion/Aerodynamics/MSc_Theses/2013/Scheeve__T.S..pdf.
- [18] David Söderblom, Per Elofsson, Linus Hjelm, and Lennart Lofdahl. Experimental and Numerical Investigation of Wheel Housing Aerodynamics on Heavy Trucks. *SAE Int. J. Commer. Veh.*, 5:29–41, 2012. doi: 10.4271/2012-01-0106. URL <http://doi.org/10.4271/2012-01-0106>.
- [19] Kidambi Sreenivas, Ramesh Pankajakshan, Stephen Nichols, Brent Mitchell, Lafayette Taylor, and David Whitfield. Aerodynamic Simulation of Heavy Trucks with Rotating Wheels. In *44th AIAA Aerospace Sciences Meeting and Exhibit*, Aerospace Sciences Meetings. American Institute of Aeronautics and Astronautics, 2006. doi: 10.2514/6.2006-1394. URL <http://dx.doi.org/10.2514/6.2006-1394>.
- [20] R.G. Stephens and H. Babinsky. An Experimental Study on Truck Side-Skirt Flow. *SAE International Journal of Passenger Cars - Mechanical Systems*, 9(2):2016–01–1593, 2016. ISSN 1946-4002. doi: 10.4271/2016-01-1593. URL <http://papers.sae.org/2016-01-1593/>.
- [21] Symscape. Polyhedral, Tetrahedral, and Hexahedral Mesh Comparison, feb 2013. URL <http://www.symscape.com/polyhedral-tetrahedral-hexahedral-mesh-comparison>.

- [22] G. van Raemdonck. *Design of Low Drag Bluff Road Vehicles*. PhD thesis, 2012.
- [23] Alexey Vdovin. Investigation of Aerodynamic Resistance of Rotating Wheels on Passenger Cars. *Master of Science Thesis*, pages 1–6, 2013. ISSN 1946-4002. doi: 10.4271/2014-01-0606.
- [24] Frank White. Fluid Mechanics. *McGraw-Hill, New York*, page 862, 2010. ISSN 1364-0321. doi: 10.1111/j.1549-8719.2009.00016.x.Mechanobiology. URL <http://www.amazon.com/Mechanics-Student-McGraw-Hill-Mechanical-Engineering/dp/0077422414>.
- [25] Frank M. White. *Viscous Fluid Flow*. McGraw-Hill Higher Education, 2006. ISBN 9780072402315.